12-2011

Nanoparticle Necklace Network Arrays Exhibiting Room Temperature Single-Electron Switching

Jennifer L. Kane
University of Nebraska-Lincoln, jkane@huskers.unl.edu

NANOPARTICLE NECKLACE NETWORK ARRAYS EXHIBITING ROOM TEMPERATURE SINGLE-ELECTRON SWITCHING

by

Jennifer Lynn Kane

A DISSERTATION

Presented to the Faculty of

The Graduate College at the University of Nebraska

In Partial Fulfillment of Requirements

For the Degree of Doctor of Philosophy

Major: Engineering

Under the Supervision of Professor Ravi F. Saraf

Lincoln, Nebraska

December, 2011

NANOPARTICLE NECKLACE NETWORK ARRAYS EXHIBITING ROOM TEMPERATURE SINGLE-ELECTRON SWITCHING

Jennifer Lynn Kane, Ph.D.

University of Nebraska, 2011

Adviser: Ravi F. Saraf

A single nanoparticle is one of the most sensitive electronic devices for sensing chemicals in a gas or liquid. The conductivity of a single Au nanoparticle is significantly modulated by the binding of a molecule that alters charge by just one electron. However, the single-electron sensitivity requires cryogenic temperatures and interconnection is not easy. A patterned two-dimensional network of one-dimensional nanoparticle necklaces made up of 10 nm Au particles are fabricated and shown to exhibit similar single-electron effect at room temperature. Furthermore, the long range conductivity of over 10's of microns makes the structure easy to self-assemble onto conventional microelectronics circuitry. A device exhibiting single-electron effect is characterized by highly non-linear current-bias behavior where at bias, $V > V_T$ current rises rapidly and scales as $(V/V_T - 1)^{\zeta}$, where $\zeta \geq 1$ is the critical exponent and V_T is the threshold voltage. Below V_T, current does not flow. Thus, V_T is the switching voltage and larger ζ signifies sharper switching characteristics. While arrays of one and two dimension are well known to exhibit appreciable V_T at cryogenic temperatures, at ambient temperatures the blockade effect vanishes. The unique architecture of the necklace network results in a weak dependence of V_T on temperature which leads to room temperature single-electron effect.

The high sensitivity of the nanoparticle necklace network array at room temperature allows coupled live cells to electronically switch, or gate, the device through cellular metabolic activity. Additionally, the critical exponent, ζ, which is a measure of how current will rise during switching, can be significantly enhanced by cementing the necklaces with the dielectric material CdS, thereby greatly increasing the switching gain and sensitivity of the device. Given robust room temperature single-electron switching, enhanced ζ values, cellular coupling capability, and natural integrability with microelectronics circuitry, nanoparticle necklace network arrays have the potential to be implemented in a wide range of applications, such as, chemical sensors, biofuel cells, biomedical devices, and data storage devices.

ACKNOWLEDGEMENTS

Foremost, I would like to thank my adviser Dr. Ravi Saraf for his constant support throughout my graduate career. I am grateful for his unfaltering optimism, counsel, and thought provoking discussions. I would also like to extend my gratitude to my committee: Dr. William Velander, Dr. Kevin Van Cott, and Dr. Eva Schubert.

To my lab members, Sanjun, Vikas, Gaurav, Vivek, Raji, Subrata, Chris, Rafal, Chieu, and Jason, I thank you for your guidance and friendship over the years. Lastly, I would like to thank my parents Pam and Jerry Kane for a lifetime of love and support, a true gift.

TABLE OF CONTENTS

LIST OF FIGURES

LIST OF TABLES

LIST OF ABBREVIATIONS

U	Energy required to charge an island or nanoparticle by a single electron
V_T	Threshold voltage
$\Delta\varphi$	Electrostatic energy of an island or a nanoparticle
Q	Electrostatic charge
n	Number of uncompensated electrons in an island or nanoparticle
V_g	Gating potential
ζ	Critical exponent
α	Parameter related to the level of quenched charge density stored in the array
N	Average number of particles in the percolation path connecting the electrodes
$p(T)$	Temperature dependent fraction of nanoparticles or islands in the percolation path that pose a Coulomb blockade
T^*	Temperature at which the threshold voltage equals zero
$p(T^*)$	$p(T)$ at $T = T^*$
C	Capacitance of an island or a nanoparticle
C_1	Capacitance of the source electrode in a three-terminal single electron transistor
C_2	Capacitance of a drain electrode in a three-terminal single electron transistor
C_g	Capacitance of the gate electrode
C_Σ	Total capacitance of the device including C, C_1, C_2, and C_g
ε	Dielectric constant of the material surrounding the island or nanoparticle
ε_0	Electric field permittivity in vacuum
D	Diameter (or size) of the island or nanoparticle
k	Boltzmann constant

CHAPTER 1

INTRODUCTION

In a metallic wire at a fixed bias the electric field is constant leading to the well known Ohm's Law. The ability to induce local modulation in the electric field in an electrically conductive material by virtue of storing (local) charge leads to non-Ohmic behavior, a principle at the heart of all electronic devices. The generation of a local energy barrier due to charge pinning allows for the regulation of current through the device by external fields, such as, electric, magnetic or mechanical. This well known gating effect provides an avenue for making a variety of electronic systems, such as solar cells, electro-thermal devices, transistor based switches for microprocessors, and (micro/nano)sensors that respond to mechanical and/or chemical stimuli.

The phenomenon of non-Ohmic electron transport (and corresponding gating) through a single or an array of nanoscale size metal islands or nanoparticles has been recognized and developed for six decades.[1-8] In these systems, a principle feature is that electron transport through the particle(s) has single electron sensitivity to local (particle) charging. Thus, these systems are called Single Electron Devices (SEDs). The devices should be considered as classical systems since the current is governed primarily by electrostatic (charging energy) even though electron transport is governed by electron tunneling, a quantum mechanical feature. A review of the chemistry, physics and engineering of four principle array architectures will be discussed: the single particle device (0D array); (dense) two-dimensional (2D) ordered and disordered array; one-dimensional (1D) array;

and quasi-one-dimensional (quasi-1D) array. With the exception of 0D devices, the arrays are naturally integrable with conventional circuitry, similar to other nanostructures, such as nanotubes, nanowires and graphene.

Isolated Nanoparticle as a Single Electron Device

The simplest SED consists of a single metal island, such as a nanoparticle[9-17] (Fig. 1.1(a)) or a lithographically patterned metal island,[5,18-21] isolated by a thin dielectric barrier between two adjacent electrodes. For the island to be charged by a single electron, *e*, a charging energy, U, equal to $e^2/2C$ is required, where the capacitance of the particle is $C = 2\pi\varepsilon\varepsilon_0 D$, ε is the dielectric constant of the material surrounding the particle, ε_0 is the electric field permittivity in vacuum, and D is the diameter of the particle. In order for the island to hold charge, the dielectric barrier must have a (tunneling) resistance

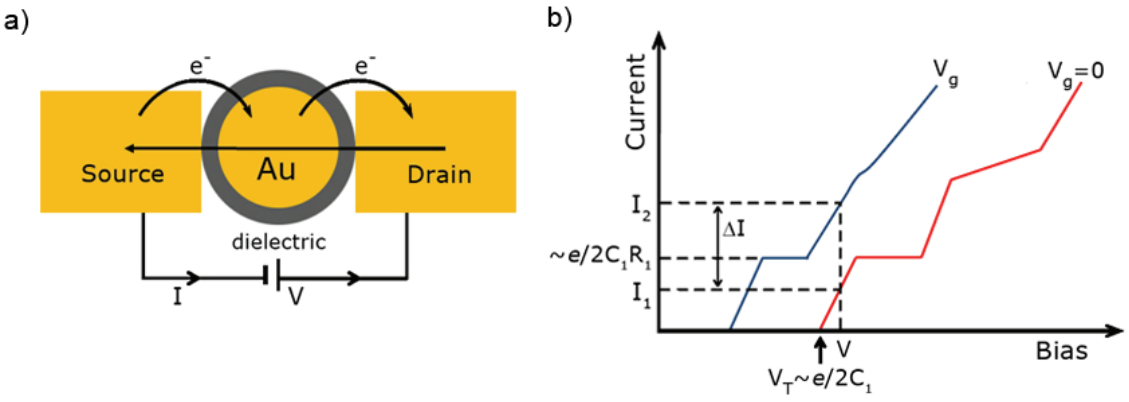

Figure 1.1 Structure and I-V characteristics of the single nanoparticle device. (a) Schematic of the single nanoparticle device where the electrodes are separated from the isolated nanoparticle (such as Au) by a thin dielectric barrier. (b) Typical I-V behavior showing the threshold voltage $V_T \sim e/2C_1$, Coulomb staircase as wiggles, and gating effect. Due to the gating voltage, V_g, V_T shifts and at an applied bias, V, the current changes from I_1 to I_2 (see Fig. 1.2(a)). The current for the first level of the staircase is $\sim e/2C_1R_1$.

significantly larger than quantum resistance, $h/2e^2$ (~13 kΩ), and be thin enough for an electron to tunnel.[22,23] The charging energy for a typical particle of D ~ 10 nm and ε ~ 3.5 is ~40 meV. As the thermal energy, kT, where k is Boltzmann constant and T is temperature, for an electron at room temperature is only ~25 meV, the electrostatic charging energy barrier of the particle will impede the tunneling probability of electron transport. This behavior is known as the Coulomb blockade effect. A key feature of the Coulomb blockade effect is that the current, I, through the particle as a function of applied bias, V, will be blocked below a threshold voltage, $V_T \sim U/e = e/2C$. Due to the broad energy distribution of free electrons within the metal particle, cryogenic temperatures, where U ~ 10 kT, are required for the observation of threshold behavior for a single particle device. For robust, room temperature operation, a U ~ 100 kT, or a V_T of ~2.5 V, is required.[24] Room temperature Coulomb blockade using D < 1 nm particles has been achieved with a large $V_T > 5$ V.[25] However, blockade characteristics are significantly smeared due to the high sensitivity to particle size variation caused by the quantization of the kinetic energy of the conduction electrons and the appreciable drift of current-voltage (I-V) features over time due to charge fluctuations.[26,27] Together, these two aspects significantly smeared the blockade characteristics of the device.[25] In addition to Coulomb blockade, single particle SEDs are characterized by quasi-periodic I-V undulations known as the Coulomb staircase. The staircase occurs as bias increases and the nanoparticle becomes sequentially charged by a single electron (Fig. 1.1(b)). Experimental observation of Coulomb blockade and staircase has been found for single nanoparticle devices.[10-16,28] The first SEDs were fabricated using lithographically patterned islands of ~100 nm diameter, which required liquid He temperatures to observe

a blockade effect. Smaller devices were fabricated using an ~1.8 nm island with a STM tip as an electrode that exhibited U in the <100 mV to 1 V range, allowing Coulomb blockade and staircase to be present at room temperature.[16]

Irrespective of dimension (0D to 2D), the defining feature of all SEDs is the effect that (local) charging of the nanoparticle(s) has on the tunneling current. If the capacitance of the system is small enough, such that the charging energy by a single electron is larger than the thermal energy, the (tunneling) current is affected by the charged state of the nanoparticle. In other words, electron transport through tunneling is driven by the reduction in the electrostatic energy of the nanoparticle by $\Delta\varphi$. Transport of a single electron into (or from) the particle causes a $\Delta\varphi$ that is well over a couple of kTs. With $\Delta\varphi/kT >> 1$, the tunneling (transmission) probability is proportional to $\Delta\varphi$, a fact that led to the proposal of the three-terminal transistor design (Fig. 1.2(a)).[4,22] In the single electron transistor, the nanoparticle is isolated from source and drain electrodes by $R_{1,2}$ and $C_{1,2}$. The particle has a charging energy of $e^2/2C$, a charging time of $\sim R_{1,2}C$, and is

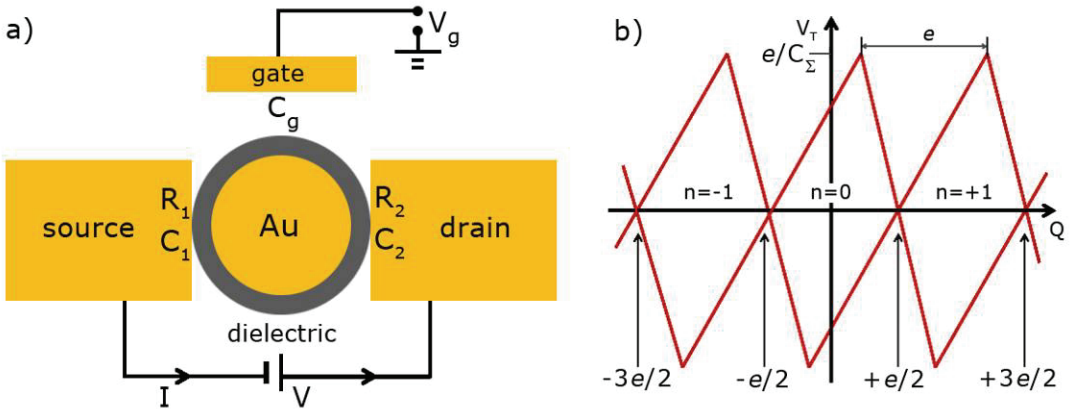

Figure 1.2 Electric properties of the single nanoparticle transistor. (a) Schematic of a single electron transistor made from a single nanoparticle. b) Schematic of Coulomb blockade oscillations showing the modulation of V_T as a function of $Q = -C_gV_g$, i.e., $Q \sim V_g$. V_T has a periodicity of $\Delta V_g = e/C_g$.

capacitively coupled to the gate electrode by C_g. Charge is localized in the particle when $R_{1,2} >> h/e^2$, according to the uncertainty principle. The importance of (static) charge localization will become apparent later in the discussion.

Current through the nanoparticle is modulated by the gate electrode. The particle contains a local charge of -n*e*, where n_1 and n_2 electrons come in and out of the particle, respectively, and $n_1 - n_2 = n$. At n = 0, the application of a gating potential, V_g, introduces uncompensated charge into the particle by $Q = -V_gC_g$. This charge addition increases the electrostatic energy potential of the particle, $\Delta\varphi/e$, by $\sim V_gC_g/C_\Sigma$, where C_Σ is the total capacitance of the device including C_g, resulting in a change of V_T. Due to a change in V_T, at an applied bias of V, the current through the particle will change from I_1 to I_2 (Fig. 1.1 (b)). Therefore, V_g is "gating" the current. There are two important features of gating due to V_g:[3,29-31] (a) the electrostatic (charging) energy, $\Delta\varphi$, will continue to rise until V_g (locally) polarizes the nanoparticle enough to induce one electron charge (i.e., Q = -*e*), leading to a maximum V_T of $\sim e/C_\Sigma$. The $\Delta\varphi$ will be identical for every incremental change in charge within the nanoparticle by *e*. (b) When V_g is increased beyond the maximum V_T condition, the polarization at the nanoparticle/gate interface diminishes and leads to a lowering of V_T. At a symmetric condition of $Q = (n \pm 1/2)e$, $\Delta\varphi$ vanishes, which suppresses the Coulomb blockade effect ($V_T = 0$) and causes the current through the device to display Ohmic-like behavior.[3,31] The V_T modulates with a periodicity of $\Delta V_g = e/C_g$, where $V_T = 0$ when $Q = (n \pm 1/2)e$ (Fig. 1.2(b)), and is called Coulomb blockade oscillation.[3,31] Coulomb oscillations are well studied, where experiments at low temperature agree remarkably well with theoretical predictions.[11-13,29,32]

The two disadvantages of a SED based on a single nanoparticle are: a) particle diameters of less than 1 nm are required for the Coulomb blockade effect to be robust at room temperature (i.e., U > 10 kT). However, quantization of the energy levels within the conduction bands of the particles becomes significant at these dimensions, thus leading to devices with high quantum noise and sensitivity to particle size. b) It is not simple to fabricate single particle SEDs.[33-36] One method of increasing the V_T value of an SED is by using a (self-)assembled array of nanoparticles (Fig. 1.3). This design alternative would allow particles of D >> 1 nm to be used, allowing easier fabrication methods to be employed and eliminating susceptibility to the quantized kinetic energy of the electron. In nanoparticle arrays, the collective storage of charge, i.e., capacitors in series, decreases the effective capacitance of the system.[7,8,37,38] This leads to V_T increasing by over an order of magnitude compared to single particle SEDs.

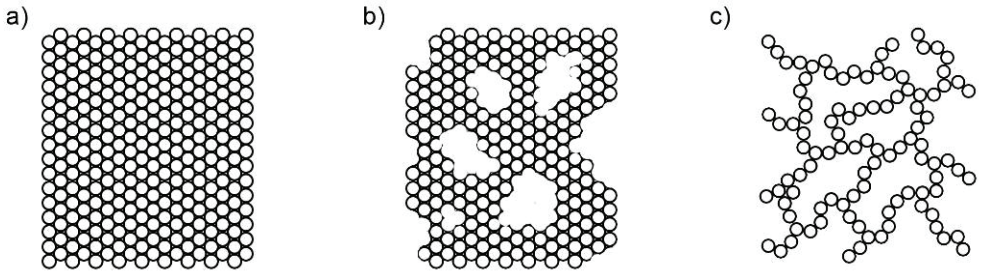

Figure 1.3 Representative array schematics. (a) A typical close-packed 2D array device. (b) A 2D array device with large (micrometer size) voids. (c) The quasi-1D nanoparticle necklace network array morphology is a 2D array with extreme voids connecting array branching points.

Two-dimensional Nanoparticle Array

A dense 2D array of conducting microparticles will demonstrate a slightly non-linear current, I, as a function of applied bias, V, due to an increase in the number of conducting pathways as tunneling barriers between particle/particle contacts are overcome by rising bias.[39,40] Compared to a microparticle array, an array of conducting nanoparticles (Fig. 1.3(a)), with a small enough capacitance to satisfy $e^2/C > kT$, has an I-V behavior that is highly non-linear.[8,37,41,42] As in the single nanoparticle device (Fig. 1.1 and 1.2), the array device exhibits a V_T. It is analytically argued that conduction in the array is akin to critical phenomena, where at a critical point, V_T, the correlation length (i.e., the percolation path) diverges when the two electrodes become connected by a percolation path.[7] Current at bias greater than V_T follows $I \sim (V/V_T - 1)^{\zeta}$, where ζ is the critical exponent.[7] The morphology of the percolation path (i.e., dimensionality and tortuosity) and the distribution of trapped charge influences ζ, which determines how current will rise beyond V_T. Trapped charge is shown to be stationary by simulations and is thus referred to as the "quenched charge distribution."[7,8] The percolation path can be deflected by trapped charges, which act as temporary blockades that may be overcome by increasing bias. By equating the quenched charge distribution of the array to the local charge of a single particle in a single electron transistor, it is reasonable to believe that the array can also be gated to modulate the I-V behavior. It is important to note that while nanoparticle arrays can be gated, microparticle arrays cannot be gated.

The array of nanoparticles has three distinct advantages. First, the larger, self-assembled structure allows for easier fabrication compared to a single particle device. Secondly, and

more importantly, for the same size particles the V_T will be greatly enhanced compared to a single particle device made from the same size of particles. The latter can easily be visualized by considering a single percolation path made up of N particles connecting the electrode. If the capacitance of a single particle is C, then the capacitance of N particles in series is ~C/N leading to $V_T \sim \alpha eN/C$, i.e., an αN fold enhancement, where α is a parameter that accounts for the level of quenched charge density stored in the array.[7,8,37,38] Drawing from the critical phenomenon analogy presented above, αN is the minimum number of steps needed to propagate the charging front to connect the source and drain electrodes.[7] Thus, it is analogous to a percolation path. The α parameter for dense 2D array is experimentally measured to be ~0.25,[37] which agrees well with simulation calculations that predict α in the range of 0.23 to 0.36, depending on the lattice geometry of the array.[7,38,43] The third advantage of the nanoparticle array is that the rise in current for $V > V_T$ will be enhanced. For a single particle system (Fig. 1.1 and 1.2), the I-V beyond V_T will be linear (except for the Coulomb staircase undulations), i.e., $\zeta = 1$. For 2D arrays, (as discussed below and shown in Table 1.1) $\zeta > 1$, predominantly >2. A larger ζ results in a faster rise in current for $V \geq V_T$, which translates into improved switching speeds.

There are a number of reports describing the fabrication of 2D array of nanoparticles. The arrays exhibit distinct properties depending upon the assembly method utilized. In array made by drop-casting or spin-coating, the particles self-assemble into close-packed monolayer films due to long-range dispersion forces during solvent evaporation.[44] By regulating the molecular length of the organic surfactant capping-ligands that encapsulate and stabilize the particles, interparticle distance can be controlled to obtain quantum

Table 1.1. Critical exponent for array as a function of dimension, temperature and order

Morphology	ζ, Scaling exponent	Temperature	Comments	Ref.
0D	1	All temperatures	Coulomb oscillation; nominally Ohm's Law; $V_T \neq V_T(T)$.	17,45
1D	1	0 K	Analytical; Infinite array.	7
	1	0 K	Simulation; 1 × 500 array; random quenched charge distribution.	46
	1.03 – 2.32	4.2 K	Experiment; 30 nm diameter carbon nanoparticle; 1.2 μm gap.	47
Quasi-1D	1.2 ± 0.1	300 K	Experiment; 1.4 nm diameter Au nanoparticle; 2 or 15 μm gap.	25,27
	1.45 ± 0.08	0 K	Simulation; 5 × 500 array; random quenched charge distribution.	46
	5/3	5 – 300 K	Experiment; 10 nm diameter Au nanoparticle; 10 and 20 μm gaps; ζ is temperature independent.	48
	1.6	195 K	Experiment; 1.4 nm diameter Au_{55} nanoparticle; 15 μm gap; 100 nm wide.	49
	1.95	8 – 120 K	Experiment; 5.5 nm diameter Au nanoparticle; 500 nm gap; 30 nm wide; ζ is dependent on temperature.	50
	3.36	296 K	Experiment; 10 nm diameter Au nanoparticle cemented with CdS; 50 μm gap.	51
	7.11	50 K		
2D: Ordered Arrays	5/3	0 K	Analytical; Infinite array.	7
	~1	5 K	Simulation; 26 × 26 array; ζ is dependent on temperature.	52
	1.6	300 K		
	2	0 K	Simulation; 400 × 400 array.	7
	2.0 ± 0.15	All temperatures	Simulation; 50 × 50 array; ζ is independent of temperature.	46
	2.25 ± 0.1	10 – 130 K	Experiment; 2.2 – 6.5 nm radius Au nanoparticle; 0.2 – 1.25 μm gap; 2 μm wide; ζ is temperature independent and highly reproducible.	8,37
	2.56 ± 0.09	4.5 K	Experiment; 1 μm gap; at high bias, ζ = 2.37 ± 0.05.	42
	2.2 – 2.7	2 K	Experiment; 10 × 10 array; 10 nm diameter Co nanoparticle;	53
	~3	5 – 300 K	Experiment; 1.8 nm diameter Au nanoparticle; 30 nm gap; ~20 – 50 nm wide; ζ is fairly constant with temperature.	54
	2 – 4	5 – 300 K	Experiment; 1.3 – 3.3 nm diameter Au nanoparticle; 15 – 40 nm gap; 50 nm wide; ζ is weakly dependent on temperature.	41

2D: Ordered Arrays with Quenched Charge Disorder (Simulation)	1.6	5 – 300 K	26 × 26 array; ζ is temperature independent.	[52]
	1.94	0 K	16 ×16 to 60 × 60 arrays.	[46]
	2.25	4.5 K	Void-free nanoparticle array.	[42]
2D: Disordered Arrays	1.8	5 – 300 K	Simulation; 26 × 18 array; random voids; ζ is weakly dependent on temperature.	[52]
	2.3	5 – 300 K	Simulation; 26 × 26 array; 37.8 nm gap; random voids; ζ = 1.9 at high quenched charge distribution.	[52]
	2.7	12 – 77 K	Experiment; 2.2 – 2.9 nm radius Au nanoparticle array with voids; at high bias, ζ = 2.16.	[37]
	4.14	4.5 K	Experiment; 3.6 μm gap; Micrometer-scale (2 μm) and nano-scale voids	[42]
	4.35	4.5 K	Experiment; 0.5 μm gap; Micrometer-scale (2 μm) and nano-scale voids; at high bias, ζ = 3.44.	[42]

resistance sufficient to hold charge.[55] As the length of the surfactant defines the interparticle separation distance (and thus the height of the tunneling barrier and capacitance), it has a significant effect on the electronic properties of the nanoparticle array. In order to ensure that spun cast array with electrodes are homogeneous, i.e., not influenced by dewetting effects caused by the electrodes, a two-step shadow masking technique can be used to deposit electrodes on top of the already formed array.[42] Nanoparticles capped with hydrophobic ligands have been shown to form a highly ordered monolayer on the surface of water.[56-58] The monolayer can subsequently be transferred onto a solid substrate by either using the Langmuir-Blodgett technique (vertically dipping and withdrawal of substrate)[56,57] or the Langmuir-Schaefer technique (contacting the surface of a substrate parallel to the surface of the film).[58] An innovative method that combines the Langmuir method and microcontact printing produces patterned 2D array.[59] Leveraging the surface reactivity of nanoparticles, monolayer and multilayer array can be assembled by cross-linking the particles with covalent bonding.[44,60] Array with specific bonding are more stable than those assembled by (weak) van der Waals forces.[61] Another method of forming 2D array is through a combination of a nanowire shadow mask and ion-beam milling.[54] This technique is proven useful because ion milling only removes the nanoparticles that are not protected by the nanowires, leaving the organic shells of the particles under the wires undamaged.[54] Different patterns of nanoparticles can be produced keeping the transport characteristics of the nanoparticles intact. 2D array fabrication can be performed by ink-jet printing of nanoparticles onto a substrate.[62] This method can easily be tailored to accommodate a range of materials and generate arrays with different morphologies.

Both experimental and simulation studies have been performed to relate ζ to the morphology of nanoparticle arrays (Table 1.1). Middleton and Wingreen (MW) were the first to analytically predict that the critical exponents for infinitely large 1D and 2D array at 0 K would be $\zeta=1$ and $\zeta=5/3$, respectively.[7] Experimental studies on 2D array observe a wide breadth of ζ, ranging from ~5/3 to ~4, due to the significant influence array morphology has on ζ (see Table 1.1). To investigate the effect structural disorder has on scaling behavior, the exponent values of a close-packed, ordered Au nanoparticle 2D array with low void fraction and a 2D array with high void density were evaluated at 4.5 K. Respectively, $\zeta=2.37 \pm 0.05$ and $\zeta=4$ were obtained, which is in good agreement with numerical simulations that predict $\zeta=2.25$ for the void-free ordered array and $\zeta=3.9$ for an array with high void density.[42] It is worth noting that the $\zeta=2.25$ found in the above simulation study is consistent with a previous experimental study on close-packed, long-range ordered 2D array using a different fabrication method and chemistry.[8] Other simulation studies on 2D ordered array obtain ζ values of 2.0 ± 0.15 and 1.94 ± 0.15.[46] As noted above, the quenched charge distribution imposes barricades to the conduction path between the electrodes that are sequentially overcome as bias is increased.[7,8] Because ζ depends on the topology of the percolation path, it is reasonable to expect that the exponent will also change as bias increases. Simulation and experimental studies show that a cross-over in ζ arises in larger, dense array, where the degree of freedom for percolation is higher.[37,42,52] In an experimental study, a change in ζ from 2.7 to 2.16 is observed as bias increases beyond $(V-V_T)/V_T \approx 2$ owing to a transition from 1D channels at low bias to highly branched 2D paths as the bias increases.[37] Simulation studies show a similar result where ζ crosses over to a smaller value at higher bias.[52] Interestingly, the

ability to compute current in each percolating path independently in the simulation studies shows that a further increase in bias causes the percolation paths to revert to becoming linear, forming smectic-like "streams", which causes a decrease in the tortuosity of the percolation path, thus lowering ζ.[52] To elucidate the effect of percolation path tortuosity and bias effects, a nanoparticle assembly combining micrometer-scale (2 μm) and nanoscale voids was studied across a range of different electrode gaps.[42] Array across 0.5 and 3.6 μm gaps show a very high ζ of 4.35 and 4.14, respectively, due to the complex void content that increased the tortuosity of the percolation path. Furthermore, for the 0.5 μm gap, a cross-over in slope to a lower ζ of 3.44 at increased bias is observed.[42] This experimental observation is consistent with simulations performed on square lattices of different sizes,[46] where larger gap width (i.e., larger system size) obeys a single power law.[42] Generally, experimental and simulation studies indicate that, unlike V_T, ζ is not a strong function of T. However, one simulation study on 2D disordered array shows that ζ for dense array weakly depends on temperature varying from 1.6 to ~1 for a temperature range of 300 to 5 K.[63] Furthermore, consistent with other studies, large void content increases the exponent from 1.6 to 2.3.[41]

Unlike a single nanoparticle device (Fig. 1.1 and 1.2), where V_T is independent of temperature, the threshold voltage of an array of nanoparticles linearly decreases as temperature, T, increases until T = T*, when the Coulomb blockade vanishes, i.e., $V_T(T^*) = 0$. Systematic simulation[46] and experiment[8] revealed a remarkable result – although V_T decreases, ζ remains constant. Since ζ is independent of T, the I-V curves for every

temperature ($T < T^*$) can be superimposed onto a single curve by simply translating them along the bias axis (with no translation along the current axis).[8,46] The $V_T(T)$ behavior is explained by building upon the percolation model proposed by MW.[7] As the temperature increases, a fraction of the Coulomb blockade "barricades," p(T), will vanish because the electrons have enough thermal energy to overcome them, i.e., the fraction of barricades posing blockade decreases as temperature increases. If the number of bias steps between the source and drain to move the charge is ΔV, then, $V_T(0) = \alpha N \Delta V$, i.e., αN steps are needed to have one percolation path connecting the source and drain electrodes.[7] As the p(T) fraction vanishes at higher temperature, $V_T = \alpha N \Delta V[1-[p(T)/p(T^*)]]$.[8] This yields the simple result that, $V_T(T) = V_T(0)[1 - [p(T)/p(T^*)]]$, where, $p(T^*)$, is the percolation threshold, which is dependent on the structure of the array. Typically, $p(T^*)$ is about 0.347, implying that only 34.7% of the barriers have to be overcome in order to achieve Ohmic behavior. If the charging energy distribution is assumed to be a linear decay with the maximum fraction of particles requiring zero charging energy, p(T) will increase linearly as T increases, which is consistent with experimental observation.[8] Consistent with simulation results,[46] 2D array devices show that V_T decreases linearly as temperature increases.[8,41,54] Thus, to build a robust single electron device operating at room temperature, three (design) criteria must be considered: (a) $V_T(0)$ should be as large as possible, i.e., α should be maximized; (b) the slope $p(T)/p(T^*)$ should be as small as possible to obtain a high V_T at room temperature; and (c) ζ should be as large as possible for high performance switching.

Another phenomenon that will significantly affect the performance of nanoparticle arrays as electronic devices is cotunneling. In the entire discussion above, the model assumes that the electron tunnels one junction at a time as it percolates through the array. However, it is possible to have several tunneling processes occurring at the same time at multiple junctions if the energy states are available. In other words, if there is no (particular) time limit for observing the tunneling process and the change in electrostatic energy is favorable, cotunneling across several junctions can occur in one step. The phenomenon is characterized by measuring differential conductance (dI/dV) at zero bias, g_0, as a function of temperature.[61,64-67] At low temperatures, $g_0 \sim \exp[-(T_0/T)^{1/2}]$ (i.e., cotunneling) crosses over to an activated process where, $g_0 \sim \exp[-E_a/kT]$, where E_a is the activation energy. The constant, T_0, is related to the hopping distance of the electron transport due to the cotunneling process. Experimentally, for multilayer and thick films of nanoparticles, the cotunneling hopping distance is about 4-5 particles.[68,69] Furthermore, the activation barrier for cotunneling rapidly increases as the dimensionality of the array reduces from 2D to 1D (or quasi-1D) array.[70] An interesting effect of cotunneling is that the I-V curve beyond the threshold voltage will rise significantly faster due to the effective "step" size of charge hopping across the electrode becoming 4-5 fold larger than by transport through tunneling alone. For example, with cotunneling the effective ζ can increase from ~2 to ~5.[68,69]

One-dimensional Nanoparticle Array

True 1D nanoparticle arrays, with single-file chain structure, are difficult to achieve. Theoretical predictions[71] and, relatively few, experiments[47,70,72] indicate that 1D array of

nanoparticles have electrical properties that are significantly different compared to 2D array. Similar to 2D array, 1D array will display a collective stored charge and, thus, an enhanced V_T. Juxtaposed to 2D array, whose close packing allows for the development of optimal percolation pathways around barriers, every tunneling barrier in a 1D array must be overcome in order for current to flow, as a result, α is predicted to be ~0.50 for a 1D[7] array, which is twice the experimentally determined value of α~0.25 found for 2D array.[37] Thus, given the increase in αN, a larger enhancement of V_T is observed in 1D array compared to 2D array. Studies have found that, as in 2D array, V_T is linearly related to array length for 1D systems and longer array lengths lead to higher V_T values.[70]

Similar to 2D array, in an early study, the $V_T(T)$ relationship for a 1D assembly of carbon nanoparticles was found to be linear for the temperature range of 10 to 75 K.[47] However, a recent study shows that the $V_T(T)$ relationship for 1D arrays possess two distinct slopes.[70] At low T, the $V_T(T)$ slope is linear, but as T increases, the $V_T(T)$ slope gradually reduces. This unusual behavior is unique to 1D array. A quasi-1D array having a width of 2-4 particles will not exhibit such sublinear $V_T(T)$ curves.[50,70] This phenomenon was theoretically predicted over 10 years ago[71] and later confirmed by experiment.[50,70] The sublinear behavior can be understood by expanding upon the $V_T(T)$ model presented for the 2D array discussed above. Starting at 0 K, as T increases, some of the barricades will vanish as the thermal energy of the electron increases. The decay of V_T with T will be linear. However, as T increases further, the larger barriers, whose energy is closer to the maximum, $\sim e^2/C$, will be more difficult to overcome, thus leading to a slower decay in V_T.[70] As will become apparent later, the decrease in slope at higher T in 1D array is

particularly interesting because it allows a higher T* to be achieved than if the decay was linear over the entire temperature scale.

Early work in the study of 1D devices relied primarily upon the random deposition[11] or induced alignment, by electrostatic[47] or magnetic[73] forces, of nanoparticles between lithographically patterned electrodes. Devices constructed by these means are typically short in length (only a few particles long) and lack position specificity. Much longer and position controlled 1D array can be developed through the template-assisted self-assembly (TASA) approach.[70,74] In TASA, templates are lithographically defined to have channel widths only as large as the diameter of the nanoparticle, making them amenable to the integration of nanoparticles through capillary force exploitation. Highly controlled, continuous 1D array monolayers are possible with TASA, whose main deficiency lies in template construction, since the channel width must be precisely controlled. Several 1D array fabrication techniques have recently been developed that are promising avenues for 1D device fabrication,[75-87] although electrical properties have not been studied. These techniques include contact printing with single particle resolution,[76] the stick-slip motion of an interface,[77] and the mineralization of metal particles onto DNA,[78] nanotubes,[79] peptides,[80] and polyelectrolytes.[81] Particles can also be deposited onto 1D templates such as CNT,[82] DNA,[83,84] polysaccharides,[85] electrospun nanofibers (Fig. 1.4),[87] and peptide microfibrils.[86] A 1D array of particles can be formed in solution by an intrinsic dipole, magnetic[88] or electric,[89] and an induced dipole.[51,90,91] Although the aforementioned fabrication techniques are promising, the achievement of long,

continuous 1D array of nanoparticles continues to be an obstacle to successful 1D device development.

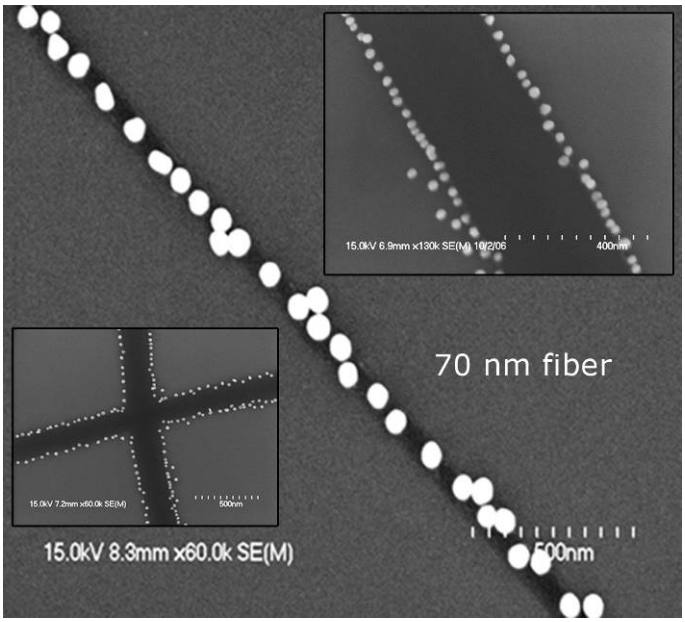

Figure 1.4. Self-assembled 1D array over large distances. Negatively charged 60 nm Au particles are deposited in single file on an electrospun fiber of positively charged poly(allylamine hydrochloride) (PAH). Inset images are of Au nanoparticles deposited along the edges of a PAH fiber. The array can be well over 100 μm long.

Quasi-One-dimensional Nanoparticle Array: Network of Nanoparticle Necklaces

Compared to 0D (i.e., single nanoparticle) and 1D devices, the architecture of 2D array has two principle advantages in terms of electrical performance: if the tortuosity of the percolation path is maximized, both α and ζ will increase, leading to a higher V_T and greater sensitivity to gating (i.e., gain). As mentioned above in the discussion of 2D array, large α and ζ can be obtained at a reasonably high I by increasing the dimensions

and void content of the device. One extreme approach to such a morphology would be a network of nanoparticle necklaces, which is essentially a 2D array with a void content so exaggerated that the array between the voids has a narrow quasi-1D structure.

Several methods have been reported describing the fabrication and electrical properties of quasi-1D devices. E-beam lithography was used to define a 4-5 particle wide array made up of D ~ 5.5 nm gold particles with ζ values ranging from 1.5-2.6 and a V_T = 2.5 V at 20 K.[50] The devices were prone to I-V curve fluctuations upon temperature cycling.[50] In another study, e-beam written ~100 nm wide arrays of D ~ 2 nm Au_{55} particles had a V_T = 6 ± 1V and ζ=1.6 at 195 K.[49] TASA was used to construct narrow 2D arrays with widths ranging from 1.5 (a zig-zag pattern) to 3 particle diameters.[70] The second type of quasi-1D structure, a network of 1D chains, was formed through the use of a Au nanoparticle decorated biopolymer scaffold.[25,27] Au particles with D ~ 1.4 nm were deposited onto a biopolymer scaffold to form 1D chains across an electrode gap of 2 or 15 μm that were found to have a ζ~1.2 and V_T = 12 ± 1V at room temperature.[25,27]

Recently, a versatile new method of assembling quasi-1D array made up of a network of nanoparticle necklaces (single-file particle chains) has been reported. Necklaces were self-assembled in solution and were deposited onto a substrate across electrodes by four methods: electrostatic attraction to the substrate,[48,51] a polymer fiber shadow mask defined patterning technique, patterning by inkless microcontact printing (IμCP), and self-assembly onto an electrospun nanofiber. Typically, a nanoparticle necklace device, made up of 10 nm Au particles with a 20 μm electrode gap, shows non-Ohmic I-V characteristics that maintain symmetry under forward and reverse bias without hysteresis.

A constant ζ=5/3 was found for temperatures ranging from 5-295 K. The key advantage of the method is the ability to "nano-cement" the particles together with a variety of (inorganic) materials to make highly robust arrays exhibiting large ζ, room temperature V_T, and high currents at a reasonable bias for devices spanning tens of microns. For example, 10 nm Au particles can be self-assembled into necklaces using the cation Cd^{2+} and subsequently cemented in solution by sodium sulfide to form the nano-cement CdS. A network of CdS cemented necklaces of 10 nm Au nanoparticles spanning across a 50 μm gap was shown to have a $V_T \sim 2.5$ V and 9.32 V and $\zeta \sim 3.36$ and 7.11 at room temperature and 50 K, respectively (Fig. 1.5). Interestingly, the ζ is constant over a very large range of $(V-V_T)/V_T$, indicating that the dimensionality of the percolation path remains invariant, indirect evidence of the quasi-1D nature of charge transport (inset Fig. 1.5).

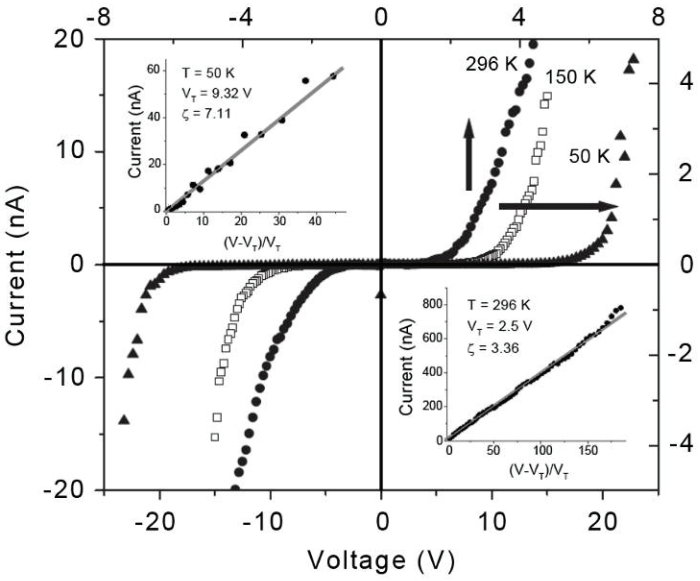

Figure 1.5. Single electron effect in the cemented nanoparticle necklace network. The I-V characteristics of a CdS nano-cemented 10 nm Au particle necklace network exhibit a very large V_T and ζ. As shown in the inset, unlike 2D structures, ζ is constant over a (very) large range of $(V-V_T)/V_T$. The two inset data plots are not shown in the published report.

A significant departure from previously reported arrays is the T versus V_T characteristics of the nanoparticle necklace network. The sublinear $V_T(T)$ characteristics observed in 1D devices is greatly exaggerated to a sharp transition (Fig. 1.6). The explanation for this behavior is founded on the model developed by Jaeger *et al*. Based on SEM images, the 1D necklaces in the network consist of "breaks," where one isolated particle has a resistance that is significantly larger than $>h/e^2$ and the surrounding 1D clusters. At low temperatures, the isolated single particles and the 1D clusters of the necklace trap charge to produce the random quenched charge distribution. As the temperature rises above 50 K, the thermal energy of the trapped charge overcomes the barrier for the larger clusters, thereby altering the quenched charge distribution. Subsequently, at larger temperatures, most of the trapping is confined to the isolated particles, which leads to a weaker disorder

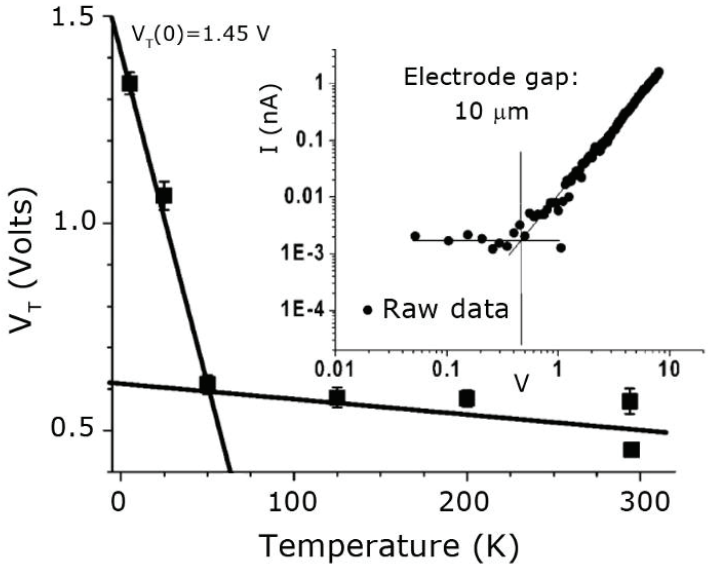

Figure 1.6. $V_T(T)$ characteristics of the nanoparticle necklace network. A 10 nm Au particle necklace bridged with H^+ ions and deposited between Au electrodes with a 10 μm gap shows a remarkable sublinear behavior with a sharp change in slope at 50 K. The inset shows a well defined V_T. Owing to the sublinear behavior, room temperature Coulomb blockade is observed even though the $V_T(0)$ is only 1.45 V.

and a smaller $V_T(T)$ slope, consistent with experimental and simulation studies. The ~50 K transition seems to be independent of the dimensions of the device and ζ remains unchanged through the transition. For an electrode gap of 20 μm, N ~ 2000 (at least), leading to an $\alpha \sim eV_T(0)/[N(e^2/2C)] \sim 0.053$, where $V_T(0) \sim 3.83$ V. The 5-fold smaller α for the necklace network compared to a dense 2D array (of α ~ 0.25) indicates an open structure with few charging centers, which is consistent with the isolated nanoparticle structure model. Arguably, perhaps the most important effect of the weaker dependence of V_T on T above 50 K is the presence of a finite V_T of ~0.45 V at room temperature for a 10 μm gap device, even though $V_T(0)$ is only 1.45 V, which translates into a robust switching energy of ~18 kT using 10 nm Au particles.

Application of Nanoparticle Arrays

While electronic devices made up of nanoparticle array are not extensive, nanoparticle arrays have found a plethora of applications in biology,[92,93] such as an agent for drug delivery, in cancerous cell ablation, and medical imaging.

The application of a multi-tunneling-junction nanoparticle array as an Ohmic device has been shown to a build a humidity sensor on living bacteria with a thousand fold better sensitivity than a microelectronic based device,[94] a tactile device to image touch at the resolution of a human finger an order of magnitude greater than conventional MEMS based devices[95,96] and an artificial nose to diagnose lung cancer.[97]

In the artificial nose, the resistance of the device changes when volatile organic compounds (VOCs) in an expired breath sample interact with functionalized arrays. Because a lung cancer patient expires specific VOCs at levels significantly different than healthy breath samples, the artificial nose can non-invasively diagnose lung cancer without the need for preconcentration.[97] Reports on the potential of nanoparticle arrays as single electron, non-Ohmic devices have been limited. One application is in a memory device that stores information by trapping charge with a gate potential and subsequently reading the information by the resultant shift in threshold voltage.[98] A network of nanoparticle necklaces was shown to exhibit switching by a living microorganism, that is, biogating, at room temperature.[48] Methanotrophic cells were seeded onto the array and subsequently exposed to methanol vapor. The metabolic activity of the live cells modulated the quenched charge distribution of the array which caused the current of the device to increase.[48] A magnetic device made up of nanoparticle necklaces is an additional potential application of the nanoparticle array as an SED. In a method similar to the one presented in Figure 1.5,[51] Cd^{2+} ions were replaced with Fe^{3+} ions and subsequently oxidized to form a magnetic iron oxide cement.[99] At room temperature the I-V behavior exhibits classic Coulomb blockade effect, where, upon application of a magnetic field (of about 70 mT), the V_T is modulated from 0.81 to 1.59 V, while the ζ of 2.1, a typical value for a 2D structure, remains unchanged. The invariance in ζ indicates that the percolation topology and quenched charge distribution is invariant (as expected) and that it is the barrier between the nanoparticles that is modulated by the magnetic field.

Summary and Conclusions

Electrical properties of single nanoparticle (0D), and their arrays in one (1D and quasi-1D) and two (2D) dimensions are discussed. All of these architectures exhibit a threshold bias, V_T, required for the passage of current, I, through the nanoparticle assembly. In general, for bias, $V > V_T$, $I \sim [(V-V_T)/V_T]^{\zeta}$, where ζ is a critical exponent. Studies in 0D show that a single nanoparticle can operate as a single electron transistor, where current is gated by regulating the charge in the particle in increments of *e* (the charge of the electron). The V_T modulates with gating potential at a periodicity of ~*e*/C, where C is the capacitance of the device. This modulation in V_T (and conductance) with gating potential is referred to as Coulomb oscillation. The sensitivity to (incremental) charging of the nanoparticle by a single electron is manifested as quasi-periodic wiggles in the current-bias characteristics, referred to as Coulomb staircase. Cryogenic temperatures are usually required to observe single electron effect, unless the particle is < 2 nm, in which case significant noise occurs due to the degeneracy of the kinetic energy of the electron.

Robust room temperature operating SEDs consisting of "large" nanoparticles, i.e., >5 nm, can be made by arranging the particles in an array. Arrays of nanoparticles do not exhibit Coulomb staircase or oscillations. Unlike a single particle device, in arrays, V_T is temperature dependent and increases as T decreases. Furthermore, in arrays $\zeta > 1$ (leading to larger gain), while for a single nanoparticle device $\zeta = 1$ (i.e., Ohm's law). In 2D arrays, ζ is typically ~2 and V_T increases linearly with decreasing T. The exponent, ζ, can be greatly enhanced by increasing disorder in the arrays by the incorporation of voids and disrupting order. Owing to a larger degree of freedom compared to 0D and 1D

systems, in 2D arrays, the ζ depends on bias. Cross-overs in ζ occur within two bias ranges: at low bias the ζ changes to a larger value as the percolation path transforms from a 1D to a more network-like topology as charge barriers are overcome; then, at high bias, ζ again lowers as the percolation path becomes 1D "smectic-like" streams. In 1D arrays, the ζ remains temperature independent but $V_T(T)$ dependence becomes non-linear. Unlike 2D arrays, where $V_T(T)$ is linear, the V_T of 1D arrays decreases at a faster rate at low T compared to higher T. An interesting array that amalgamates the advantages of both 1D and 2D arrays is a network of 1D necklaces of nanoparticles: (a) similar to a disordered 2D array (with a ζ of ~4), the ζ is greatly enhanced to as high as ~7. (b) Similar to 1D array, the $V_T(T)$ behavior is non-linear and exaggerated to exhibit a sharp (transition-like) cross-over to a lower slope at large T, therefore making it possible to achieve robust room temperature single electron behavior with "large" nanoparticles of 10 nm diameter. (c) Similar to 1D array, the ζ remains constant over a large range of biases, i.e., $(V/V_T - 1)$ from 0 to 50, thus, increasing the operating range significantly (we note in passing that such high biases have not been previously reported for nanoparticle-based devices).

The nanoparticle array device offers three salient advantages over single nanoparticle devices: (i) the switching voltage, V_T, can be enhanced order(s) of magnitude higher compared to a single particle, allowing room temperature operation; (ii) the rise in current, i.e., ζ, can be significantly increased from 1 (for a single particle device) to 7 (for a cemented nanoparticle necklace network, a quasi-1D array); and (iii) the arrays can easily be integrated with microelectronics circuitry. Nanoparticle necklace arrays, characterized by a substantial $V_T > 2$ V using 10 nm "large" particles, high ζ ~ 7, natural

integrability, and the ability to induce magnetic, electro-luminescent, and chemical sensitivity, is a promising platform for building nanoparticle-based SEDs.

CHAPTER 2

SELF-ASSEMBLY OF A MICROMETERS-LONG ONE-DIMENSIONAL NETWORK OF CEMENTED AU NANOPARTICLES

One-dimensional (1D) nanostructures are good candidate materials for use in electronic devices because they can act as both nanodevices and circuitry, allowing the integration of power sources and extraction of signals. Basic logic circuits,[100,101] a variety of chemical and biochemical sensors,[102,103] and devices with neural cell networks[104] have been produced using carbon nanotubes and nanowires in which the 1D nanostructure forms the wiring material as well as the device.[105] The use of necklaces of nanoparticles provides a highly versatile route for the production of 1D nanostructures in which both the chemistry of the nanoparticle and its diameter can be tailored. Necklaces of nanoparticles have been assembled using chains of DNA,[106] nanofibrils,[107] block copolymers,[108] functionalized ligands,[109] and polyelectrolytes[81,110] as scaffolds. In addition to scaffold-directed self-assembly, electric-dipole interactions between nanoparticles can also be used to make 1D necklaces.[89,111] However, in each of these structures there is no special interconnection between the particles beyond the physical contact that is mediated by the morphology of the scaffold. In this chapter, we demonstrate the self-assembly of a necklace of Au nanoparticles on a flexible polymer chain that is mediated by a linker ion that is subsequently used to cement the particles together with an inorganic material. The diameter of the Au nanoparticles was 10 nm, the polymer was poly(styrene sulfonate) (PSS) with a molecular weight of 5×10^5 Da, and the cementing material was CdS. Subsequent to necklace formation, the particles are

cemented together with CdS. The cementing process could be directly observed using transmission electron microscopy (TEM). The CdS "nano-cement" transforms the discrete nanoparticles making up the necklaces into an encapsulated, wire-like structure with widths (i.e., diameters) of ~10 nm.

2.1 MATERIALS AND METHOD

Formation of the Nanoparticle Necklace Network in Solution Using a Molecular Scaffold

The 10 nm Au particles used to make the network array are purchased from BBI International and have a concentration of 5.7 x 10^{12} particles per mL with pH 6. Citrate reduction is used to synthesize the particles which results in citrate ions becoming adsorbed onto the Au surfaces and imparting them with a negative charge. A cadmium perchlorate hydrate solution (Cd solution) of 1 mg mL^{-1} concentration is prepared and then sonicated for 2 h. Under constant stirring, 1 mL of Cd solution is added dropwise to 4 mL of Au solution, giving a total volume of 5 mL. The solution is stirred for ~18 h, during which time the solution color changes from wine-red to violet blue. This color change corresponds to a shift in the surface plasmon resonance (SPR) band from 525 nm for the Au solution[111] to ~620 nm with a shoulder at 525 nm for the Au-Cd solution (Fig. 2.1). Acting as a molecular scaffold, 200 μL of polystyrene sulfonate (PSS) (MW = 500,000 Da) at a concentration of 1 mg mL^{-1} is added to the Au-Cd solution and stirred overnight. To cement the particles together, a solution of Na_2S, at a stoichiometric ratio of 0.7 times the amount of Cd in the Au-Cd-PSS solution, is added under dark conditions. The addition of Na_2S changes the SPR spectrum considerably, as the peak at 620 nm moves back to 540 nm. Inert nitrogen conditions are maintained during the entire synthesis process.

Characterization Equipment

The UV-vis absorption spectra of the liquid solutions are measured using an Ocean Optics Model USB2000 spectrometer with a 1 cm quartz cuvette holder. Transmission Electron Microscopy (TEM) and Energy Dispersive X-ray Analysis (EDX) is performed using a Hitachi H-9000 NAR with carbon film coated copper grid sample holders. Photoluminescence spectrums are measured with a Hitachi F-4500 spectrophotometer. A home-built I-V system is used to perform electrical property characterization. Current is measured with the highly sensitive multimeter, Agilent 3458A, and bias is applied with an Agilent 6613C power supply. A variable temperature cryostat by Oxford Instruments Superconductivity is used to conduct I-V studies at a range of temperatures.

Microelectrode Chips

The cemented nanoparticle necklace network array devices are fabricated using a microelectrode chip with a 500 nm thick thermal oxide layer, 50 nm thick titanium adhesion layer, and 300 nm thick Au electrodes. Electrode gap spacings of 50 μm are formed using photolithography patterning.

2.2 FORMATION OF A CADMIUM SULFIDE CEMENTED NANOPARTICLE NECKLACE NETWORK

Citrate-functionalized Au nanoparticles (Au solution) are formed into necklaces using cadmium ions by adding a 1 mg mL^{-1} concentrated cadmium perchlorate hydrate solution (Cd solution) dropwise into the Au solution until a volume ratio of 1:4 (Cd solution:Au solution) is obtained. Initially, the Au solution has a wine-red color and a corresponding SPR adsorption band at ~525 nm (Au curve in Fig. 2.1).[111] After ~18 h of stirring, the Au-Cd solution is violet blue in color and the SPR band has red-shifted to ~620 nm with a shoulder peak at 525 nm (Au-Cd curve in Fig. 2.1). Analysis of the Au-Cd solution

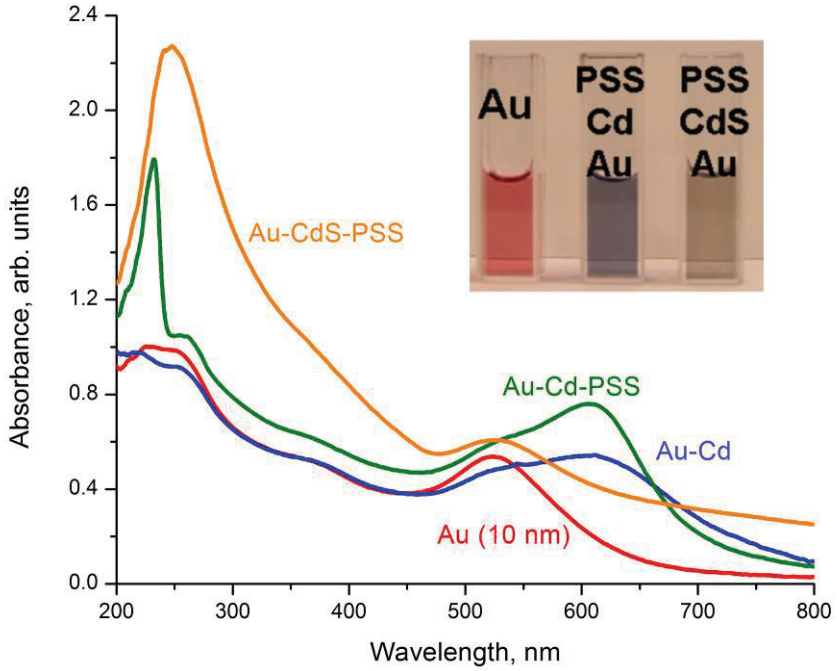

Figure 2.1. UV-vis absorption spectra at the various stages of necklace formation. SPR bands for the 10 nm Au particle solution, the Au-Cd solution, the Au-Cd-PSS solution, and the cemented Au-CdS-PSS solution. Inset: Cuvette images highlighting the color change of the solution for each formation stage. Solutions change from wine-red, to blue, and then to yellow brown.

using TEM indicates that there are only a few isolated Au particles (Fig. 2.2). Therefore, it is probable that the SPR band shoulder at ~525 nm is due to electron plasmon motion

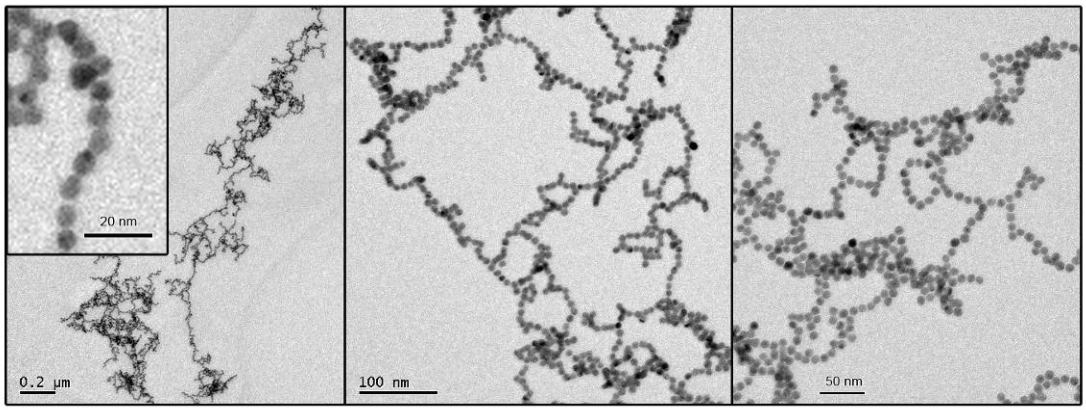

Figure 2.2. TEM images for the uncemented nanoparticle necklace. Discrete Au particles are bridged into long 1D necklaces through Cd^{2+} interparticle bridging and PSS scaffolding. The images indicate that few individual particles are in the Au-Cd-PSS assembly. Inset: Interparticle distance is 1 – 2 nm.

along the short axis (10 nm diameter) of the 1D necklace of nanoparticles. The red-shift in the SPR band of the Au-Cd solution is a result of the electrons of the Au particles becoming delocalized along the 1D necklaces.[90,109] The necklace assembly process begins when divalent Cd^{2+} ions partially compensate the immobilized negatively charged carboxylic acid groups from the citrate ions on the particles. As the nanoparticles come close together during thermal collision, the Cd^{2+} ions on the particle surface induce an electric dipole. Once the attractive force of the induced dipole reaches ~kT, the particle dipoles align and "polymerize" into long 1D necklaces of nanoparticles,[48,51,112] changing the solution from wine-red to violet blue. Necklace formation takes ~18 h due to the slow collision rate of the particles. If kept constantly stirred, the Au-Cd solution will remain stable for 1 to 2 weeks.

The ratio of Cd solution:Au solution is a critical factor in necklace formation. As noted above, for a ratio of 1:4, long necklaces with an SPR band peak of ~620 nm form. However, when the ratio is increased above 1:4, the solution precipitates due to the overcompensation of negative citrate ion charges by Cd^{2+} ions. If the ratio is reduced below 1:4, such as 0.5:4, there are not enough Cd^{2+} ions present to effectively polymerize the necklaces. Short necklace chains develop that have an SPR band peak at ~550 nm.

The polymer polystyrene sulfonate (PSS) is used as a molecular scaffold to direct the self-assembly of necklaces, guiding the clustered 1D chains into a longer, more exfoliated network. PSS, at a volume of 200 μL and concentration of 1 mg mL^{-1}, is added to the Au-Cd solution and stirred for ~18 hr. The negatively charged sulfonate groups of PSS prefer to attach to the free Cd^{2+} ions on the Au surfaces not involved in bridging the Au-Cd necklaces together.[113] Incorporation of PSS in the Au-Cd solution results in the appearance of a peak at ~265 nm in the SPR band, attributed to the absorbance of PSS (Au-Cd-PSS curve in Fig. 2.1). In addition to functioning as a scaffold, the PSS adds steric and electrostatic hindrances to the nanoparticle necklaces that increase solution stability considerably. Solutions of Au-Cd-PSS show no color change and have a constant SPR band for over 6 months. The presence of a quasi-1D nanoparticle necklace network on PSS chains is visible using TEM (Fig. 2.2). Particles within the necklaces have an interparticle distance of 1 – 2 nm.

The CdS nano-cement is formed by adding sodium sulfide (Na_2S) to the Au-Cd-PSS solution at a ratio 0.7 times the stoichiometric ratio with respect to the amount of Cd^{2+} in the necklace solution. The Na_2S addition converts the Cd^{2+} ions bound to the necklaces

into CdS. Following the formation of CdS, the SPR band of the necklace solution shifts from a peak at ~620 nm back to ~540 nm (Au-CdS-PSS curve in Fig. 2.1), indicating that the plasmonic coupling of the Au particles is weakened by the higher dielectric constant of CdS compared to the ionic bridge (Cd^{2+} and citrate ions). SPR analysis of the Au-CdS-PSS solution shows a CdS shoulder at ~415 nm that is highly blue-shifted when compared to a bulk CdS SPR band of ~510 nm, indicating that the CdS is in the form of interparticle cement.

The formation of cement around the Au nanoparticles is observed with TEM (Fig. 2.3). Upon Na_2S addition, the necklaces are transformed into continuous wires where nanoparticle silhouettes appear as nodes in the wire. With a wire width of ~10 nm, it is apparent that the wire was formed out of a 1D nanoparticle necklace. Regions of ~20 nm wire width are the result of necklace entanglements present before cementing. The

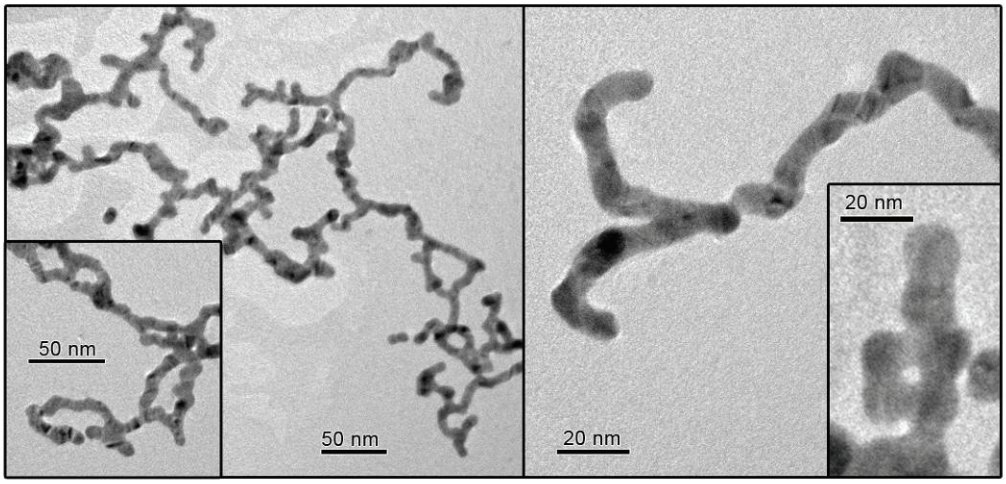

Figure 2.3. TEM images of the CdS cemented nanoparticle necklace. The addition of Na_2S to the Au-Cd-PSS assembly results in the formation of CdS cement. The cemented necklaces appear as continuous wire-like structures with diameters of ~10 nm.

morphology of the cemented necklace keeps the characteristic branches, loops and length of the uncemented necklaces (Fig. 2.2). TEM characterization indicates that TEM sample processing does not fracture the cement, demonstrating that the cemented necklaces are robust enough to be developed into a network array device.

Elemental Analysis is performed using Energy Dispersive X-rays (EDX) on the cemented solution during TEM characterization. A 60 nm beam spot size is used. The EDX spectrum indicates the presence of Au and CdS in the cemented necklace (Fig. 2.4). A Cu peak is observed due to the Cu grid used in sample preparation and a Cr peak is attributed to the sample holder of the TEM instrument.

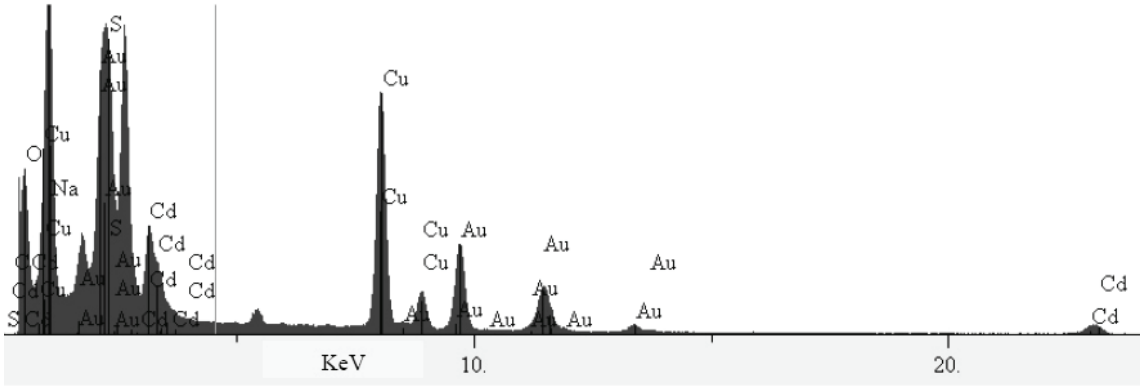

Figure 2.4. Elemental analysis of CdS cemented necklaces. Energy dispersive x-rays (EDX) are used to perform an elemental analysis of the cemented necklace solution with a 60 μm beam size. The EDX spectrum shows the presence of Au, Cd, and S in the sample. The Cu peaks are due to the copper grids holding the TEM samples. The ~5.7 KeV peak is due to the chromium of the TEM sample holder.

2.3 FABRICATION OF A NETWORK ARRAY DEVICE

Network array devices are created by depositing the negatively charged cemented Au-CdS-PSS solution onto a cationically functionalized (positively charged) substrate surface by electrostatic attraction. The substrate is a microelectrode chip consisting of a silicon (Si) chip with a passivating 500 nm thick thermal oxide (SiO_2), a 50 nm thick titanium adhesion layer, and 500 nm thick Au electrodes spaced 50 μm apart from each other.

2.4 ELECTRICAL CHARACTERIZATION OF A NETWORK ARRAY DEVICE

A CdS cemented network array device with a 50 μm gap exhibits non-linear I-V behavior with a threshold voltage, V_T, at room temperature (Fig. 2.5). Current at bias beyond $V > V_T$ flows according to $I \sim (V-V_T/V_T)^{\zeta}$, where ζ is the critical exponent.[7] The analytically determined critical exponent, ζ, for 2D arrays is 5/3.[7] Both ζ and V_T are estimated using a non-linear regression curve fitting method (see Appendix A). A $V_T \sim 2.5$ V and $\zeta \sim 3.36$ at room temperature is determined. The critical exponent of the CdS cemented network array device increases as temperature is decreased. At 150 K, $\zeta \sim 4.89$ and by 50 K a large $\zeta \sim 7.11$ is exhibited (Fig. 2.6). The complex ζ behavior of the cemented network array device is attributed to the fact that the CdS interparticle cement is a high dielectric material capable of storing charge.

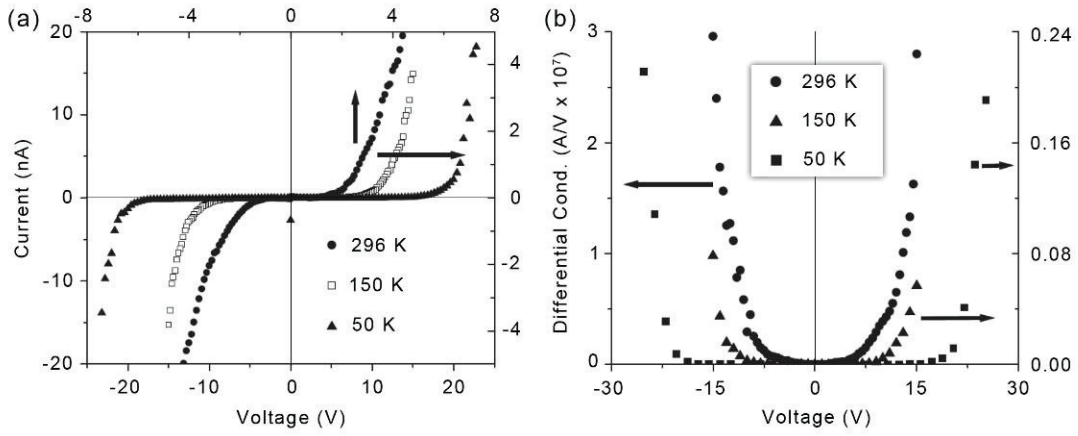

Figure 2.5. Electrical behavior of the cemented nanoparticle necklace network array. a) A 50 μm device exhibits non-linear I-V behavior. As temperature decreases, V_T increases from 2.5 V at room temperature to 9.32 V at 50 K. b) Differential conductivity for the 50 μm device in (a).

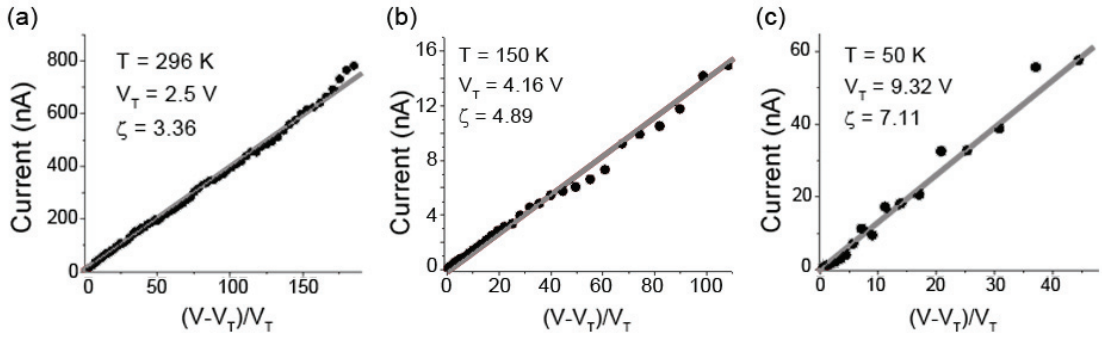

Figure 2.6. The effect of temperature on ζ. The critical exponent for a 50 μm device is studied at three temperatures for a large range of bias. a) At 296 K the device shows a V_T = 2.5 V and ζ = 3.36. b) V_T increases to 4.16 V and ζ is 4.89 at 150 K. c) At 50 K, the V_T = 9.32 V and ζ = 7.11.

As the temperature is lowered from room temperature to 50 K, the V_T of the device increases from ~2.5 V to ~9.32 V, a behavior consistent with experimental[8,41,54] and simulation[46] studies of 2D arrays. The expected V_T for a single isolated particle with diameter D = 10 nm and dielectric constant ε = 3, is $V_T = e/2C = e/(4\pi\varepsilon\varepsilon_0 D) \approx 50$ mV. The corresponding barrier energy, U, is 50 meV, or 2 kT at room temperature. For the above equation, C is the capacitance of the particle, ε_0 is the electric permittivity in vacuum, and *e* is the charge of an electron. The calculated V_T ~ 50 meV for a single particle is drastically different from the experimentally derived V_T ~2.5 V for the cemented nanoparticle necklaces.

The heightened V_T for the network array device can be explained by modeling the necklace as a percolating structure interspersed with nanoparticle islands made up of one (singlet), two (doublet) or more particles (Fig. 2.7). The islands are isolated particles that are not attached to the percolating nanoparticle chain due to interparticle gaps. These

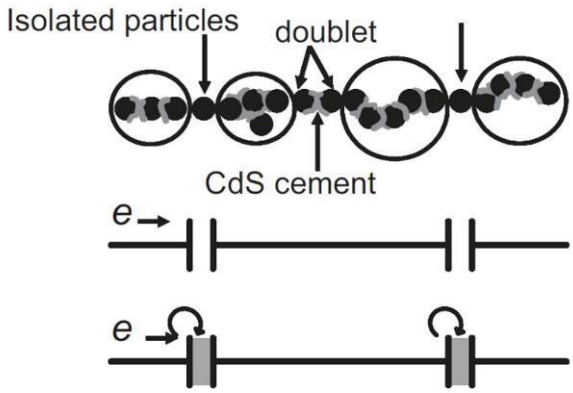

Figure 2.7. Schematic of the cemented nanoparticle necklace. Large clusters (enclosed in circles) are cemented together with CdS and act as wires within the necklace array. Isolated single particles (singlets), doublets, and other short chains punctuate the necklace and act as classic Coulomb blockade island devices.

gaps may arise due to the inability of cement to form or possibly the fracture of the cement during processing. In this model, the nanoparticle islands are coupled to the percolating necklace through tunneling junctions that mirror classical Coulomb blockade device theory. Thus, the islands are viewed as individual Coulomb blockade devices and the long percolating necklaces as wires.

Across the 50 μm electrode there are many percolating necklaces punctuated with isolated nanoparticle islands. At room temperature, the islands consist of clusters of "single" particles (i.e., singlets). Since the island particles are in series across the 1D necklace of nanoparticles, the net capacitance, C_T, is found by using series addition:

$$\frac{1}{C_T} = \frac{1}{C} + \frac{1}{C} + \ldots = \frac{n}{C} = \frac{n}{2\pi\varepsilon\varepsilon_o d} \qquad \text{Eqn. (2.1)}$$

where n is the number of clusters. An effective particle size of d/n leads to a threshold voltage of $V_T = e/2C_T = n(e/2C) = nV_1$ for the network array, where V_1 is the threshold voltage for a single particle. For the achievement of a $V_T \sim 2.5$ V at room temperature for a device with a 50 μm gap, the number of island singlets is estimated to be $n \sim 50$ (with $V_1 = 50$ mV). In other words, a typical electron percolating across a 50 μm gap will encounter only 50 isolated defects within the array.

As the temperature is decreased below room temperature, kT is lowered and larger clusters like doublets or triplets form into Coulomb blockades. When the large clusters are incorporated into Equation (2.1), the net capacitance drops, which in turn leads to a larger V_T. Additionally, the Coulomb blockade voltage will become broader at low temperatures due to the distribution of cluster size. The broadening of V_T in response to temperature has been observed in Au island devices with a 1D array[114] and 2D array morphology.[8]

2.5 SUMMARY AND CONCLUSIONS

A method to fabricate an electrically conducting network of 1D Au nanoparticle necklaces that exhibits remarkable Coulomb blockade effects was presented. Long 1D nanoparticle necklaces form through Cd^{2+} interparticle bridges. Necklace length and stability were increased by the inclusion of PSS. The particles making up the necklaces were cemented together by the addition of Na_2S, which transformed the Cd^{2+} ions on the surface of the Au particles into CdS. Although only Cd^{2+} ions were used in this study, the necklace formation process is highly adaptable and it is expected that a wide range of cations could be utilized. Therefore, the "nano-cement" of the necklaces can be tailored to suit a range of device specifications.

The CdS nano-cemented network array devices exhibited single electron behavior with a room temperature threshold voltage of $V_T = 2.5$ V and a $\zeta > 3$. As T was decreased to 50 K, ζ significantly increased due to the charge storing capacity of the CdS dielectric cement. A device with a high ζ is amenable to the development of a single electron sensitive switch that displays large gain at room temperature. The devices could be important for applications in nanoelectronics and sensors.

CHAPTER 3

SELF-ASSEMBLED NANOPARTICLE NECKLACES NETWORK SHOWING SINGLE-ELECTRON SWITCHING AT ROOM TEMPERATURE AND BIOGATING CURRENT BY LIVING MICROORGANISMS

A possible approach to building a hybrid bionanodevice that is powered or regulated by a microorganism is to electronically couple it to a nanodevice sensitive to the production of a few electron charges from the cell due to its biochemical activity, and the nanodevice is chemically nontoxic to the cell. A single nanoparticle behaves as a robust standalone switch such that the current through it can be modulated by a single electron altering the charge (or discharge) state of the particle.[24] Transistors and logic devices which use a single nanoparticle have been demonstrated to modulate current using that single nanoparticle.[11,12] The key parameter of the device is the Coulomb blockade voltage, V_T, above which the current switches on, that is, suddenly begins to increase.[24] The current is turned ON when the Coulomb blockade is overcome due to a single electron charge of barrier energy, eV_T, where e is the charge of an electron.

The nanoparticle-microorganism system seems ideal for building hybrid bionano-electronic devices where the (few) redox electrons from a cell or microorganism can, in principle, modulate the current through the particle by altering the charge state of the nanoparticle. However, cryogenic temperatures are required for these single particle, single-electron devices since the barrier energy for switching, eV_T, is small, <100 meV, for a typical 10 nm Au particle.[24] Coulomb blockades at room temperature can be

obtained by a single particle <1 nm;[25] however, quantum noise and charge fluctuation make the devices very noisy.[26,27]

The switching voltage, V_T, and the corresponding switching barrier energy, eV_T, can be enhanced by over an order of magnitude using a two-dimensional (2D) array of nanoparticles. In recent years, on the basis of theoretical predictions,[7] 2D arrays of nanoparticles that are easy to interconnect with electrical circuits have been demonstrated to exhibit similar switching behavior[37,41,42,54] and robust V_T above 1 V. Using some aspects of self-assembly, several top-down approaches, such as utilization of thiol-ligated Au nanoparticles,[53,115-117] assembly at the solvent-air interface,[118,119] and a live bacterium surface,[94] have been developed to fabricate 2D arrays interconnected to circuitry. Unfortunately, the over 10-fold enhancement compared to a single nanoparticle caused by several Coulomb blockades over the percolation path in the array vanishes at room temperature because V_T decreases (linearly) as temperature, T, increases.[8,41]

Although not studied for its Coulomb blockade properties (and subject of this report), an alternative architecture is a monolayer of 1D array of particles. A 1D array can be made using three possible approaches. Clusters of 1D arrays are synthesized by mineralization of (usually noble) metal from salt precursors or seed on a variety of 1D templates, such as DNA,[78] peptides,[80] nanotubes,[79] and polyelectrolytes,[81] to form a broad size distribution of particles, either discrete or continuous nanowires. In the second method, (monodispersed) nanoparticles are self-assembled on templates, such as CNT,[82] DNA,[83,84] polysaccharide,[85] and peptide microfibrils,[86] to form a discrete (i.e., insulating) 1D array. In the third method, an intrinsic magnetic[88] or electric[89] dipole, or induced

electric dipole, of the particle is used to self-assemble 1D necklaces of nanoparticles. The electric dipole can be induced by either replacing the immobilized ionic moiety with a neutral species[90] or partially neutralizing the charge with mobile ions.[51,91] In the third method, the particles are in close proximity for electron tunneling which is manifested as a red shift in surface Plasmon absorption spectrum[90] and non-ohmic conductivity of the 3D network (i.e., several monolayers) deposited between electrodes.[51] Although the optical application of "Plasmon wave guide" aspect of the necklace is well reported,[120] the (interesting) electrical properties of monolayer of 1D necklaces are not as recognized. This report describes a novel architecture composed of a 2D network (i.e., monolayer) of 1D nanoparticle necklaces of 10 nm Au particles where, for the first time, robust single-electron switching, that is, V_T, is observed at room temperature. Necklaces of nanoparticles were self-assembled in solution by an induced electric dipole mediated by ions and deposited on solid substrate to form a well over 1 mm large 2D network (i.e., monolayer) of 1D Au nanoparticle necklaces. Unlike our previous study[51] that used a 3D network mediated by Cd^{2+}, a toxin to living cells, the reported study is a 2D network mediated by H^+ ions. The room temperature switching occurs because, unlike the 2D (ordered or disordered) array, V_T becomes nominally independent of T above 50 K for this necklace architecture.

The robust V_T at room temperature and nontoxic nature of the necklace allows the possibility of developing a hybrid bionanodevice with living cells. Biogating the necklace network by depositing live yeast cells is demonstrated. As the cells are fed a nutrient (methanol vapor), the metabolic activity modulates the current through the

network. The biogating effect is caused by a redistribution of the quenched charge distribution[7] of the array by the electrochemical reactions elicited by the cells. The process is comparable to a three-terminal single electron transistor,[4,22] where instead of an external gate a live cell is implemented. Response times for the device are consistent with the metabolism kinetics of the cell.

3.1 MATERIALS AND METHOD

Formation of the Nanoparticle Necklace Network in Solution

The nanoparticle necklace network is made up of Au particles with 10 and 60 nm diameters at concentrations of 5.7 x 10^{12} and 2.6 x 10^{10} particles mL^{-1}, with pH 6 and 8, respectively, and are purchased from BBI International. For both solutions, the Au particles are electrostatically stabilized with the tri-sodium citrate dihydrate ($Na_3C_6H_5O_7 \cdot 2H_2O$) capping agent to give them a negative charge. A solution consisting of 60 and 10 nm particles at a volume ratio of 1:6, respectively, is prepared (Fig. 3.1(a)). Necklaces are formed by inducing an electric dipole by the dropwise addition of 120 µL of 10 mM HCl into 270 µL of the Au particle solution mixture under constant agitation. The H^+ ions bind to the negative citrate ions, partially compensating the charge of the particles (Fig. 3.1(b)). Given the high mobility of the H^+ ions on the citrate monolayer, an electric dipole is induced (Fig. 3.1(c)) when the particles are brought in proximity by thermal motion.[51] The polarized nanoparticles align and "polymerize" into long 1D

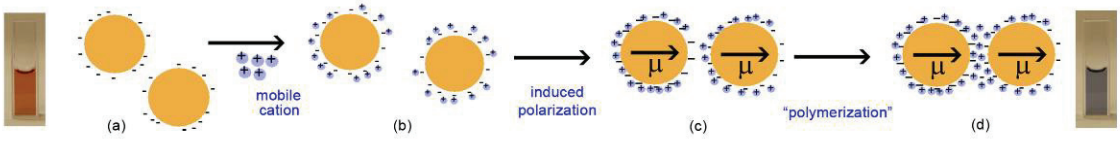

Figure 3.1. Schematic of the polymerization of nanoparticles. a) Unmodified 10 and 60 nm Au particles have a wine-red color and negative charge. b) H^+ ions partially charge compensated the Au particles. c) An electric dipole is induced in the nanoparticles. d) Dipoles align and "polymerize" the particles into long chains. The blue color of the solution indicates necklace formation.

chains, or necklaces (Fig. 3.1(a)). As the necklaces form, the free electrons of the nanoparticles become delocalized and cause a red shift in the surface plasmon absorption band of the solution.[90] This allows the formation of the nanoparticle necklaces to be monitored by UV-vis spectroscopy in real time. The nanoparticle solution changes from wine-red to violet blue in ~18 hours, where the blue color is indicative of necklace formation (Fig. 3.1(d)). The resulting nanoparticle necklace solution has a pH of ~2.3. Although not understood, the inclusion of 60 nm Au nanoparticles in the solution significantly increases necklace formation kinetics and maintains solution stability for over one week.

Characterization Equipment

Formation of the nanoparticle necklaces in solution is monitored using an Ocean Optics Model USB2000 spectrometer. Network array deposition and morphology on solid substrates is studied with a Hitachi S-4700 Field-Emission Scanning Electron Microscope (FESEM). Electrical property characterization (I-V behavior) is performed using a home-built system with a high sensitivity multimeter, Agilent 3458A, to measure current and an Agilent 6613C to supply bias. Temperature studies are conducted using a variable temperature cryostat by Oxford Instruments Superconductivity. Network array devices coupled with *P. pastoris* cells are studied in a sealed bell jar setup. The setup contains a water reservoir to maintain ~70% humidity, a heating element to keep the biotransistor at 26ºC, and a methanol reservoir.

Optical Analysis of the Nanoparticle Necklace Network in Solution

UV-vis spectroscopy is used to monitor the "polymerization" process (Fig. 3.1) by measuring the surface plasmon resonance (SPR) absorbance of the solution (Fig. 3.2). The SPR spectra of the Au particles changes from having peaks at ~525 nm and ~535 nm for the 10 and 60 nm particles, respectively, to one broad peak at ~610 nm for the unified nanoparticle necklace network (Fig. 3.2). The shoulder peak at ~525 nm is the plasmon wave along the short axis (10 nm particle diameter) of the long 1D necklaces. There is a red shift in energy for the necklace solution as a result of electrons delocalizing along the necklaces.[109] Necklace formation, manifested by a change in solution from wine-red to violet blue, takes ~18 hours due to the slow collision rate of the particles.

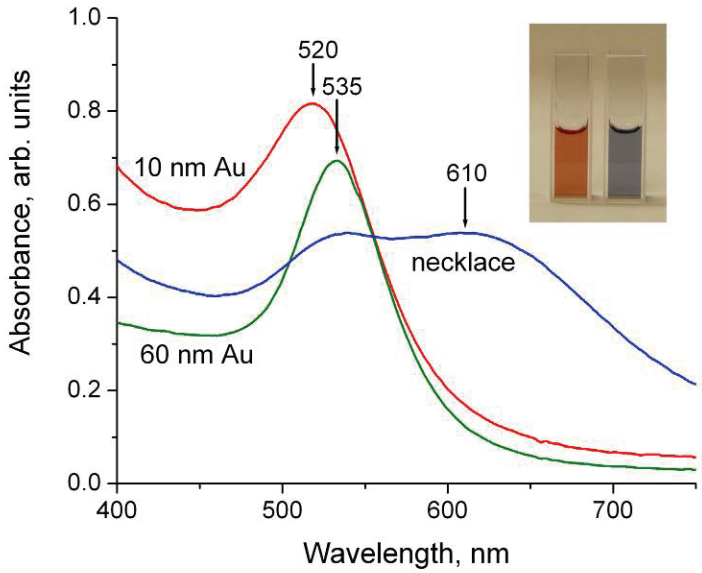

Figure 3.2 UV-vis spectrums of the nanoparticle solutions. UV-vis absorption spectra in solution at various stages of necklace formation. The SPR absorbance band for 10 and 60 nm Au particles is at ~535 and 520 nm, respectively. Upon formation of necklaces, the SPR band red shifts to ~610 nm and the solution color changes from wine-red to violet blue. Inset: Cuvette images indicating solution color change.

Cell Cultures and Deposition

Prior to coupling with the network array device, *Pichia pastoris* yeast cells are grown in media with methanol as the carbon source for 24 hours. Methanol inclusion induces the development of methanotrophic metabolic pathways within the cells and allows methanol vapor to be used as a food source for the cells during device testing. Yeast cells are coupled to the array by immersing the device into a yeast solution and subsequently rinsing well with water (pH 7). Approximately 200 yeast cells are deposited onto a device that is 10 μm long and ~1 mm wide. The deposited, or seeded, cells are ~2 μm in diameter and can survive in air for ~14 hours at a humidity of 70% and temperature of 26°C. Cell deposition is confirmed using a Leitz Aristomet optical microscope (Fig. 3.1(a)). Following biotransistor testing, samples are characterized using a Hitachi S-4700 Field-Emission Scanning Electron Microscope (FESEM). Yeast cells have a preference for the nanoparticle necklace array, as demonstrated by a higher deposition density on the array compared to the Au electrodes and bare Si substrate (Fig. 3.1(b)). Refer to Appendix B for the *P. pastoris* cell culturing procedure.

Microelectrode Chips

The microelectrode chips used to fabricate the nanoparticle necklace network array devices consists of a silicon wafer with a 500 nm thick thermal oxide layer. Lithography patterning was utilized to produce 300 nm thick Au electrodes onto the SiO_2 layer with a 50 nm thick titanium adhesion layer and electrode gap spacings of 10 and 20 μm.

3.2 NETWORK ARRAY DEVICE FABRICATION

A network array device is fabricated by electrostatically adsorbing the necklace network array solution onto a microelectrode chip. Characterization of the devices by FESEM, confirms that array morphology is a quasi-1D array, where 1D chains of 10 nm Au particles form a 2D monolayer (Fig. 3.3(a)) with reasonable uniformity after an ~24 hour deposition time. The network array forms long-range percolating channels traversing up to 100 μm in length and ~5 mm in width, where array length corresponds to electrode gap spacing. The 60 nm particles do not appear to have any particular correlation with the

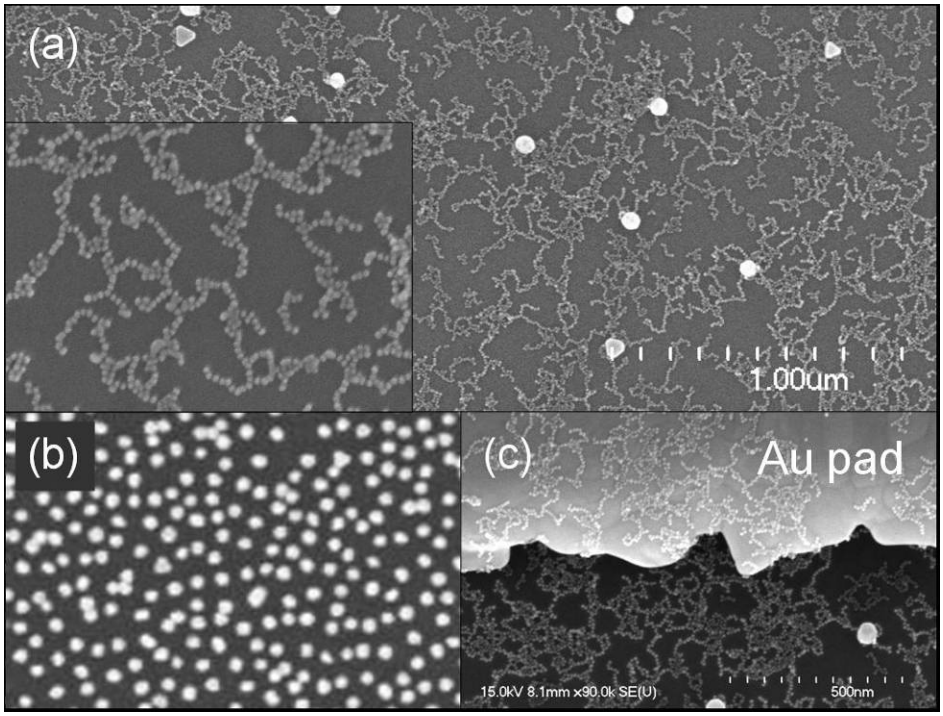

Figure 3.3 Field emission scanning electron microscope (FESEM) images of the nanoparticle necklace network array on a SiO_2/Si chip. (a) Nanoparticle network array on a chip after ~24 hour deposition . (b) Unmodified 10 nm Au particles after a ~48 hr deposition time form a nonpercolating submonolayer on the chip. c) The network array deposited well on the Au pad electrodes, leading to a naturally robust interconnection with the array. (Inset a) Higher magnification image of the nanoparticle necklace arrary. The scale bar in inset a and panel b is 100 nm.

necklace structure (Fig. 3.3(a)). In contrast, the 48 hour deposition of unmodified, citrate-functionalized 10 nm Au particles results in a sparse and nonpercolating submonolayer due to charge repulsion between particles (Fig. 3.3(b)). Electrostatic repulsion is beneficial to the fabrication of the network array, where a highly exfoliated network forms due to charge repulsion between individual necklace segments. Additionally, the network array shows excellent contact with the Au pads (Fig. 3.3(c)), illustrating a naturally robust interconnection with microelectronic circuitry.

Electrical characterization of the devices by I-V measurement shows room temperature conductivity. However, a significant number of devices exhibit Ohmic behavior due to a high amount of percolation pathways available along the large channel width of the array or a lack of necessary stored charge energy barriers (Fig. 3.4). Two techniques are implemented to transform Ohmic devices into non-Ohmic devices: micrometer scratching, to reduce channel width, and potassium ferric cyanide etching, to increase barricade density.

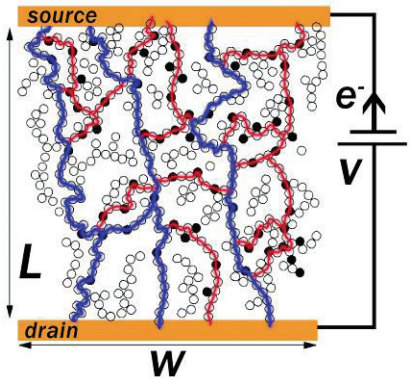

Figure 3.4. Device schematic of an L by W 2D array of nanoparticle necklaces. The percolation channels of a nanoparticle necklace network array between source and drain electrodes are shown. Dark circles are "quenched" single electron charges that act as barricades to the electron flow due to external bias, V. Channels containing a lower linear density of barricades (blue) will percolate at a lower bias than the paths with a larger number of charged particles (red).

Micrometer Scratching

A micrometer with a 10 μm diameter scanning tunneling microscopy (STM) tip is used to selectively remove a portion of the array by scratching. Through implementation of the micrometer scratching technique, a study of the relationship between electrical behavior and array width is performed. The array initially shows nonlinear I-V behavior at room temperature with V_T = -1.4 V and ζ ~2.3 (Fig. 3.5, scratching 0) and has dimensions of 30 μm by ~2,100 μm. Successive array scratchings are performed, with each scratching cycle reducing the width of the array by ~100 μm, leading to a gradual reduction in conductivity. At scratching 20, the array has dimensions of 30 μm by 100 μm and shows

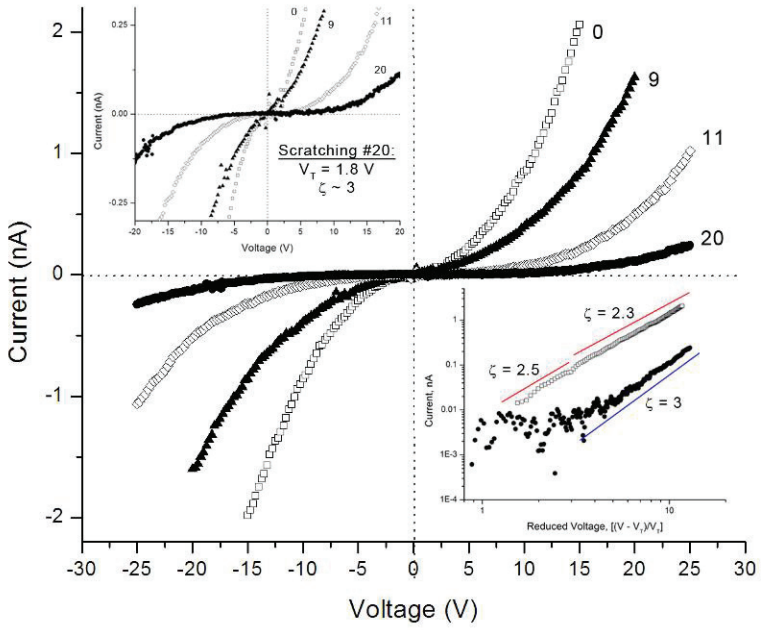

Figure 3.5. Micrometer scratching to form non-Ohmic devices. Initially (scratching 0) a 30 μm gap array shows non-linear I-V behavior at room temperature, but with a V_T =- 1.4 V. By scratching 20, the array exhibits a room temperature V_T = 1.8 V. Top inset, a magnified view of the low bias range of the I-V curve, illustrating the presence of a large V_T for scratching 20. Inset bottom, at scratching 0 ζ ~ 2.3 and at scratching 20 ζ ~3.

room temperature Coulomb blockade (Fig. 3.5, top inset). An analysis of the raw I-V data with a non-linear curve fitting function (see Appendix A) finds that at scratching 20 the device has a $V_T \sim 1.8$ V and a $\zeta \sim 3$ (Fig. 3.5, bottom inset).

V_T is linearly related to array width (Fig. 3.6). As array width is reduced from ~2,100 μm to ~100 μm, the V_T increases linearly from $V_T = -1.4$ V to 1.8 V. This V_T behavior is due to the reduction of percolating pathways by scratching. Initially (at scratching 0, Fig. 3.5), there were a large number of percolating pathways, where electrons traversing the array could easily avoid quenched charge barricades, resulting in no V_T at room temperature. As array width is reduced, fewer pathways are available and quenched charges become more difficult to maneuver around, thus, higher V_T values are exhibited.

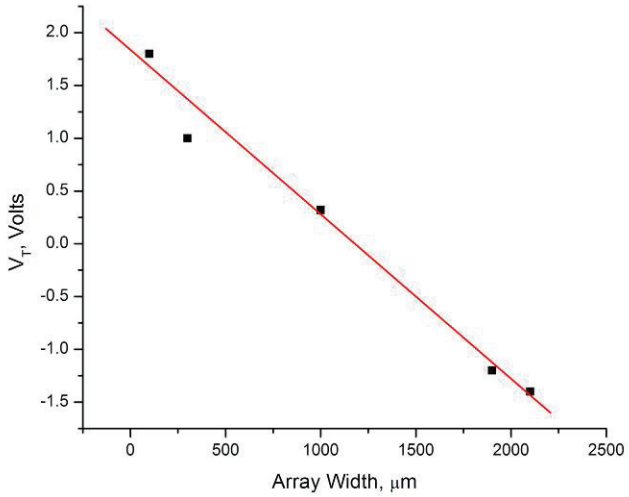

Figure 3.6. V_T versus array width. For the 30 μm gap device, as array width decreases from ~2,100 μm to ~100 μm, V_T linearly increases from -1.4 V to 1.8 V.

Potassium Ferric Cyanide Au Etching

Ohmic devices are treated with a 1.23 x 10^{-4} M solution of potassium ferric cyanide [$K_3Fe(CN)_6$] in water for several minutes, followed by thorough water washing. Cyanide ions uniformly etch Au nanoparticles though oxidative dissolution.[121] Based on the phenomena that cyanide ions dissolve Au nanoparticles, a highly sensitive sensor for the detection of cyanide was developed.[122] The $K_3Fe(CN)_6$ partially dissolves the outer diameter of the Au particles, increasing interparticle distance, i.e., increasing tunneling distance. With larger tunneling distances, more barricades are produced within the array, allowing higher V_T values to be achieved. To illustrate the technique, $K_3Fe(CN)_6$ dissolution is performed on an 50 μm array device with linear (i.e., $\zeta \sim 1$) I-V behavior at room temperature (Fig. 3.7). A 20 min exposure to $K_3Fe(CN)_6$ results in the I-V behavior

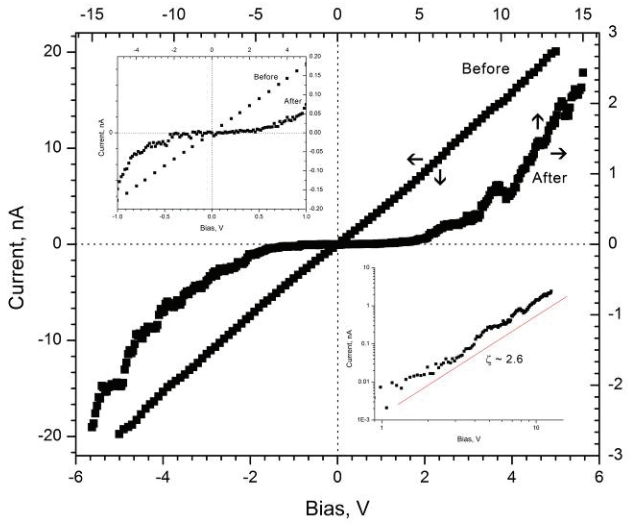

Figure 3.7. $K_3Fe(CN)_6$ etching to form non-Ohmic devices. $K_3Fe(CN)_6$ etching of the outer diameter of the Au nanoparticles making up the network array changes the I-V behavior of the device from Ohmic ($\zeta \sim 1$), to highly non-linear with a room temperature V_T = 1.1 V (upper inset). This change occurs as a result of increased interparticle distances caused by the partial dissolution of the Au particles. Inset: The $K_3Fe(CN)_6$ modified device exhibits a $\zeta = 2.6$.

of the device becoming highly non-linear and displaying Coulomb blockade (Fig. 3.7). Non-linear regression analysis of the I-V data by a curve fitting method (see Appendix A) determines that the $K_3Fe(CN)_6$ modified device has a $V_T \sim 1.1$ V and a $\zeta \sim 2.16$ at room temperature.

3.3 ELECTRICAL CHARACTERIZATION OF NETWORK ARRAY

Network array devices exhibit robust non-linear I-V behavior at room temperature that is highly reproducible. To illustrate robustness, a bias cycle is applied 30 times to a 10 μm gap device (Fig. 3.8). The I-V curves have excellent symmetry with respect to the application of forward and reverse bias, lack hysteresis and display only a minimal decrease in V_T following the 30 bias cycles (Fig. 3.8 inset).

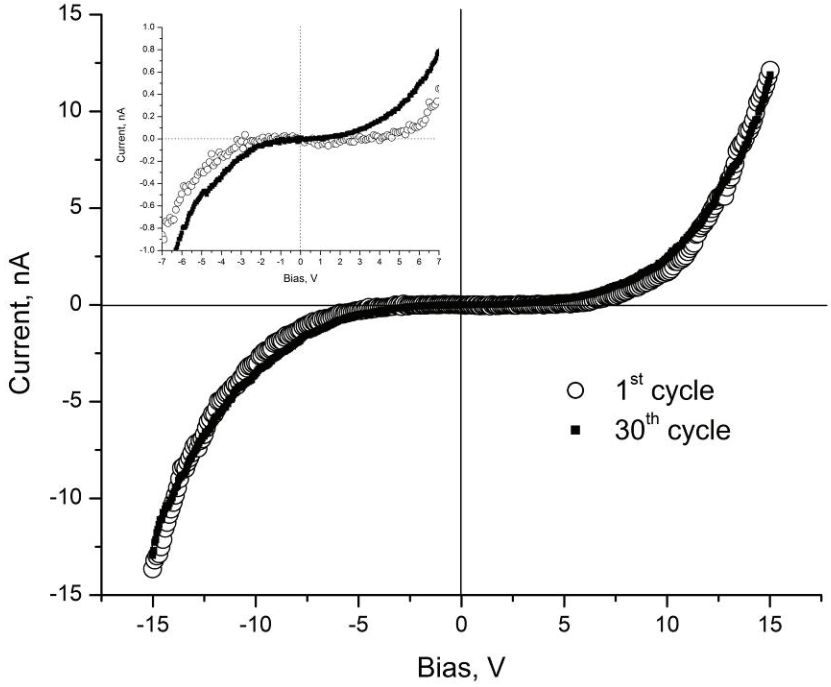

Figure 3.8. Robustness of the network array device. The I-V curve exhibits excellent symmetry with respect to forward and reverse bias without the presence of hysteresis. The cycle is defined as a change in bias from 0 to 15, 15 to -15, and -15 to 0 V. Inset: After 30 cycles, there was a slight reduction in V_T (upper inset).

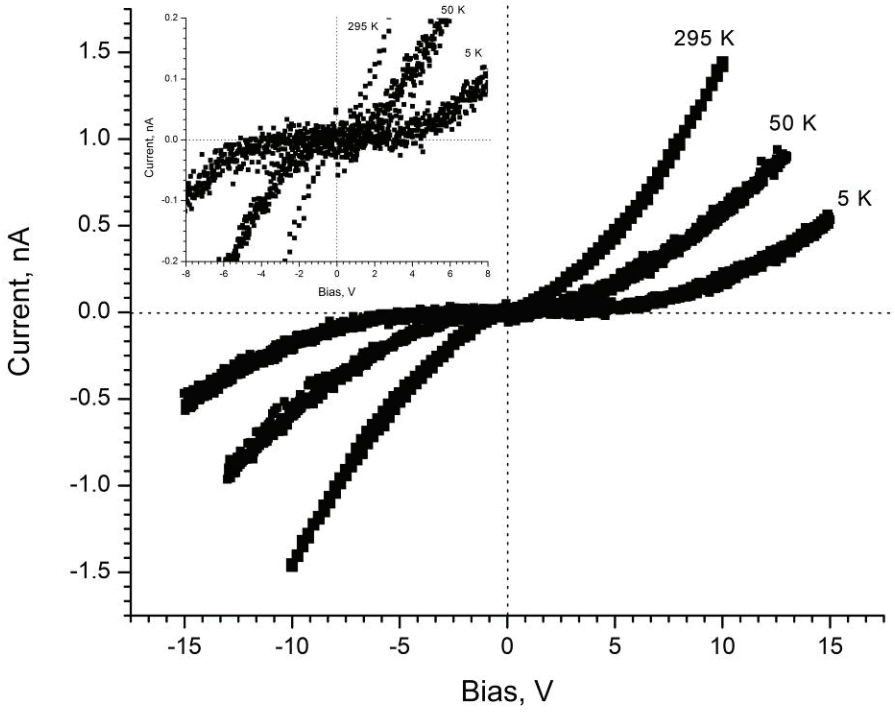

Figure 3.9. I-V characteristics for the 20 μm gap. A voltage cycle is applied to a 20 μm network array device at three temperatures. The voltage cycle is defined as 0 to positive bias, back to 0 V, 0 to negative bias, and back to 0 V. In forward and reverse bias, the I-V curves are symmetric and lack of hysteresis. Inset: A magnified view of the low bias region, highlighting the appearance of a large V_T = 3.1 V at 5 K.

The I-V behavior of a network array deposited across 20 μm spaced electrodes exhibits no hysteresis over several cycles and is highly symmetric at room temperature (Fig. 3.9). As temperature is reduced, the current decreases, leading to a positive bias V_T for the device. This behavior is consistent with experimental[8,41,54] and theoretical[46] studies of 2D array devices. The I-V behavior of the array device at bias $V > V_T$ is analogous to a second order phase transition given by $I \sim (V\text{-}V_T/V_T)^{\zeta}$, where ζ is the critical exponent.[7] Analytically, the ζ for 1D and 2D arrays is predicted to be 1 and 5/3, respectively.[7] The array device exhibits a universal value of $\zeta \sim 5/3$ for the entire temperature range of

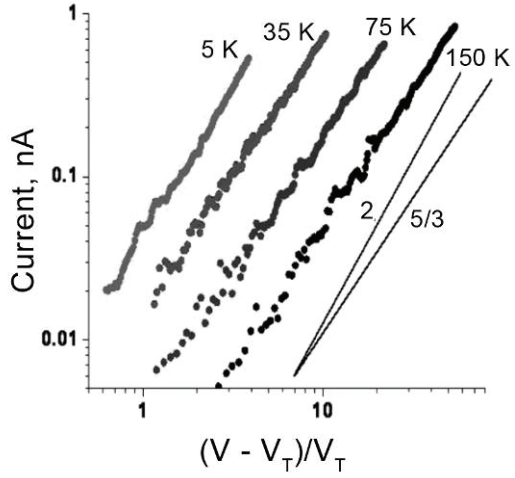

Figure 3.10. Current versus reduced voltage. The raw data for the 20 μm device is replotted as reduced voltage [$(V - V_T)/V_T$] versus I at a series of temperatures. V_T was determined using a non-linear curve fitting method. A universal value of ~5/3 was found for each temperature. The lines with slopes of 2 and 5/3 are shown for comparison.

study, 5 to 295 K, (Fig. 3.10). V_T is determined by a non-linear curve fitting method (see Appendix A) before plotting current versus the reduced voltage, $(V-V_T)/V_T$, on a logarithmic axis to display ζ. I-V cycles are performed at each temperature one to three times to ensure the accuracy and stability of the device. Data at 15, 35, and 150 K is collected during cooling, with the remaining T curves collected during heating from 5 to 295 K. Interestingly, the ζ is constant over a very large range of $(V-V_T)/V_T$, indicating that the dimensionality of the percolation path remains invariant, indirect evidence of the quasi-1D nature of charge transport.

The central difference (and the novelty of the reported structure) compared to 2D nanoparticle arrays is in the behavior of V_T as a function of T. At low temperatures, the linear decrease in V_T with increasing temperature is similar to other 2D array studies;[8,41] however, a sharp change in slope occurs around 50 K (Fig. 3.11(a)). Above 50 K, similar

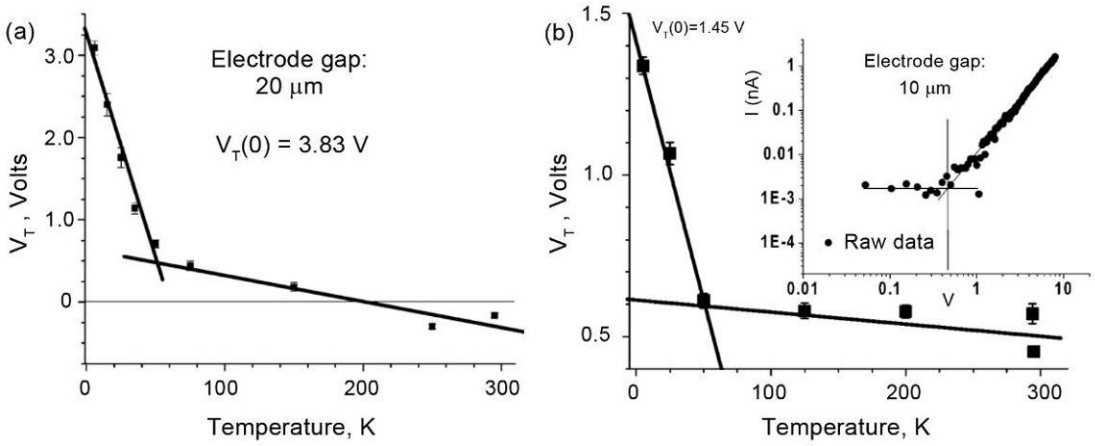

Figure 3.11. V_T versus temperature behavior. (a) The $V_T(T)$ relationship for the 20 μm device shows an abrupt change in slope at ~50 K with a $V_T(0)$ = 3.83 V. At T > 200 K, V_T becomes negative, indicating no room temperature switching behavior. (b) For the 10 μm device, the $V_T(T)$ relationship is also non-linear with a sharp change in slope at ~50 K. The significantly smaller slope at T > 50 K leads to a V_T of ~0.45 V at room temperature. Inset: Raw data at 295 K explicitly indicates the Coulomb blockade effect at room temperature.

to a single nanoparticle, the V_T becomes a weak function of T. As a result, for a 10 μm gap, high V_T of ~0.45 V at room temperature is obtained (Fig. 3.11(b)). The corresponding switching energy, eV_T, at room temperature is ~20 kT. This is an approximately 10-fold enhancement compared to a single particle blockade. The raw data explicitly exhibiting V_T at room temperature is shown in Figure A1.1 of Appendix A.

The sharp transition at 50 K for both gaps is attributed to the topology of the percolation path in the necklace network array. Field emission scanning electron microscope (FESEM) images (Fig. 3.3) indicate exfoliated necklace network morphology that is locally a 1D conductor with branching points several nanoparticles apart. Therefore, the coordination number for the necklace network is about 2, in contrast to a dense, randomly close-packed 2D array of 4 – 6. Simulation studies on dense 2D arrays show that as the bias rises from 0 to V_T, the array increasingly charges with single-electron charges

trapped in some of the individual nanoparticles that are randomly distributed over the array.[7,38] As the I-V current exhibits no hysteresis (Fig. 3.9), this random charge distribution is fixed, that is, quenched, as also observed for nanoparticle arrays.[8,37] In well-developed theory on 2D arrays of nanoparticles, random quenched charge distribution[7,38] presents barricades to the percolation path that are overcome as the bias gradually increases. Owing to a large coordination number in the dense 2D array, the percolation path is optimized to reduce the number of barricades (of energy height ~e/2C) in their trajectory.[7] As the temperature increases, some of these barricades are washed out because of the higher energy of the conduction electrons. This leads to a linear decrease in V_T such that at some $T \geq T^*$, there is at least one percolation path with no barricade connecting the two electrodes, resulting in no Coulomb blockade (i.e., $V_T \leq 0$).[8] Consistent with experimental observations, this model predicts a linear decay of V_T as T increases.[8] T* for a dense 2D array is below room temperature. In contrast, the 1D necklace network geometry constricts the percolation path due to a lower coordination number. Thus, the (fewer) barricades that still survive at high temperature in the percolation path cannot be circumvented due to the low coordination number of the array, hence a higher V_T is expected.

The barrier height of the barricade is the energy used to charge the isolated single particle (or cluster) with a single electron.[7,8] For a 10 nm particle surrounded by dielectric media of $\varepsilon \approx 4$, the capacitance is 2.22×10^{-18} F. The potential rise due to single-electron charging is $e/C \approx 72$ mV that presents an energy barrier of 72 meV. A doublet, that is, two particles in physical contact with a tunneling barrier well below kT, has a $C \approx 3.1$ x

10^{-18} F and an energy barrier of 51 meV. For a reasonable Coulomb blockade, or barricade, the barrier should be ~10 kT,[24] thus a doublet with a barrier energy of ~12 kT at 50 K presents a barricade to electron transport. Therefore, for T < 50 K, doublets and clusters larger than a doublet can also store charge to present a barricade. Because the barricade cannot be circumvented in the necklace network, due to a low coordination number, as T decreases beyond 50 K, the contribution from larger (individual) clusters increases, contributing to the rapid increase in V_T. However, for T > 50 K, the barricades will only be limited to single nanoparticles imbedded in the necklace segments. In other words, above 50 K, the 1D necklace segments in the percolation path are punctuated with nanoparticles with trapped single-electron charge that present a barricade to the electron flow (Fig. 3.4). The transition at 50 K is sharp because the barricade size abruptly rises from a single particle (the majority of barricades) to the contribution from the cluster of two particles.

The model is identical to the classical models for 2D arrays.[7,38,43] The only difference is that the conduction is through well-defined percolation paths made up of 1D necklace segments. As the bias ramps up, the current rises rapidly as barricades are overcome, leading to more possible network pathways for electron percolation. For example, in Figure 3.4 at low bias, only the "blue" pathway is "open" as it has the least amount of barricade; as the bias increases, the "red" pathways also become "open" leading to a rapid rise in current.

For the single isolated nanoparticle barricades at T > 50 K based on 2D array theory, the effective charging energy of the array is $\sim e V_T(0)/\alpha N$, where N is the length of the

conduction path in number of particles and α is a parameter that accounts for the quenched charge density stored in the array.[7,37,38] The α parameter for dense 2D arrays is experimentally measured to be ~0.25,[37] which agrees well with simulation calculations that predict α in the range of 0.23 to 0.36 depending on the lattice geometry of the array.[7,38,43] In the necklace network, for an electrode gap of 20 μm, N ≈ 2000 (at least), leading to $\alpha \approx eV_T(0)/[N(e^2/2C)] \approx 0.053$, where $V_T(0) \approx 0.65$ V (extrapolated from T > 50 K behavior to 0 K in Figure 3.11(a)). The over 5-fold smaller α for a necklace network compared to a dense lattice indicates an open structure with few trapped charge centers, or barricades, leading to (most importantly) a smaller T versus V_T slope above 50 K, as observed in Figure 3.11. A consequence of smaller slope at T > 50 K allows for the possibility of obtaining a robust Coulomb blockade effect at room temperature for the 10 μm gap (Fig. 3.11(b)).

3.4 ELECTRICAL CHARACTERIZATION OF THE BIOTRANSISTOR

The biotransistor is demonstrated by coupling live *P. pastoris* cells to a 10 μm network array device with an ~1 mm width (Fig. 3.12). A large array width is utilized in order to ensure adequate coverage of the array by the cells. However, this results in device currents that are higher than those observed in the prior studies of Figure 3.8 and 3.9 (Fig. 3.13(a)). The electrical behavior of the network array device is not significantly affected by cell deposition. Following cell coupling to the network array, the devices are exposed

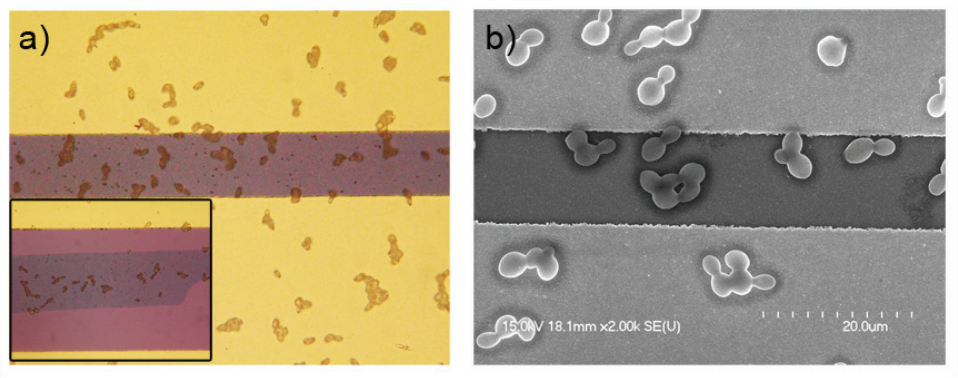

Figure 3.12. Characterization by microscopy. (a) An optical image of cells coupling to the network array on the SiO_2 surface and Au electrodes for a 20 μm device. The inset illustrates the preference of the cells to deposit on the network array, gap length is 50 μm. A large array is used to ensure adequate cell coverage. (b) SEM image of yeast cells on a network array between 20 μm spaced Au electrodes.

to methanol vapor while applying a ramp cycle. The live yeast cells metabolize the methanol vapor and produce formaldehyde.[123] At an appropriate potential along the bias ramp, the formaldehyde, which is deposited on the network array by the cells, oxidizes to form CO and H^+ through the following balanced chemical reaction:[124,125]

$$4HCHO + O_2 \leftrightarrow 4CO + 2H_2O + 4H^+ + 4e^- \qquad \text{Eqn. (1)}$$

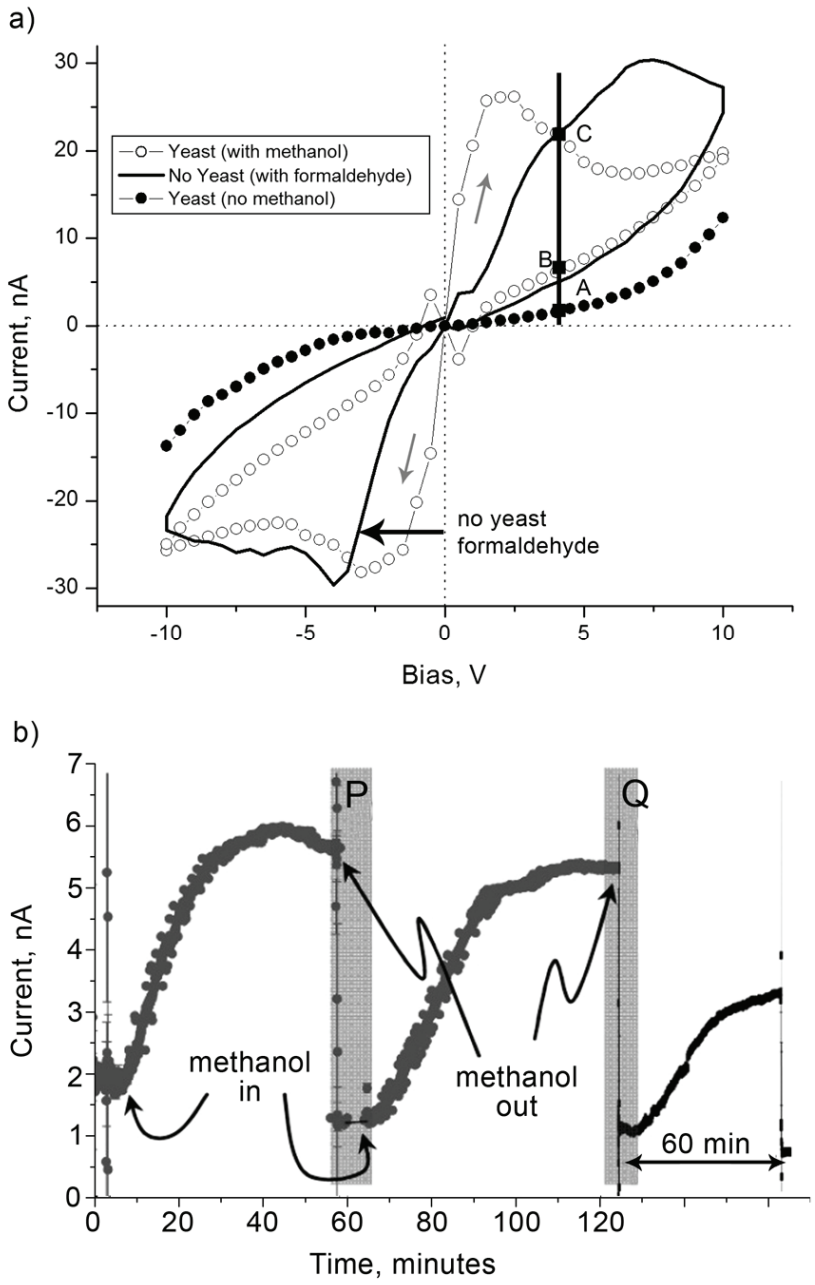

Figure 3.13. Biogating the network array device coupled with live cells. (a) The I-V behavior of the network array upon exposure to methanol. The device with yeast (open circles) exhibits redox peaks while the device with no yeast (filled circles) does not. A network array device with no yeast exposed to formaldehyde vapor (solid line) displays similar redox peaks. (b) The modulation of device current at a constant bias of 4 V as the yeast cells are exposed to methanol. At points P and Q, the methanol is removed.

The resulting I-V behavior of the network array-yeast system upon methanol exposure is analogous to cyclic voltametry.[126] For each molecule of formaldehyde oxidized, one electron is released to the network array (Fig. 3.14).[124,125] Current is maximized at ~2 V due to the diffusion limited oxidation current of formaldehyde. Upon lowering the bias from 10 to 0 V, no reduction current is observed at ~2 V as the gaseous product CO is no longer present in the system and can therefore not be reduced. Compared to the no yeast I-V curve, the current is elevated on the down bias ramp due to the modulation of the quenched charge distribution of the network array device by the electrons produced by formaldehyde oxidation. In other words, the electrons produced by formaldehyde oxidation redistributed the trapped charge barricades within the array and produced a percolation pathway with fewer barricades, thus allowing higher currents to be achieved. When a reverse bias is applied from 0 to -10 V, a peak at -3 V occurs when formaldehyde reduces back to methanol.[127] The redox peaks are not due to methanol reacting to the network array device. When a parallel study is conducted using a network array device

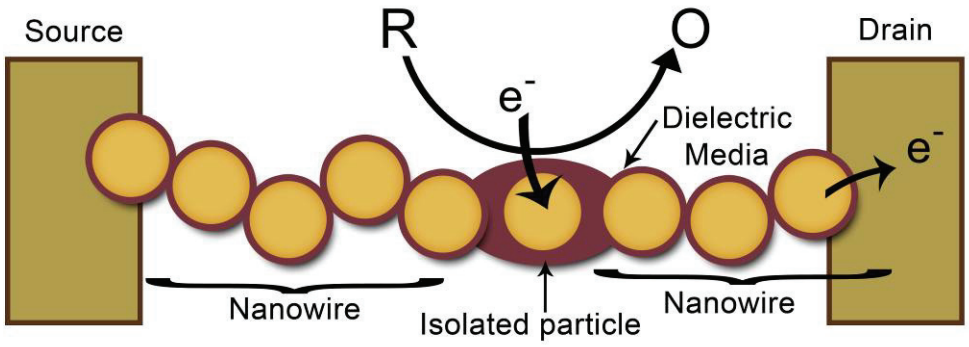

Figure 3.14. Electrochemical coupling to the nanoparticle necklace array. Formaldehyde gas (R) oxidizes to give an electron to the necklace array. The quenched charge distribution will change and lead to a modulation in I at fixed bias. At $V \sim V_T$, a large change in I occurs. Large ζ values correspond to higher changes in I.

without coupled yeast cells, the I-V behavior of the device does not exhibit redox peaks and appears similar to Figures 3.8 and 3.9 as seen in Figure 3.13(a).

It is important to note that there is no reference electrode in the system. Therefore, the redox peaks in the I-V curves do not correspond to documented thermodynamic electrochemical potentials and will vary from sample to sample, though reasonable comparisons can be made. For example, in a control experiment, formaldehyde vapor is exposed to a network array device with a 10 μm gap without coupled yeast cells. In

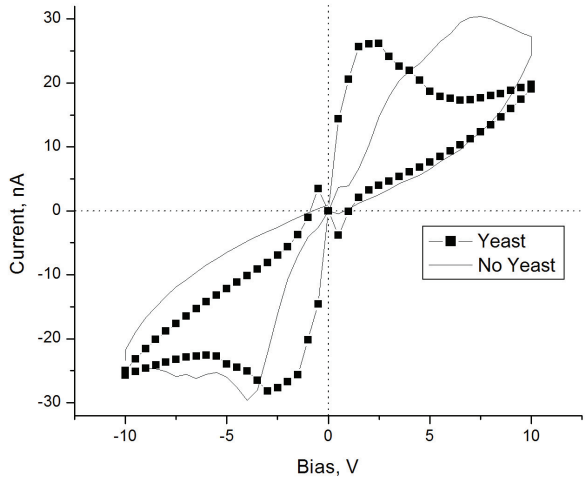

Figure 3.15. Formaldehyde exposure to bare network array. The effect of formaldehyde vapor exposure to the network array device without yeast exhibits redox peaks similar to a network array device that is coupled with yeast and exposed to methanol. Peak location and size differ due to the lack of reference electrodes and the difference in the physical nature of the formaldehyde.

forward bias, the I-V behavior of the network array device shows a peak with a shoulder positioned close to the bias observed for the maximum formaldehyde oxidation current of a network array device coupled with yeast cells (Fig. 3.13(a) and Fig. 3.15). Peak location and shape was similar in reverse bias as well. Although there are no reference electrodes and the physical nature of the formaldehyde in the two experiments differ, i.e., a chemical vapor versus the product of yeast metabolic reactions, the I-V behaviors can be reasonably compared to indicate that redox processes are responsible for the I-V behavior of the biotransistor during methanol exposure.

The biotransistor is biogated by the biochemical processes of live cells through exposure to methanol vapor. A demonstration of biogating is shown by applying a constant bias of 4 V while monitoring the current of the system as methanol is introduced and evacuated. A bias of 4 V is chosen because the potential is in the range of the expected maximum redox peak provided by Figure 3.13(b). During methanol exposure, the device exhibits an ~5-fold gain in current (points P and Q in Figure 3.13(b)). After a couple of cycles, the biotransistor is left at zero bias in a humid environment for ~12 hr. Upon subsequent methanol exposure, the device exhibits a lowered gain with a slowed rise time of 30 minutes compared to the ~20 minute rise time achieved ~12 hours earlier. The slowed rise time is due to the decreased metabolic kinetics of the cells. A control experiment is performed to rule out the possibility that methanol vapor is reacting to the network array device and not the live yeast cells. A 10 μm device without yeast is exposed to methanol at a constant bias of 4 V. In this case, a decrease, rather than an increase, is observed

(Fig. 3.16), excluding the simple reaction of methanol vapor to the bare device as the cause of the biogating behavior.

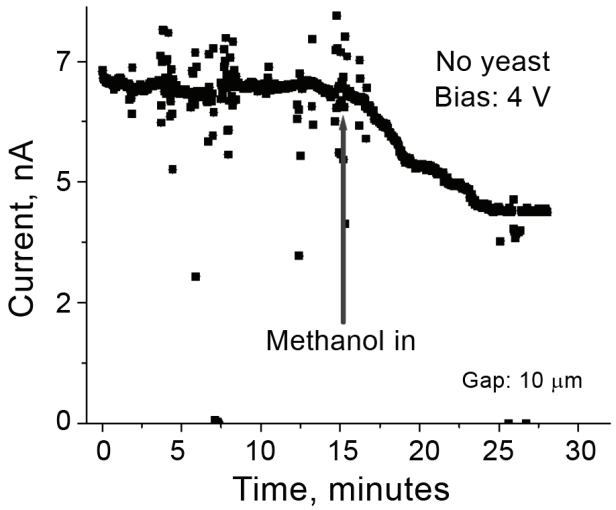

Figure 3.16. Methanol exposure to bare network array. At a constant bias of 4 V, a 10 μm device without yeast exhibits a reduction in current upon exposure to methanol vapor.

The ~5-fold gain in the current of the device at a fixed bias of 4 V is consistent with Figure 3.13(a), where point A is no methanol and point B is the gain due to methanol (points P and Q of Figure 3.13(b)). The biogating behavior of Figure 3.13(b) can be explained as follows. When the yeast cells are exposed to methanol, formaldehyde is produced and summarily oxidized. Electrons released during oxidation altered the quenched charge distribution of the network array. This alteration modulated the current of the device in a manner similar to physical gating by a third electrode. The

redistribution of the quenched charge distribution from points A to B caused biogating to occur. Unfortunately, point C was not attained while biogating due to an inhibition of the redox currents by diffusion (Fig. 3.13(a)).

3.5 SUMMARY AND CONCLUSIONS

The fabrication process and device applications of a 2D network of 1D nanoparticle necklaces has been described. Mediated by mobile ions on the nanoparticle surface, the particles self-assemble in solution to form long necklaces that can be directly deposited onto electrical circuitry. Two techniques are demonstrated to transform Ohmic network array devices into non-linear devices: (a) micrometer scratching to remove a portion of the percolating pathways and (b) $K_3Fe(CN)_6$ Au etching to partially dissolve the outer diameter of the Au particles to increase interparticle distances in order to form more barricades within the percolating pathways. The local 1D conductor nature of the array leads to fundamental differences in its behavior of V_T as a function of T. In previously reported studies on conducting 2D nanoparticle arrays, V_T decreases linearly with increasing temperature and vanishes at room temperature; however, for the network described herein, the slope abruptly flattens above 50 K. The insensitivity to T above 50 K makes it possible to achieve robust single-electron switching at room temperature in the array. The effect is attributed to barricades of single particles with single electron charge embedded in the 1D necklace segment above 50 K.

For the first time, biogating using the metabolism of a living cell coupled to a single electron device has been demonstrated. Methanotrophic *Pichia pastoris* yeast cells were coupled to an H^+ ion bridged nanoparticle necklace array device to form a biotransistor. Biogating was achieved by exposing the biotransistor to methanol, where the biochemical processes of the live cells utilized the methanol to produce formaldehyde, which was

oxidized on the array. Formaldehyde oxidation released electrons to the array that altered the quenched charge distribution, causing biogating to occur.

The response time of the device to chemical stimulation is consistent with the metabolism kinetics of the cell. Biogating, which allows the biochemical processes in the cell to be measured, will lead to applications in bioenergy, using the network array as the electrodes. Another potential application of the biotransistor is in high sensitivity biosensors, where the adsorption of biomolecules, viruses, microorganisms, or cells causes a change in the single electron quenched charge distribution. This results in a subtle modulation in the current of the device that can be measured in real time.

CHAPTER 4

POLYMER FIBER SHADOW MASK PATTERNING OF A NANOPARTICLE NECKLACE NETWORK EXHIBITING SINGLE-ELECTRON EFFECT AT ROOM TEMPERATURE

A continuing obstacle to nanodevice evolution is the facile interconnection of nanostructures to microelectronic circuitry. Among available device nanostructures, including carbon nanotubes,[100] nanowires,[104] graphene,[128] and metal (or semiconductor) nanoparticles,[11] an array of nanoparticles is the most promising nanodevice avenue, as arrays are naturally integrable with conventional circuitry. Additionally, the chemistry and diameter of the nanoparticles is easily tailored and highly versatile. Arrays of nanoparticles have been fabricated through drop or spincasting thiol-ligated Au nanoparticles,[8,42] electrostatic[47] and magnetic[73] forces, template assistance,[70,74] solvent-air interface assembly,[118,119] random deposition,[11] and scaffold utilization.[25,78,82,94] An advantage of using a scaffold is that site-specific arrays are formed predominantly through self-assembly techniques. A wide range of scaffold materials have been used to form one-dimensional (1D) nanoparticle arrays, including polyelectrolytes,[81] polysaccharides,[85] peptide microfibrils,[86] DNA,[78,80,83,84] and nanotubes.[79,82] The 1D nanoparticle arrays are fabricated by either mineralizing metal salt precursors directly onto the 1D scaffolds to form particles[78-81] or by self-assembling particles onto the scaffolds.[82,85,86] By using biopolymer scaffolds, quasi-one-dimensional (quasi-1D) nanoparticle network arrays were fabricated.[25,27] Two-dimensional (2D) nanoparticle

arrays have been self-assembled with live bacterium,[94] silver nanoplates,[129] and polyelectrolyte fiber scaffolds.[130]

In this report, a quasi-1D nanoparticle necklace network array is fabricated on a 2D poly(methyl methacrylate) (PMMA) film scaffold that is patterned using polyethyleneoxide (PEO) fiber shadow masking. Prior to network array fabrication, the nanoparticle necklaces are self-assembled in solution using ion mediation to induce an electric dipole.[48,51] Traditionally with shadow mask patterning, a metal mask with holes or lines is held close to or against a target to either deposit a material, as in the evaporation of metal,[131] or to remove a material, as in reactive ion etching.[132] Freestanding structures, such as nanowires,[54] nanofibers,[133] and nanoparticles,[132] have been increasingly utilized as shadow masks to achieve nanoscale device features. By using a freestanding V_2O_5 nanowire as a shadow mask, a conducting ~30 nm wide 2D array of Au nanoparticles was fabricated across electrodes.[54] A polymer nanofiber was recently used as a mask to form uniform 350 nm wide electrode gaps for the development of a submicron-channel organic field-effect transistor.[133] The benefits of using freestanding shadow mask structures are that precise etching/deposition occurs as the mask is in direct contact with the substrate and the structures can be easily removed using chemical[132] or mechanical[133] means. For example, the PEO fiber shadow masks used in this study are quickly removed by dissolution in water.

Conducting nanoparticle necklace network array devices are self-assembled onto the patterned PMMA film scaffolds. The devices exhibit single-electron behavior at room temperature, that is, a threshold bias, V_T, must be applied in order for current to flow

across the array. At bias, V, greater than the Coulomb blockade voltage, V_T, current, I, suddenly rises (turns ON) and flows according to $I \sim [(V - V_T)/ V_T]^{\zeta}$, with ζ as critical exponent.[7] Barrier energies for the Coulomb blockades are eV_T, where e is the charge of an electron. A single electron can overcome a blockade and turn the device ON, thus these systems are known as single-electron devices (SEDs).[24] A zero-dimension (0D) single nanoparticle SED requires cryogenic temperatures to operate, as a 10 nm diameter Au particle has an $eV_T < 100$ meV.[24] With 1D and 2D SEDs, the percolation path of the arrays contain many Coulomb blockades, which significantly increases device barrier energies. Despite an enhancement of V_T, experimental studies have found that due to V_T linearly decreasing with increasing temperature,[8,41] 1D, 2D, and dense quasi-1D array devices do not exhibit room temperature single-electron behavior.[8,37,41,47,50,70] However, room temperature switching is exhibited by quasi-1D nanoparticle necklace network SEDs,[48,51] as a result of V_T being nominally independent of temperature above 50 K for devices of this architecture.[48]

For 1D and 2D arrays, the analytically determined ζ values are 1 and 5/3, respectively. Experimentally, 2D arrays primarily exhibit $\zeta > 2$ and for 1D array $\zeta = 1.03 – 2.32$ at 4.2 K.[8,37,41,42,47,53,54] The nanoparticle necklace arrays on the PMMA scaffolds demonstrate $\zeta > 2$. A large ζ value corresponds to faster and sharper switching, as a smaller change in bias produces a greater change in current. The nanoparticle necklace network array devices are chemically etched with cyanide ions to reduce particle size and enlarge interparticle distances. Cyanide ions uniformly etch Au nanoparticles.[121] Particle etching results in an enhancement of V_T and ζ due to the development of more Coulomb

blockades within the percolation pathway. With robust, room temperature V_T and significant ζ values, the nanoparticle necklace network array devices are ideal for incorporation into chemical sensors and nanodevices requiring high sensitivity.

4.1 MATERIALS AND METHOD

Substrate Preparation

The microelectrode chip substrates consist of a silicon wafer with a 500 nm thick thermal oxide layer. A 50 nm thick titanium adhesion layer and 300 nm thick Au electrodes are lithographically patterned onto the silicon dioxide substrate with electrode gap spacings of 10 μm. Prior to scaffold deposition, the chips are cleaned using a piranha solution to remove hydrocarbon contaminants.

Formation of the Nanoparticle Necklace Network in Solution

The nanoparticle necklace network is made up of 10 nm diameter Au particles with a concentration of 5.7 x 10^{12} particles mL^{-1} at pH 6 (BBI International). The particles are stabilized with the capping agent tri-sodium citrate dihydrate ($Na_3C_6H_5O_7 \cdot 2H_2O$) to give them a negative charge. An electric dipole is induced in the particles by adding 120 μL of 10 mM HCl dropwise into 250 μL of the Au particle solution. The H^+ ions bind to the negative citrate ions on the surface of the Au particles and partially compensate the charge of the particles. When the particles are brought into proximity by thermal motion, an electric dipole is induced due to the high mobility of the bound H^+ ions.[51] Polarization of the particles causes them to align and "polymerize" into long 1D chains, or necklaces. During necklace formation the free electrons of the nanoparticles become delocalized, resulting in a red-shift in the surface plasmon resonance (SPR) absorption band of the solution.[90] UV-vis spectroscopy is used to monitor nanoparticle necklace formation in

real time through an analysis of the changing SPR band. In ~18 hrs, the nanoparticle solution color changes from wine-red to violet blue, where the blue color is indicative of necklace formation. The necklace network solution is stable for well over one week.

Scaffold Formation through Polymer Fiber Shadow Mask Patterning and Network Array Device Fabrication

A 1 wt% solution of poly(methyl methacrylate) (PMMA, MW = 75,000 Da) in toluene is spuncast onto a chip at 3,000 rpm for 20 s to produce a film ~35 nm thick. The PMMA film is annealed at 130ºC for 10 min. Polymer fibers made up of a 35 wt% solution of polyethyleneoxide (PEO, MW = 100,000 Da) in water are deposited across the electrode gaps on top of the PMMA film. Chips are exposed to oxygen plasma (98 W; 595 mTorr; 180 s) to remove the portion of the PMMA film not protected by the PEO fiber shadow masks. The samples are then immersed in deionized water for 30 min to dissolve the PEO fibers and the remaining PMMA film scaffolds are annealed at 130ºC for 1 hr. Network array devices are fabricated by exposing the PMMA scaffolds to ammonia plasma (70 W; 465 mTorr; 50 s) and depositing the Au nanoparticle necklace solution through electrostatic attraction for ~24 hrs.

Characterization Equipment

PEO fiber shadow masking is monitored using a Leitz Aristomet optical microscope. Network array deposition and morphology on the PMMA film scaffolds is studied with a Hitachi S-4700 Field-Emission Scanning Electron Microscope (FESEM). Electrical

property characterization (I-V behavior) is performed using a home-built system with an Agilent 3458A high sensitivity multimeter for measuring current and an Agilent 6613C to supply bias.

4.2 POLYETHYLENE OXIDE FIBER SHADOW MASKING TO FORM A PMMA FILM SCAFFOLD

Nanoparticle necklace network array devices are fabricated on polymer film scaffolds patterned using a polymer fiber shadow masking technique (Fig. 4.1). A 1 wt% solution of poly(methyl methacrylate) (PMMA) in toluene is spuncast onto a microelectrode chip at 3,000 rpm for 20 s to form a ~35 nm film. The sample is heated at 130ºC for 10 min to partially adhere the PMMA film to the substrate surface. A short baking time allows the excess PMMA, i.e., the portion of the film not forming the scaffold, to be removed later

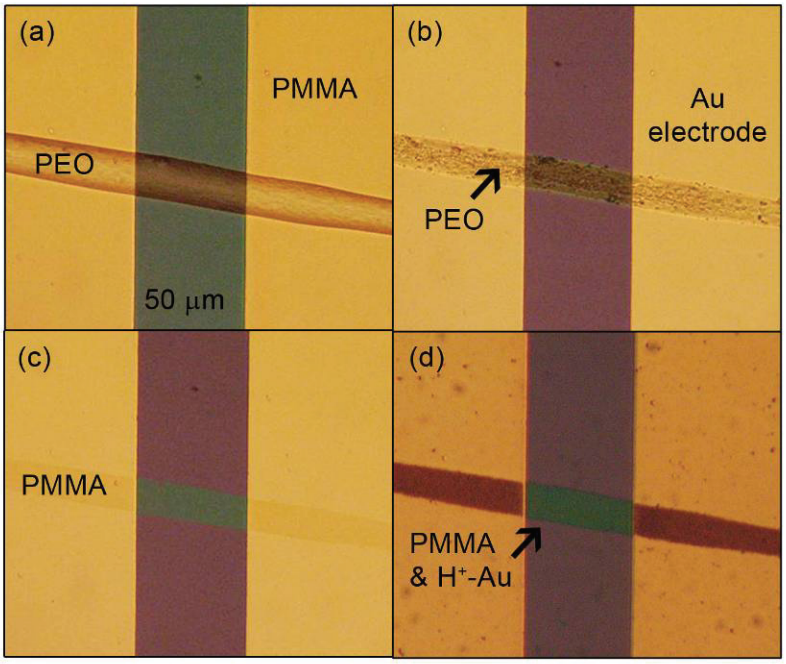

Figure 4.1. Images of PMMA film scaffold device formation. (a) A PEO fiber of ~18 μm diameter is deposited across a 50 μm electrode gap on a ~35 nm thick PMMA film. (b) Oxygen plasma exposure for 3 min removes the unprotected PMMA film. (c) The PEO fiber is dissolved in water, leaving a narrow PMMA film scaffold. (d) After exposure to ammonia plasma, the Au nanoparticle necklaces are electrostatically self-assembled onto the PMMA film scaffold. PMMA is absent on the edges of the Au electrodes.

in the fabrication process. Next, a 35 wt% polyethyleneoxide (PEO) solution in water is stretched into ~20 – 100 μm diameter fibers and placed onto the PMMA film across the electrode gap (Fig. 4.1(a)). The PMMA film unshielded by the PEO fiber is removed by exposing the sample to oxygen plasma for 3 min (Fig. 4.1(b)). After plasma treatment, the PEO fiber shadow mask is removed by immersing the sample in water for 30 min (Fig. 4.1(c)). The resulting patterned PMMA film scaffold is heated at 130ºC for 1 hr to adhere the film to the substrate surface.

The nanoparticle necklace network is deposited onto the patterned PMMA film by treating the sample with ammonia plasma to impart a positive charge on the scaffold. Through electrostatic attraction, the negatively charged nanoparticle necklaces deposit onto the amine functionalized PMMA scaffold in ~24 hr (Fig. 4.1(d)), as confirmed by Field-Emission Scanning Electron Microscopy (FESEM) (Fig. 4.2). Necklaces deposit as a quasi-1D array, where a 2D monolayer of exfoliated 1D necklaces with large voids spans across an electrode gap. Necklace deposition is confined to the PMMA film scaffold (Fig. 4.2(b)). The edges of the Au electrodes lack PMMA film, indirectly shown by the lack of necklace deposition at the edges of the electrode, as necklaces will only deposit onto the scaffold (Fig. 4.2(c)).

An interesting, and essential, feature of the patterned PMMA film is that during the scaffold fabrication process the film is absent on the Au electrodes near the gap. This feature is most clearly seen after nanoparticle necklace deposition (Fig. 4.1(d) and Fig. 4.2(c)). The lack of PMMA film at the edges of the Au electrodes is a result of inhomogeneties in film formation across the electrode gap during spincasting. No

PMMA film on the Au electrodes juxtaposed to the necklace network array device is advantageous to device conductivity, as the array spanning across the gap has excellent contact with the electrodes. Thus, more robust devices are fabricated.

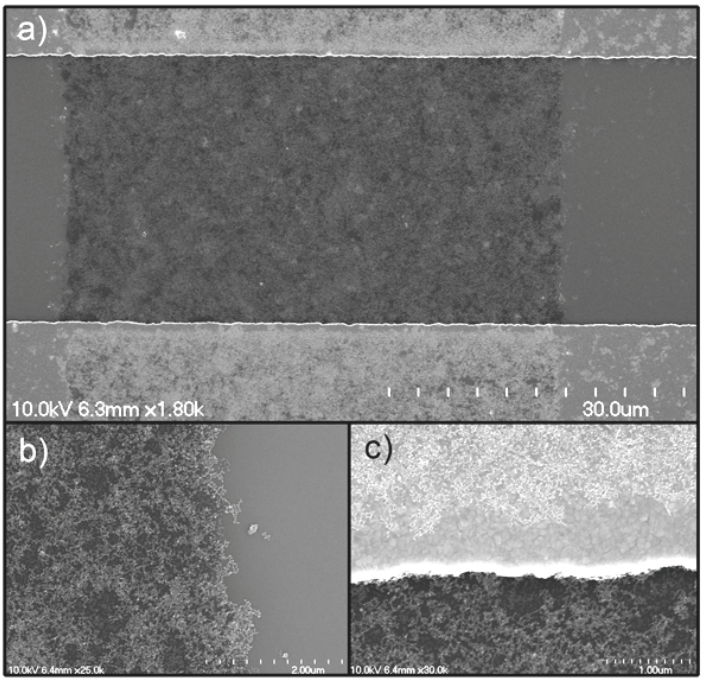

Figure 4.2. FESEM images of a nanoparticle network array device formed on a PMMA scaffold. (a) Necklaces self-assemble onto a 90 μm wide PMMA film scaffold across a 20 μm electrode gap (b) Array deposition is limited to the PMMA film scaffold. The nanoparticle necklace network array has a quasi-1D morphology. (c) The PMMA film is absent from the edge of the Au electrode.

4.3 ELECTRICAL CHARACTERIZATION OF NETWORK ARRAY DEVICES

The current-voltage (I-V) behavior of the conductive nanoparticle necklace network array device is non-linear at room temperature. A network array across a 10 μm electrode gap exhibits symmetric I-V behavior with no hysteresis (Fig. 4.3). Current, I, flows through the device after a threshold voltage, V_T, is surpassed. Once bias $V > V_T$, current flows according to the second-order phase transition $I \sim [(V- V_T)/ V_T]^{\zeta}$.[7] The critical exponent, ζ, is a measure of the gain of the device upon switching, i.e. $V > V_T$.[7] Larger ζ values correspond to faster and sharper gains, which lead to higher sensitivity switches. For 1D and 2D arrays, ζ is analytically determined to be 1 and 5/3, respectively. Although

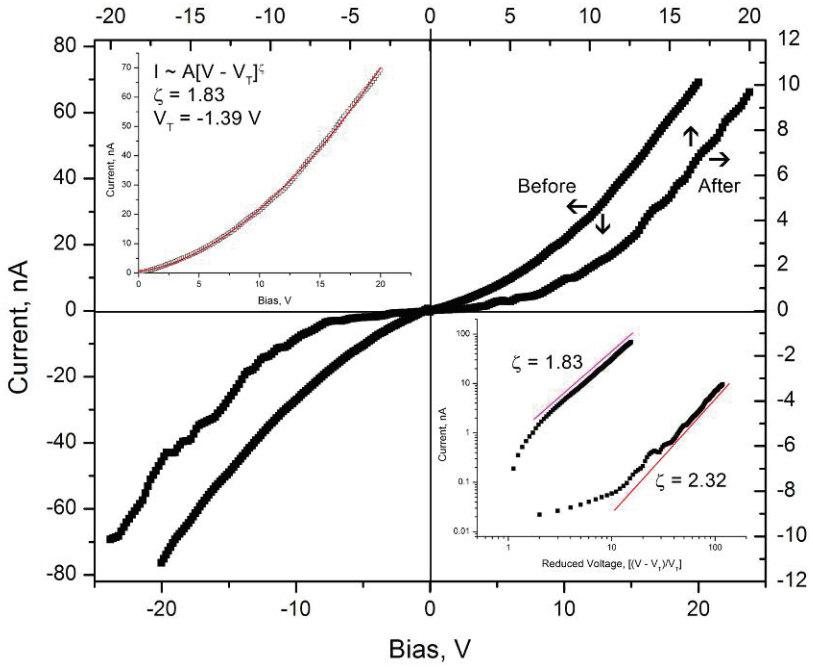

Figure 4.3. I-V behavior of a $K_3Fe(CN)_6$ etched nanoparticle network array device. A 10 μm device exhibited a V_T = -1.39 V ζ = 1.83 (lower inset) before $K_3Fe(CN)_6$ modification. After exposure to $K_3Fe(CN)_6$, the device shows non-linear I-V characteristics with a V_T = 0.16 V and a ζ = 2.32 (lower inset). The upper inset is the fitting function used to determine the V_T and ζ parameters of the before curve.

experimental studies of 2D array predominantly report $\zeta > 2$.[8,37,41,42,53,54] For the 10 μm device, a non-linear fitting function (Fig. 4.3 upper inset) determines that V_T = -1.39 V and ζ = 1.83 at 295 K.

The unique architecture of the nanoparticle necklace network array capitalizes on the leading electrical features of both 1D and 2D arrays. For example, experimental study has demonstrated that inclusion of voids within a close-packed 2D array increases ζ by increasing the tortuosity of the percolation path of electrons traversing the array.[42] With the nanoparticle necklace network array, the void content is exaggerated to the point where the array between the voids has a 1D necklace morphology. Another advantage of the quasi-1D nanoparticle necklace network array is an enhancement of V_T, leading to room temperature switching behavior. To illustrate, consider a single particle array with a $V_T \sim e/2C$, where $C = 2\pi\varepsilon\varepsilon_0 D$ is the capacitance of the particle, ε is the dielectric constant, ε_0 is the electric field permittivity in vacuum, and D is the diameter of the particle. For an array with a percolation path of N particles, the capacitance of the series is ~C/N, which leads to $V_T \sim \alpha e N/C$, i.e., an αN enhancement, where α is a parameter accounting for the level of quenched charge density stored in the array.[7,8,37,38] The quenched charges punctuate the array and can act as (temporary) blockades in the percolation path. Simulations have shown that the charges are stationary with increasing bias, leading to the name "quenched charge distribution."[7,8]

The α parameter is dependent upon array geometry. In a close-packed 2D array, experimental study has determined α to be ~0.25.[37] Theoretical predictions give a range of α values from 0.23 – 0.36, depending on the lattice geometry of the 2D array.[7,38,43] A

1D array is predicted to have an $\alpha \sim 0.50$.[7] The α value is higher for a 1D array compared to a 2D array as a result of array geometry. With a dense 2D array, optimal percolation paths around blockades are developed, reducing α. However, in a 1D array, every blockade must be overcome in order to surpass V_T and for current to flow, which leads to higher α values. For the nanoparticle necklace network, the 1D nature of the necklaces constricts the percolation path, forcing more blockades to be overcome and thus exhibiting higher α values compared to a dense 2D array. In summary, the quasi-1D morphology of the nanoparticle necklace network leads to increased ζ values, i.e. sharper switching, and enhanced V_T. The enhancement of V_T results in room temperature single-electron switching occurring in the nanoparticle necklace network array. Close-packed and moderately void-filled 2D arrays exhibit non-linear I-V behavior and V_T at cryogenic temperatures.[8,41]

Network array device electrical properties are improved by treating the samples with an etching solution to decrease Au particle size, thereby increasing interparticle distances. The etching solution is 0.124 mM potassium ferric cyanide ($K_3Fe(CN)_6$). Cyanide ions have been found to oxidatively dissolve Au colloids with a uniform shrinking behavior.[121] A highly sensitive sensor for the detection of cyanide was recently developed based on the phenomena that cyanide ions dissolve Au nanoparticles.[122] When the 10 μm device is exposed to $K_3Fe(CN)_6$ for 20 min, the I-V behavior significantly changes (Fig. 4.3). The V_T is enhanced from -1.39 V to 0.16 V and ζ increases from 1.83 to 2.32 (Fig. 4.3 lower inset). By using $K_3Fe(CN)_6$ to partially dissolve the Au nanoparticles making up the network array and enlarging interparticle distances, the

number of blockades within the percolation pathway increases. An increase in blockades enlarges the α parameter and the tortuosity of the percolation pathway, resulting in an enhancement of both V_T and ζ.

4.4 SUMMARY AND CONCLUSIONS

The process to pattern a PMMA film scaffold by PEO fiber shadow masking and the self-assembly of a nanoparticle necklace network array device onto the scaffold has been presented. The PEO fiber shadow masks allowed ~20 – 100 μm wide patterned PMMA films to be fabricated across electrode gaps. After removing the unshielded PMMA film with oxygen plasma, the PEO masks were easily removed by dissolution in water. By giving the scaffolds a positive charge through ammonia plasma exposure, the nanoparticle necklace network array device was formed with electrostatic attraction and self-assembly. Array deposition was confined to the patterned PMMA film scaffold.

The network array devices exhibited non-linear I-V behavior at room temperature. Both V_T and ζ were enhanced by treating the network array with a potassium ferric cyanide ($K_3Fe(CN)_6$) etching solution to partially dissolve the outer diameter of the Au nanoparticles making up the array. Etching enlarged the interparticle distances between the particles and increased the amount of blockades within the percolation path of the array. With more blockades present, ζ increased due to higher path tortuosity and V_T increased due to higher α parameter values, as α is related to the density of quenched charges, i.e., blockades, within the array. The versatile shadow mask patterning technique and robust room temperature single-electron switching, i.e., V_T, with $\zeta > 2$ make the nanoparticle necklace network arrays ideal for the development of high sensitivity nanodevices and sensors.

CHAPTER 5

A NANOPARTICLE NECKLACE NETWORK ARRAY SINGLE-ELECTRON DEVICE FABRICATED THROUGH INKLESS MICROCONTACT PRINTING

In a single-electron device made up of a single nanoparticle, current through the device can be modulated by altering the charge state of the particle by using a single electron.[24] With single-electron devices (SEDs), current switches ON, that is, suddenly increases, once the Coulomb blockade voltage, V_T, is surpassed.[24] In order to overcome the Coulomb blockade, the barrier energy, eV_T, where e is the charge of an electron, must be met. Single particle SEDs have been incorporated into transistors and logic devices.[11,12] However, given the small barrier energies for switching of the single particle devices, where $eV_T < 100$ meV for a 10 nm Au particle, cryogenic temperatures are required.[24] Room temperature Coulomb blockades with single particle SEDs are possible using a particle with a diameter < 1 nm;[25] but these devices are very noisy due to kinetic energy quantization from particle size variation and charge fluctuations.[26,27]

A two-dimensional (2D) array of nanoparticles enhances the V_T by over an order of magnitude by incorporating multiple Coulomb blockades in the percolation path of the array.[8,37,41,42] However, the V_T in 2D arrays vanishes at room temperature as a result of V_T linearly decreasing as T increases.[8,41] Recently, a quasi-1D array made up of a 2D network of 1D nanoparticle necklaces has been demonstrated to exhibit robust single-electron switching at room temperature.[48] The nanoparticle necklaces are self-assembled in solution by inducing an electric dipole through ion mediation.[48,51] Nanoparticle

necklaces have been shown to have enough sensitivity to be biogated with living cells by using the few electrons produced from the metabolic activity of the cells to modulate current through the array.[48] In this report, a network of nanoparticle necklaces is patterned onto a substrate through a variation of the microcontact printing (μCP) technique to form a chemical sensor with single-electron sensitivity at room temperature.

Microcontact printing (μCP) is a well-established method for generating micro- or nanoscale patterns on a substrate. In μCP, or soft lithography, the relief features of a patterned elastomeric stamp, typically made up of polydimethylsiloxane (PDMS), are "inked" with molecules and then brought into contact with a substrate. Ink is transferred to the substrate from the features of the stamp in contact with the substrate. The technique of μCP was developed during the early 1990's for the patterning of self-assembled monolayers (SAMs) onto Au substrates.[134,135] Currently, a wide range of fields, including biology,[136,137] electronics,[138,139] and tissue engineering,[137] employ μCP in their applications. However, a growing number of studies have reported in the last decade that a significant amount of low-molecular-weight PDMS oligomers transfer along with the ink during the μCP process.[140-145]

In the first detailed study on PDMS contamination through μCP, SAMs of dodecanethiol were printed with flat PDMS stamps onto Au substrates.[140] Substrate analysis by time-of-flight secondary ion mass spectrometry (TOF-SIMS) combined with principal components analysis (PCA) determined that PDMS contamination occurred with μCP despite an extensive week long stamp cleaning procedure performed prior to μCP. PDMS contamination levels were found to increase as the concentration of dodecanethiol

decreased.[141] Another study compared the μCP of flat to patterned PDMS stamps on substrates of Au, SiO_x, and TiO_2.[141] In the study, flat and patterned stamps transferred PDMS oligomers to the three substrate surfaces during μCP. The direct chemical interaction between PDMS and the two oxide substrates was stronger than the interaction between PDMS and the Au substrate. The study also determined that patterned stamps deposited more PDMS than flat stamps. A surprising result of the study was that when a patterned stamp was pretreated with UV/ozone and brought into contact with a Au substrate, more PDMS deposited in the non-contact regions of the Au substrate compared to the contact regions. The authors postulated that in the non-contact regions of the Au substrate, PDMS fragments left the sides walls of the stamp during μCP and were transported down to the areas of non-contact.[141]

While PDMS contamination during μCP is a deleterious side effect that can compromise the integrity of the printed sample, a new patterning technique called "inkless" microcontact printing (IμCP) emerged. With IμCP, the ink is the low-molecular weight PDMS oligomers that naturally transfer during the μCP procedure. The transferred PDMS oligomers change the surface energy of the substrate and enable patterning by dewetting to be performed. Surface energy patterning by IμCP has been used to form fluorescent polymer patterns on conducting poly(3,4-ethylenedioxythiophene) (PEDOT) substrates through spin- or dip-coating for applications in organic electronics and photonics.[142] Patterned organic semiconductor thin film transistors have also been fabricated using an IμCP surface energy modified substrate.[146] A biochip capable of differentiating the conformation states of biomolecules and the detection of enzymatic

biomolecular activity was developed through IμCP, using the transferred PDMS as a scaffold.[143] Another application of IμCP is as a mask for substrate etching. A study found that the 5 – 10 nm thick patterned PDMS layer formed by IμCP is remarkably sufficient to serve as a mask in the wet chemical etching (for Al, Mo, and ITO metal) and dry reactive ion etching (Si and polymer) of substrates.[145]

The non-commutative IμCP behavior of PDMS on the Au electrodes, i.e., PDMS transfers to the non-contact regions on the Au surface and only weakly interacts with the contact regions on the Au surface,[141] is advantageous to nanoparticle necklace network array device fabrication. The minimal deposition of PDMS on the Au electrodes juxtaposed to the PDMS scaffold on the silica allows the network array spanning across the electrode gap to have excellent contact with the Au electrodes. Interferometry testing of the Au electrode is used to directly confirm the negligible transfer of PDMS to the contact region, while Field-Emission Scanning Electron Spectroscopy (FESEM) characterization of the network array deposition behavior is used to indirectly substantiate that PDMS minimally transfers to the contact region of the Au electrode. If PDMS would transfer to the Au electrodes through direct PDMS stamping, the Au electrodes would be passivated and unable to form a conducting network array device.

The nanoparticle necklace network array device has a quasi-1D morphology on the IμCP scaffolds and exhibits single-electron behavior, i.e., V_T, at room temperature. The necklace architecture of the array allows room temperature switching to occur due to V_T being nominally independent of T above 50 K.[48] With robust V_T at room temperature, the network array device can function as a highly sensitive chemical sensor. For

demonstration, the necklace network array is chemically gated with methanol vapor, resulting in a modulation of the current through the network and a shift in V_T.

5.1 MATERIALS AND METHOD

Formation of the Nanoparticle Necklace Network in Solution

A network of nanoparticle necklaces is formed with 10 nm diameter Au particles at a concentration of 5.7 x 10^{12} particles mL^{-1} with pH 6 (BBI International). The capping agent, tri-sodium citrate dihydrate ($Na_3C_6H_5O_7 \cdot 2H_2O$), is used to electrostatically stabilize the particles by giving them a negative charge (Fig. 5.1(a)). Necklaces are formed by inducing an electric dipole in the particles by adding 120 µL of 10 mM HCL dropwise to 250 µL of the Au particle solution. Introduction of HCl causes a partial charge compensation of the particles due to the binding of H^+ ions to the negative citrate ions covering the Au surfaces (Fig. 5.1(b)).[51] Thermal motion brings the particles into

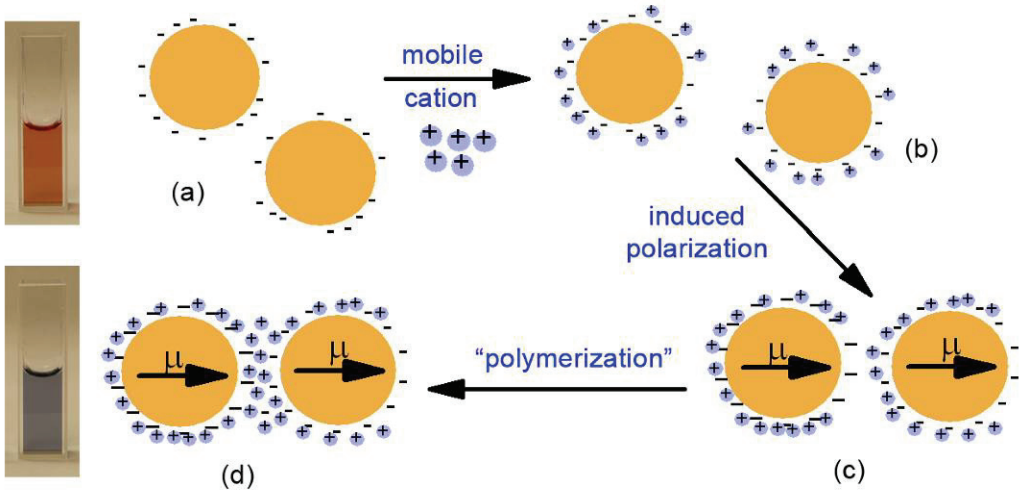

Figure 5.1. Polymerization of nanoparticles schematic. a) Unmodified 10 nm Au particles have a wine-red color and negative charge. b) H^+ ions from HCl partially charge compensate the Au particles. c) An induced electric dipole forms in the nanoparticles. d) The dipoles align and "polymerize" the particles into long chains. Necklace formation is indicated by the blue color of the solution.

proximity and induces an electric dipole. Alignment of the polarized nanoparticles "polymerizes" the particles into long 1D chains, or necklaces (Fig. 5.1(c)). As the necklaces form, a delocalization of the free electrons of the particles occurs and causes a red-shift in the surface plasmon resonance (SPR) absorption band of the solution.[90] Real time monitoring of necklace formation is conducted through UV-vis spectroscopy analysis of the SPR spectra of the necklace solution. The color of the nanoparticle solution changes from wine-red to violet blue in ~18 hrs (Fig. 5.1(d)). A blue solution color is indicative of the formation of the nanoparticle necklace network. The necklace solution is stable for well over one week.

Surface Preparation of Microelectrode Chips

The microelectrode chips are made up of a silicon wafer with a 500 nm thick thermal oxide layer. Lithography is used to pattern a 10 nm thick titanium adhesion layer and 50 nm thick Au electrodes on the chips with electrode gap spacings of 5 and 10 μm. The protective poly(methyl methacrylate) sacrificial layer covering the chips is removed by successive ultrasonic treatment with acetone, 2-propanol, and deionized water. Oxygen plasma exposure (98 Watts; 595 mTorr; 180 s) is used to remove hydrocarbon contaminants on the chips and make the chips hydrophilic. To study the effect of substrate pretreatment to IμCP behavior, chips are immersed into a solution of 100 μL hexanethiol in 10 mL ethanol for ~24 hrs to make the Au electrodes hydrophobic.

Inkless Microcontact Printing

The stamps for IμCP printing are fabricated with polydimethylsiloxane (PDMS) (Sylgard 184, Dow Corning) in a 10:1 ratio of PDMS to crosslinking agent. The PDMS mixture is poured into a 60 mm diameter petri dish containing a photolithography patterned mold. Molds for the fabrication of PDMS stamps are formed with the negative photoresist SU-8. The photoresist is diluted by mixing 500 μL SU-8 with 500 μL developer before a volume of 100 μL diluted SU-8 is pipetted onto a 1 inch diameter silicon wafer and spuncast at 3,000 rpm for 30 s. The wafer is heated at 65ºC for 30 s and then 120ºC for 1 min before it is placed onto a Hybralign Series 400 mask aligner. A mask with 10 μm wide lines spaced 90 μm apart is positioned above the wafer. The resist is exposed to UV light for 2 min and then cured at 120ºC for 1 min. As a negative photoresist, the SU-8 unprotected by the mask is cured, while the SU-8 protected by the mask remains soluble in developer and is removed by rinsing the wafer with developer for 2 min. Lastly, the wafer is rinsed with isopropyl alcohol and deionized water. The resulting mold consists of 80 μm wide lines (in contact during stamping) that are spaced 20 μm apart. Due to UV light undercutting of the mask, 90 μm wide lines are not achieved. The stamp is cured at 60ºC for 30 minutes. The cured stamp is placed onto a freshly oxygen plasmaed chip and heated at 60ºC for 1 hr to transfer low-molecular-weight PDMS oligomers from the stamp to the chip.

Nanoparticle Necklace Network Array Device Fabrication

After the stamp is removed, ammonia plasma (70 W; 465 mTorr; 50 s) is used to positively charge the printed PDMS scaffolds before an ~18 hr deposition of the Au nanoparticle necklaces. The nanoparticle necklaces deposit on the printed PDMS in 80 μm wide arrays on the silica across the electrode gaps.

Chemical Gating of a Network Array Device on a PDMS Scaffold

Network array devices are exposed to methanol vapor in a sealed chamber. During testing, devices are maintained at a constant bias while current is monitored as a function of time. The current of the device is modulated by the input/evacuation of the methanol vapor in the seal chamber. A pump supplies an input of air to evacuate the methanol from the chamber between chemical exposures. Output streams are vented to a chemical hood for safety.

Characterization Equipment

The UV-vis absorption spectra of the liquid solutions are measured using an Ocean Optics Model USB2000 spectrometer with a 1 cm quartz cuvette holder. IμCP onto the microelectrode chips is monitored with a Leitz Aristomet optical microscope with dark field capability. A Hitachi S-4700 Field-Emission Scanning Electron Microscope (FESEM) is used to characterize the morphology of the network array devices. Characterization of the electrical properties (I-V behavior) of the devices is performed

using a home-built system with a high sensitivity Agilent 3458A multimeter and an Agilent 6613C power supply. Differential interferometry measurements are performed using a home-built heterodyne interferometer with a red (633 nm) helium-neon laser split into a sample beam and reference beam.

5.2 INKLESS MICROCONTACT PRINTING

Inkless microcontact printing (IμCP) is used to pattern PDMS scaffolds onto a microelectrode chip for the fabrication of a network array device that exhibits room temperature single-electron behavior. With IμCP, the "ink" that is patterned onto the substrate is the low-molecular-weight PDMS oligomers that are transferred to the substrate during printing. The procedure for IμCP is depicted in Figure 5.2. The PDMS stamp consists of 80 μm wide lines spaced 20 μm apart. Before IμCP, the microelectrode chip is cleaned of hydrocarbon contaminants and made hydrophilic by exposure to oxygen plasma for 3 min. Oxygen plasma increases the strength of the bonds formed between the –OH groups on the PDMS stamp surface and the substrate by enlarging the

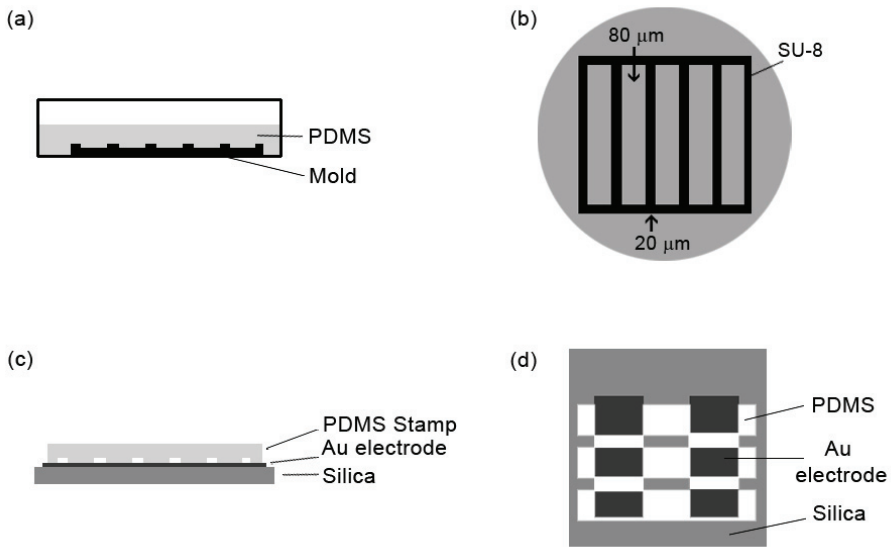

Figure 5.2. Schematic of inkless microcontact printing. (a) A solution of Sylgard 184 PDMS and crosslinking agent is poured into a petri dish containing a lithographically patterned mold. (b) The mold is formed with SU-8 photoresist and consists of 80 μm wide lines spaced 20 μm apart. (c) The cured stamp is put into contact with a chip at 60ºC for 1 hr, during which time PDMS is transferred to the chip. (d) When the stamp is removed, low-molecular-weight PDMS remains on the chip.

concentration of hydroxyl groups.[144,147] With stronger interfacial bonds, more PDMS is transferred, thus improving IμCP on the substrate.[144] The PDMS stamp is brought into contact with the chip for 1 hr at 60ºC at a relative humidity of ~40%. Following IμCP, 80 μm wide lines of PDMS have transferred to the silica substrate (Fig. 5.3). However, on the Au electrodes, PDMS has transferred predominantly onto the 20 μm wide non-contact regions (Fig. 5.3). Printing at room temperature for 12 hrs produces comparable IμCP results. A previous study showed that PDMS transferred to the non-contact regions of a Au surface and attributed the behavior to PDMS fragments escaping from the side walls of the stamp and transferring down into the non-contact region. Non-contact transfer of PDMS to silica was not exhibited.[141]

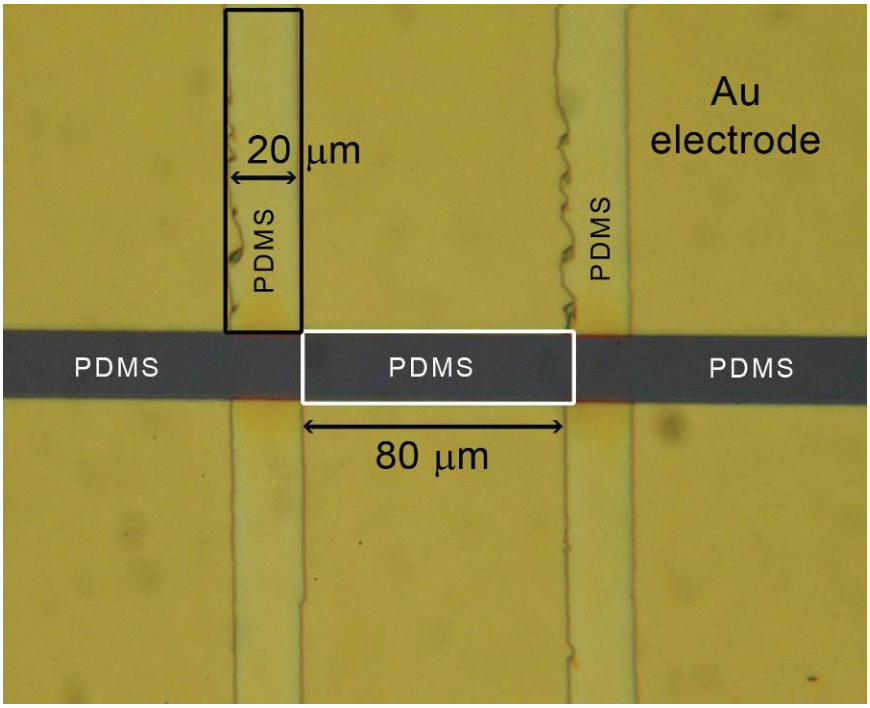

Figure 5.3. The non-commutative printing of PDMS. An optical image of a chip after PDMS stamping shows that PDMS is transferred to the contact region of the silica in 80 μm wide lines. However, on the Au electrodes, PDMS transfers to the 20 μm wide non-contact regions.

The transfer of low-molecular-weight PDMS oligomers in the contact regions of the Au electrode is negligible compared to the silica substrate. The non-commutative printing of PDMS is perhaps due to differences in adhesion between the PDMS stamp and the two substrate surfaces. Chemical interactions between PDMS and the substrates will affect their respective work of adhesion, W_a, and adhesion hysteresis, which is the change in adherence for approach versus retraction dynamics during printing.[148] A large adhesion hysteresis results from high interfacial bonding.[148] Chemical interactions between PDMS and the Au surface are weaker compared to PDMS and silica surface during IμCP.[141] With weaker chemical interactions, lower interfacial bonding and less PDMS transfer occurs on the Au surface.

A differential interferometer is used to confirm the minimal transfer of PDMS in the contact region of the Au electrode. With differential interferometry, two laser beams are applied to an electrode as an external AC field is used to polarize the Electrical Double Layer (EDL) at the interface of the electrode and an ionic solution. The EDL forms due to the electrostatic interaction between the ions in the solution and the surface of the electrode.[149] When applying the external AC field, ions modulate in the interfacial region of the electrode causing a modulation in the optical path length of the laser beams. If the electrode is partially passivated with a polymer film, such as PDMS or polystyrene, the charge modulation above the film will be minimal.[150] By positioning one laser beam ("reference") above the passivated film and the second beam ("sample") on the exposed bare electrode, the recombined differential signal of the charge modulation from the laser beams gives the amplitude of the ion accumulation at the electrode/solution interface.[150]

In this study, the reference and sample beams are positioned on the contact and non-contact regions of the Au electrode, respectively, to test for the presence of PDMS in the contact region of the electrode. The sample is contained within a 3-terminal electrochemistry cell (with working, counter, and reference electrodes) in a 50 mM NaCl solution. An external AC field and a bias ramp of -0.3 to 0.5 back to -0.3 V (red plot) is applied to the working electrode, i.e., the Au electrode (Fig. 5.4). The primary frequency (1f, blue plot) of Figure 5.4 is the recombined differential beam, showing a clear signal of the ion accumulation amplitude. The signal of the recombined beam for the contact (reference beam) and non-contact (sample beam) regions of the Au electrode is

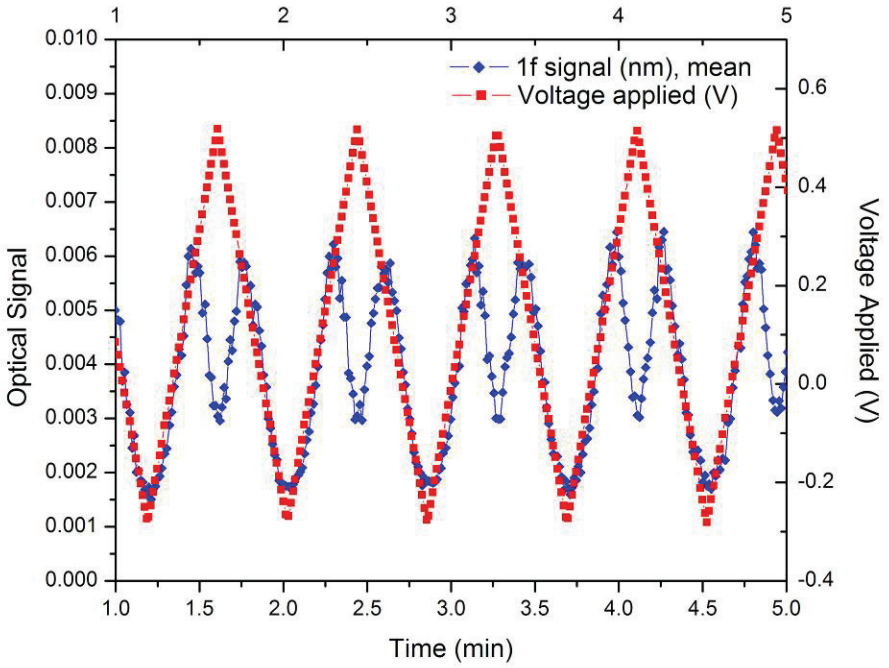

Figure 5.4. Differential interferometry testing of the Au electrodes. Using a differential interferometer, the transfer of PDMS to the Au electrodes is studied. A -0.3 to 0.5 back to -0.3 V bias cycle (red plot) and an external AC field is applied to the electrode. The primary frequency, recombined differential beam (blue plot), shows the amplitude of the ion accumulation occurring at the EDL of the electrode. The presence of a clear primary frequency signal indicates that a negligible amount of PDMS transfers to the contact region of the Au electrodes.

comparable to differential interferometry signals of a bare electrode (reference beam) and a passivating polystyrene film (sample beam).[150] Based on the clearness of the primary frequency signal, it is reasonable to state that the contact region of the Au electrode has an insufficient amount of PDMS to passivate the electrode, while the non-contact region has a PDMS thickness sufficient to passivate the electrode. In other words, a negligible amount of PDMS transfers to the contact region compared to the non-contact region of the Au electrode.

Relative humidity plays a critical role in the non-contact transfer of PDMS onto the Au electrode. When relative humidity levels during the IμCP process are ~10%, the non-contact PDMS transfer of the low-molecular-weight PDMS oligomers does not occur. At relative humidity levels above 35%, water absorbs onto the hydrophilic Au electrode surface, forming a water layer that can reach a thickness of 0.2 nm at a relative humidity of 65%, a height comparable to the dimensions of one water molecule.[151] As the level of relative humidity increases, the absorbed water layer becomes homogenous and thicker in height.[151] A possible explanation for the transfer of PDMS into the non-contact region of the Au electrode is that the PDMS fragments leaving the side walls of the patterned stamp[141] chemically interact with the mobile water layer on the electrode surface. Experiment has demonstrated that at interfacial boundaries siloxane materials have an affinity for water.[152] The affinity and low interfacial tension between PDMS and water is attributed to hydrogen bond interactions[153] and dipolar-dipolar interactions.[154] PDMS transfers to the non-contact region perhaps due to these interactions. When the relative humidity level is low, the absorbed water layer on the Au electrode is significantly

thinner.[148] As a result, PDMS fragments leaving the side walls of the stamp would not appreciably interact with the water layer and would not be mobile enough to transfer into the non-contact region. Differential interferometry testing confirms the lack of non-contact PDMS transfer on the Au electrodes at ~10% relative humidity.

5.3 FABRICATION OF NETWORK ARRAY DEVICES

Network array devices are fabricated with inkless microcontact printed PDMS scaffolds by exposing the chips to ammonia plasma to impart the scaffolds with a positive charge before immersion into the negatively charged nanoparticle necklace solution. By electrostatic attraction, a nanoparticle necklace network array deposits on the positively charged PDMS scaffolds in a quasi-1D morphology (Fig. 5.5). Necklaces deposit predominantly on the 80 μm wide PDMS scaffolds on the silica and the 20 μm wide non-contact region PDMS scaffolds on the Au electrodes (Fig. 5.5(d)). There is excellent contact between the network array devices and the Au electrodes (Fig. 5.5(c)). The

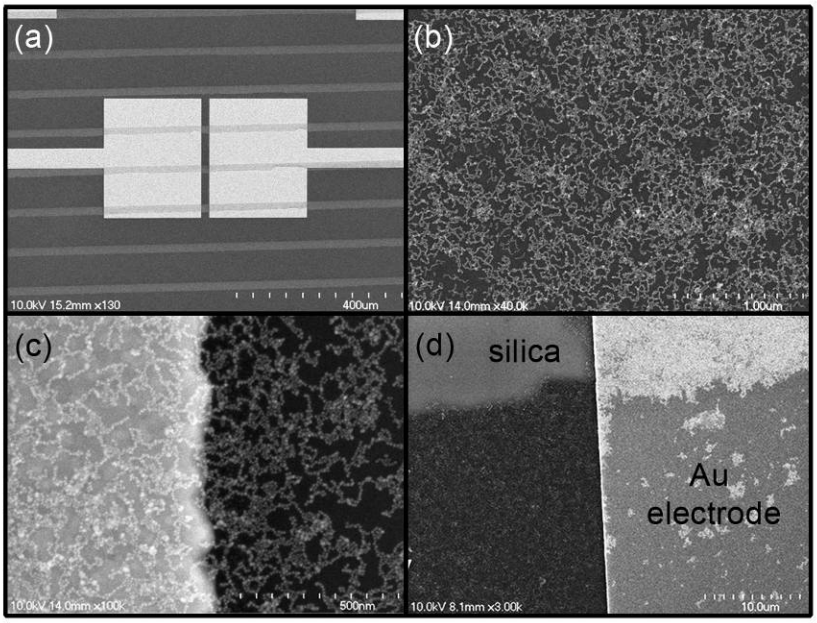

Figure 5.5. FESEM images of a network array device on a patterned PDMS scaffold. (a) Approximately three 80 μm wide arrays are formed for each electrode gap. (b) The nanoparticle necklaces deposit on the PDMS scaffold as a quasi-1D array. (c) There is excellent contact with the array and the Au electrodes. (d) On the Au electrodes, the nanoparticle necklaces deposit primarily on the 20 μm wide PDMS scaffolds (light colored region) and not on the 80 μm wide region that was in contact with the PDMS stamp.

FESEM images of the network array deposition are further evidence, though indirect, of the negligible transfer of PDMS to the contact regions of the Au electrodes.

The patterning of PDMS scaffolds by IμCP can be tailored by pretreatment of the microelectrode chips. By immersing the chip in a solution of hexanethiol for ~24 hours, non-contact printing of the silica surface can be achieved (Fig. 5.6). During IμCP at a relative humidity of ~10%, PDMS transfers along the edges of the stamp as lines, but also in the 20 μm wide non-contact region of the silica substrate. FESEM and optical images illustrate that necklace network array deposition is confined to the non-contact region of the silica (Fig. 5.6). The minimal deposition of nanoparticle necklaces elsewhere on the chip is indirect evidence that PDMS transfers predominantly in the non-contact region of the silica surface. To the best of the author's knowledge, this is the first observation of non-contact PDMS transfer on a silica surface by IμCP. A possible

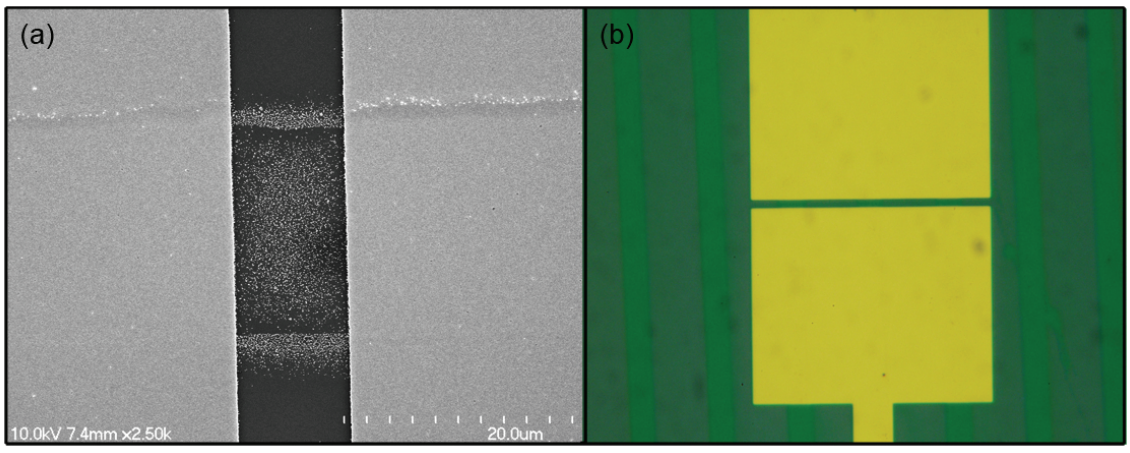

Figure 5.6. Non-contact IμCP on a silica substrate. (a) FESEM image showing deposition of the nanoparticle necklace array primarily onto the 20 μm wide PDMS scaffold in the non-contact region of the silica substrate. IμCP was performed at a relative humidity of ~10%. (b) An optical image of the network array device, where necklaces deposited as 20 μm wide arrays in the non-contact regions of the silica substrate (green lines).

explanation for the novel non-contact printing of PDMS on silica is that the hexanethiol treatment chemically interacted with the silica substrate by lowering the concentration of hydroxyl groups. With fewer hydroxyl groups on the silica, interfacial bonding in the contact region of the silica was reduced, thus lowering the amount of PDMS transferred. As with the non-contact transfer of PDMS onto the Au electrode, the lack of optimal chemical interaction between the PDMS and the silica surface at the contact interface led to an increase in non-contact PDMS transfer on the silica surface.

5.4 ELECTRICAL CHARACTERIZATION OF NETWORK ARRAY DEVICES

The nanoparticle necklace network array devices are electrically conductive with non-linear current-voltage (I-V) behavior at room temperature. An array spanning across a 10 μm electrode gap exhibits non-linear I-V behavior with minimal hysteresis (Fig. 5.7). The device possesses a threshold voltage, V_T, which must be surpassed before current, I, will flow. At bias $V > V_T$, current flows according to the second-order phase transition $I \sim [(V - V_T)/ V_T]^{\zeta}$, where ζ is the critical exponent.[7] For 1D and 2D arrays, the critical exponent is analytically determined to be 1 and 5/3, respectively.[7] The exponent ζ corresponds to the gain of the device upon switching, where larger ζ values mean faster and sharper responding devices. The 10 μm device has a V_T = -0.9 V and ζ = 2.1, as determined by a non-linear fitting function (Fig. 5.7). Minimal hysteresis of the I-V

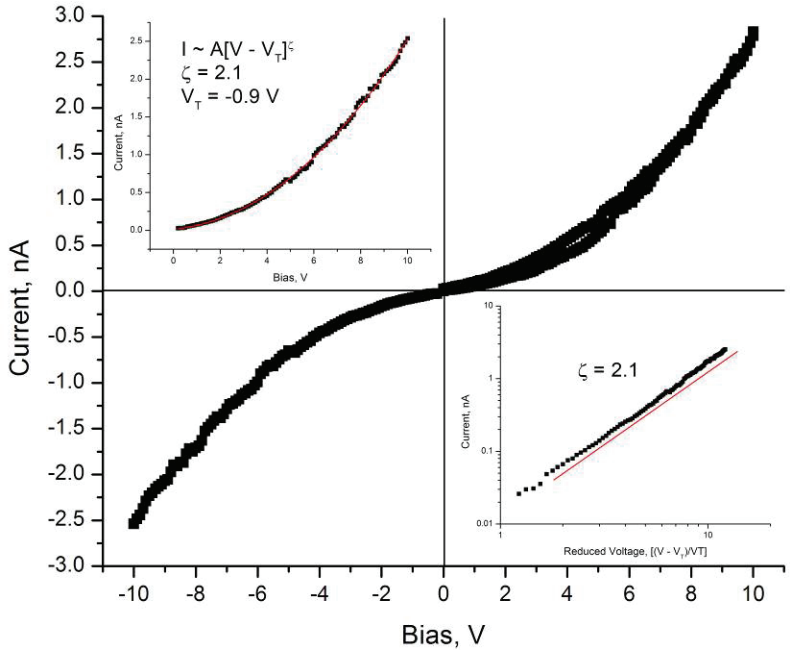

Figure 5.7. Electrical behavior of a 10 μm network array device. A 10 μm device exhibits V_T = -0.9 V and ζ = 2.1 (lower inset) at room temperature with minimal hysteresis. Upper inset: Fitting function to determine V_T and ζ values.

curves indicates that the device is robust upon bias cycling. Experimentally, ζ values >2 are predominantly demonstrated in dense 2D arrays.[8,37,41,42,53,54] For a 1D array of 30 nm diameter carbon nanoparticles, exponent values ranged from $\zeta = 1.03 – 2.32$ at 4.2 K.[47] Experimental[25,27,48-50] and analytical[52] studies of quasi-1D arrays report ζ values ranging from 1.2 ± 0.2 to 1.95. Previously reported nanoparticle necklace network arrays demonstrated $\zeta = 5/3$ values for temperatures, T, of 295 – 5 K.[48]

A network of nanoparticle necklaces is an amalgamation of 2D and 1D arrays. Essentially, the nanoparticle necklace network is a 2D array with an extremely exaggerated void content, where interconnecting 1D necklaces are arranged among the voids. Nanoparticle necklace networks are therefore quasi-1D in morphology. A fortuitous advantage of the necklace network architecture is that the tortuosity of the percolation path of the electrons traversing the array is increased by the large voids. Increasing tortuosity leads to larger ζ values[42] and improved device switching. For the 10 μm device, a $\zeta = 2.1$ indicates that the quasi-1D necklace of nanoparticles has a tortuosity comparable to a dense 2D array, but with room temperature switching behavior, i.e., V_T. Another effect of tortuosity maximization is that α, a parameter that accounts for the level of quenched charge density stored in the array, increases.[7] Quenched charges are stationary local trapped charges that can pose as (temporary) blockades in the percolation path.[7,8] For a single particle array (a zero-dimension array), the Coulomb blockade, $V_T \sim e/2C$, where $C = 2\pi\varepsilon\varepsilon_0 D$ is the capacitance of the particle, ε is the dielectric constant, ε_0 is the electric field permittivity in vacuum, and D is the diameter of the particle. In an array with a percolation path of N particles, the particles in series have a cumulative

capacitance of ~C/N, leading to $V_T \sim \alpha eN/C$, i.e., an αN enhancement.[7,8,37,38] The α of a dense 2D array is experimentally measured to be ~0.25,[37] which is in accordance with the predicted value range of 0.23 – 0.36, depending upon the lattice geometry of the array.[7,38,43] For 1D arrays, α is predicted to be ~0.50,[7] higher than 2D arrays as a result of the requirement that every tunneling barrier in a 1D array must be overcome in order for current to flow. Optimal percolation pathways around blockades are reached in 2D arrays due to the close-packed nature of the particles. Although 2D in design, given the quasi-1D morphology of the nanoparticle necklace network array, increased α values and thus, larger V_T are expected as compared to dense 2D arrays. Room temperature V_T in 2D arrays have not been demonstrated due to a linear reduction in V_T as temperature is increased.[8,41]

A nanoparticle network array device across a 5 μm gap exhibits a non-linear I-V curve with V_T = -1.1 V and ζ = 2.45 (Fig. 5.8). The behavior of the 5 μm device, i.e., ζ enhancing and V_T reducing compared to the 10 μm device, is predicted by experimental[41,42,71] and theoretical[71] array studies. In a void filled 2D array, ζ was shown to increase as device length was lowered, where 5 μm and 3.6 μm length devices exhibited ζ = 4.35 and ζ = 4.1, respectively.[42] The nearly 7-fold increase in device length resulted in a 0.25 change in ζ.[42] As the length of the gap is decreased, the tortuosity of the array is increased due to a reduction in available percolation pathways for the electrons to flow through. The increase in array tortuosity causes an enhancement of ζ for the 5 μm device (Fig. 5.8). In the nanoparticle necklace network array, a 2-fold increase in device length resulted in a 0.35 change in ζ. Thus, the morphology of the

nanoparticle necklace network array allows ζ values to be significantly modified through device dimension optimization. By reducing the length of the array, the α parameter reduces as less Coulomb blockades are included in the pathways, thus leading to a reduction in V_T.

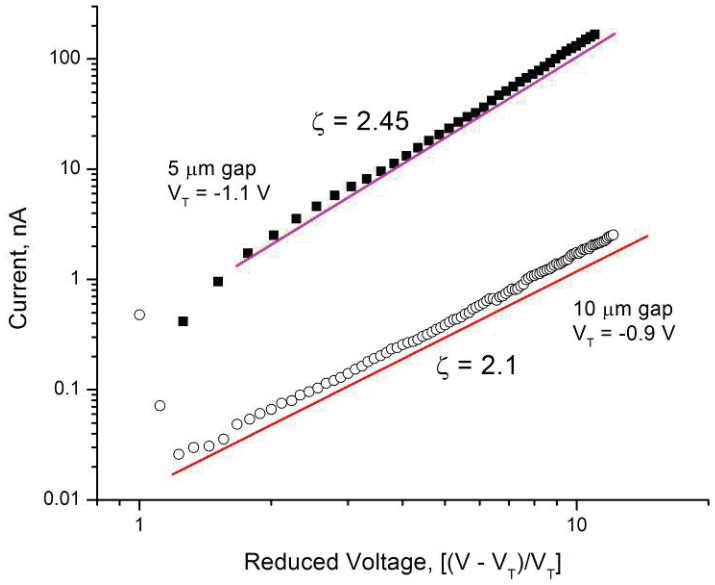

Figure 5.8. Effect of device length on the critical exponent. The 10 μm device has a ζ = 2.1 and V_T = -0.9 V. As device length is reduced, ζ increases and V_T decreases. The 5 μm device has higher currents with a ζ = 2.45 and V_T = -1.1 V. Both devices were measured at 295 K.

5.5 CHEMICAL GATING ELECTRICAL CHARACTERIZATION

Nanoparticle network array devices are chemically gated to show a modulation in I and V_T. The central principle of chemical gating is that when the network array device is stimulated by a chemical gas (or vapor), electrochemical reactions occur that redistribute the quenched charge distribution of the array and cause a modulation in the electrical properties of the device (Fig. 5.9). Chemical gating is conducted in a sealed chamber

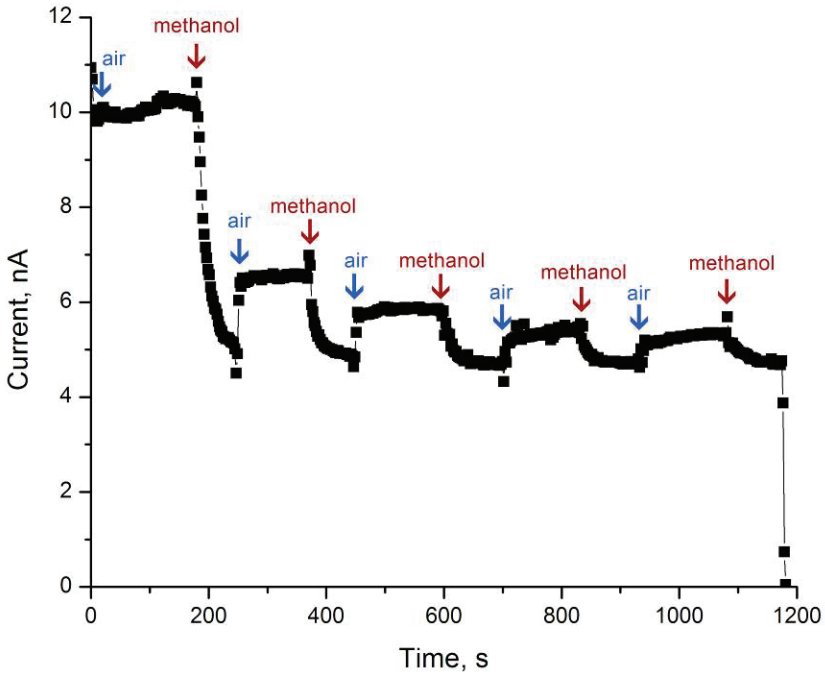

Figure 5.9. Chemical gating of a network array device with methanol. A constant bias of 4 V is applied to a 10 μm device. Initially in air, the device has I = 10 nA. Upon methanol exposure, current drops to I ~ 5 nA. Evacuation of methanol from the chamber with air results in a lessened equilibrium current value of the device with each successive methanol exposure cycle.

with external electrical interface connections (Fig. 5.10) by applying a constant bias across the device while monitoring current as a function of time. Compressed, filtered air is used in baseline current measurements and to evacuate gas testing molecules from the

device headspace. Gating is performed with methanol vapor by introducing the vapor to the device headspace through the input port of the chamber. In response, the current of the device modulates by increasing/decreasing. A flow of air is used to evacuate methanol from the device headspace through the output port.

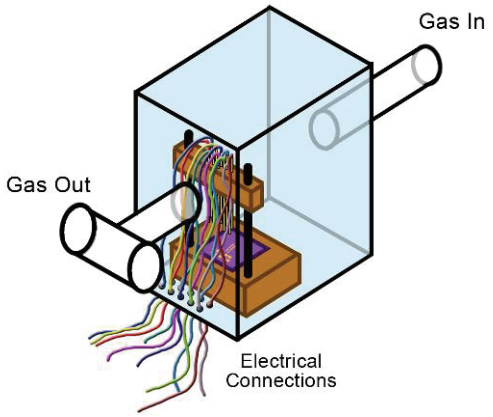

Figure 5.10. Schematic of the chemical gating chamber. The sealed chemical gating chamber has an input and output port that is vented to a chemical hood. Electrical connections are made through sealed holes in the base of the chamber.

Methanol chemical gating is performed on a 10 μm device exhibiting room temperature non-linear I-V behavior. Before gating, the I-V behavior of the device displays a V_T = -1.1 V and a $\zeta = 1.8$ (Fig. 5.11). During chemical gating, a constant bias of 4 V is applied to the device as methanol vapor is sequentially input and evacuated from the testing chamber while current is monitored (Fig. 5.9). Prior to the first methanol exposure, the device exhibits I = 10 nA at V = 4 V. Upon methanol exposure, the current drops to I ~ 5.1 nA. The current of the device does not increase to its former value following the evacuation of methanol from the chamber with air. Instead, a new equilibrium current of

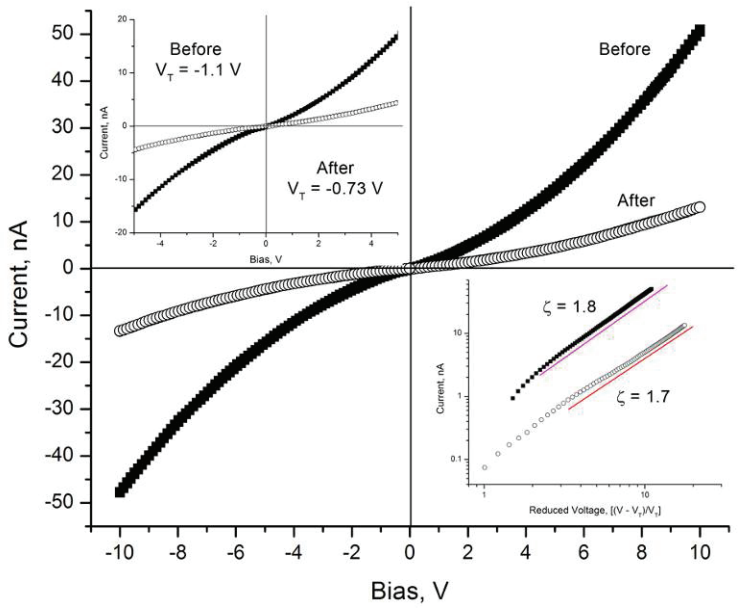

Figure 5.11. Electrical characterization of a 10 μm device before and after methanol gating. Before methanol exposure, the 10 μm device exhibits a V_T = -1.1 V and ζ = 1.8 (lower inset). After successive methanol exposures at a constant bias of 4 V, the device exhibits decreased current values with a V_T = -0.73 V and ζ = 1.7 (lower inset). A magnified view of the lower bias region is shown in the upper inset. All measurements were performed at 295 K.

I = 6.5 nA is established. A second exposure of methanol decreases the current to I ~ 4.8 nA again. After methanol evacuation, the new equilibrium current has lessened to I = 5.9 nA. Successive methanol exposures result in similar reductions in the equilibrium current of the device. Although testing is ended at 1,175 s (Fig. 5.9), it is reasonable to expect that the equilibrium current of the device will ultimately equal I ~ 4.8 nA, the current of the device during methanol exposure. After methanol chemical gating, the I-V behavior of the device in air exhibits decreased current values with a V_T = -0.73 V and ζ = 1.7 (Fig. 5.11). Gating by methanol caused the V_T of the device to shift from V_T = -1.1 V to -0.73 V. The enhancement of V_T signifies that methanol redistributed the quenched

charge distribution of the array so as to increase the number of Coulomb blockades encountered in the percolation path. The slight lowering in ζ from 1.8 to 1.7 is indicative of a lessening of the tortuosity of the percolation path. Branches within the pathway most likely became impassable, thus lowering ζ and the current through the device.

5.6 SUMMARY AND CONCLUSIONS

A technique to employ inkless microcontact printing (IμCP) to pattern nanoparticle necklace network array devices that exhibit room temperature single-electron behavior was presented. With inkless microcontact printing, the "ink" was the low-molecular-weight PDMS oligomers that naturally transferred during the printing process. During IμCP, PDMS was non-commutatively printed the microelectrode chip. PDMS transferred to the contact region of the silica substrate as 80 μm wide scaffolds, but on the Au electrodes, PDMS predominantly transferred to the non-contact region to form 20 μm wide scaffolds. Minimal PDMS transferred to the contact region of the Au substrate due to weaker chemical interactions as confirmed using differential interferometry.

Humidity played a crucial role in PDMS transfer to the non-contact regions of the Au electrode. At relative humidity levels above 35%, PDMS transferred to the non-contact region on the Au substrate. However, when relative humidity levels were ~10%, negligible PDMS transferred to the non-contact and contact regions of the Au electrode. PDMS transfer to the non-contact region was most likely caused by PDMS fragments escaping the side walls of the stamp and interacting with a thick water layer covering the Au electrode. The transfer of PDMS can be confined to the non-contact region of the silica by pretreating the chip with a hexanethiol solution. This report gives the first demonstration of non-contact IμCP onto silica.

The fabricated nanoparticle necklace array devices on the patterned PDMS scaffolds exhibited single-electron behavior at room temperature. Current flowed as $I \sim [(V - V_T)/$

$V_T]^{\zeta}$, where ζ is the critical exponent, at $V > V_T$. The quasi-1D network array devices displayed ζ values > 2.1 that were dependent on device length. A 5 μm device exhibited $\zeta = 2.45$ and a 10 μm device had a $\zeta = 2.1$. The enhancement in ζ with decreasing device length was a result of an increase in the tortuosity of the percolation path. The V_T of the arrays became higher as gap length increased due to a greater amount of Coulomb blockades present in the pathways. Chemical gating was performed on the devices using methanol vapor. The methanol redistributed the quenched charge distribution of the array, resulting in an enhancement of V_T. With robust room temperature single-electron behavior, the nanoparticle necklace network array devices have the potential to serve as highly sensitive chemical sensors and to be incorporated into nano- and bioelectronic devices.

CHAPTER 6

A NANOPARTICLE ARRAY SELF-ASSEMBLED ON AN ALIGNED NANOFIBER SHOWING ROOM TEMPERATURE SINGLE-ELECTRON SWITCHING

The use of nanostructures, such as carbon nanotubes (CNTs), nanowires, graphene, and metal or semiconducting nanoparticles, in electronic devices is ideal, as the structures serve as both the nanodevice and circuitry. By using CNTs, nanowires, and graphene, a range of devices has been developed, including logic circuits,[100,101] chemical[102,128] and biochemical[103] sensors, and live cell interfaces.[104,155] Nanodevices fabricated with a single nanoparticle have been shown to function as transistors and logic devices.[11,12] With nanoparticles, the chemistry and diameter of the structure is highly versatile and easily tailored. However, these zero-dimension (0D) single nanoparticle devices are difficult to fabricate and require liquid helium operating temperatures.[24] On the other hand, self-assembled nanoparticle arrays of one-dimensional (1D), quasi-one-dimensional (quasi-1D), and two-dimensional (2D) are naturally integrable with conventional circuitry and have been utilized in a number of nanodevices.[8,25,37,41,47,54,70] Devices with 1D architecture have been formed through random deposition,[11] electrostatic forces,[47] magnetic forces,[73] and template-assisted self-assembly.[70,74] Quasi-1D devices with e-beam lithography defined narrow Au nanoparticle arrays[50] and networks of 1D nanoparticle chains have been reported.[25,27,48,51] Array devices of 2D have been formed with self-assembly using thiol-ligation,[8,37,53] a live bacterium surface,[94] and a polymer fiber.[130]

Among nanoparticle array devices, of dimension 0D to 2D, a uniting feature is the presence of a Coulomb blockade voltage, V_T, where at bias, V, greater than V_T the current suddenly rises (turns ON).[24] Coulomb blockades have barrier energies of eV_T, where *e* is the charge of an electron. For these devices a single electron can overcome the Coulomb blockade and turn the device ON, as a result these systems are referred to as single-electron devices (SEDs).[24] Once the blockade is surpassed, i.e., at $V > V_T$, current, I, flows according to $I \sim [(V- V_T)/ V_T]^{\zeta}$, where ζ is the critical exponent.[7] For a 0D SED, the barrier energy, eV_T, is <100 meV for a 10 nm Au particle,[24] making cryogenic temperatures necessary.[24] Devices of 1D to 2D dimension contain many Coulomb blockades within the percolation path of the array, enhancing the V_T of the devices significantly. However, experimental studies of 1D, 2D, and close-packed quasi-1D array devices report that at room temperature the enhanced V_T vanishes,[8,37,41,47,50,70] as V_T decreases linearly with increasing temperature.[8,41] Room temperature single-electron switching, i.e., V_T, can be achieved by utilizing a quasi-1D array made up of a network of 1D nanoparticle chains.[25,27,48,51]

A promising avenue for the development of a quasi-1D nanoparticle array device with the potential for room temperature single-electron switching is through the use of a nanofiber template with nanoparticle self-assembly. Traditionally, nanofibers are formed by electrospinning, i.e., a high electric field is applied to a polymer solution to produce a nanometer sized jet that is stretched into long fibers and deposited onto a collector. Alignment of electrospun nanofibers across electrodes has been demonstrated by implementing a rolling drum collector[156] and electrostatic forces.[157] Electrospinning has

been used to form nanofiber composites consisting of metal (or semiconductor) nanoparticle decorated fibers. Composite fibers are formed by including metal salt precursors into the electrospinning solution and subsequently forming particles through chemical[158-160] and photocatalytic reduction[161-163] of the electrospun fibers. Also, metal particles can be directly incorporated into solutions prior to electrospinning[164,165] or self-assembled onto electrospun fibers[166] to form composite fibers. Although nanofiber electrospinning is a convenient method to deposit aligned templates across electrodes for the self-assembly of a nanoparticle array device, the electrical properties of these composite fibers has yet to be fully studied.

In this report, polyallylamine hydrochloride (PAH) nanofibers are electrospun across electrodes for the self-assembly of a quasi-1D Au nanoparticle array device. The positively charged amino ($-NH_2$) groups on the PAH polymer backbone allow negatively charged citrate capped 60 nm diameter Au particles to self-assemble onto the nanofibers. Additionally, ~10 nm Au particles are formed by using UV light of 260 – 270 nm and the amino groups of PAH to reduce Au^{3+} to Au^0 metal directly onto the nanofibers.[167] The self-assembly and nucleation processes are site specific, as the Au particles will deposit only onto the positively charged PAH fiber. Device conductivity is made robust by electroplating Au to the edges of the array in contact with the electrodes through the reduction of Au^{3+}.

The electrical behavior of nanoparticle array devices fabricated on PAH nanofibers is studied in this report. By tailoring the diameter of the PAH fibers, the morphology of the nanoparticle array can be optimized to form void-filled quasi-1D arrays. Due to the

nanoparticle necklace network type architecture of the array on the larger PAH fibers, room temperature single-electron switching occurs. The room temperature switching of the devices is attributed to the fact that for nanoparticle necklace networks, V_T becomes nominally independent of temperature above 50 K.[48] Given the robust V_T at room temperature, the nanoparticle arrays on the aligned PAH nanofibers have potential applications in highly sensitive sensors and nanoelectronics.

6.1 MATERIALS AND METHOD

Substrate Pretreatment

The microelectrode chip consists of a silicon wafer with a 500 nm thick thermal oxide layer. Lithography is used to pattern a 50 nm thick titanium adhesion layer and 300 nm thick Au electrodes with gap spacings of 10, 20, 30, 50, and 100 μm. Prior to electrospinning, the chips are cleaned with piranha and immersed into a solution of 10 mL ethanol and 100 μL octadecyltrichlorosilane (Gelest) for 1 hour then rinsed twice with ethanol to make the silica surface hydrophobic.

Electrospinning of Polyallylamine Hydrochloride Nanofibers

The electrospinning solution consists of ~3.0 g polyallylamine hydrochloride (PAH, MW = 75,000 Da), 4.0 mL water, and 1.0 mL ethanol. The solution is placed onto a roller for ~24 hours to become thoroughly mixed. Electrospun PAH nanofibers are deposited directly onto the microelectrode chip, which is mounted onto a grounded rolling drum in the electrospinning setup. A plastic 10 mL syringe is filled with 1 mL of the PAH solution and fitted with a needle. The syringe is placed horizontally into an automated syringe dispenser at a flow rate of 0.01 mL h^{-1}. A positive bias of 5.2 kV is applied to the needle of the syringe to form a cone and jet for the production of nanofibers. The generated PAH nanofibers travel 19 cm to the grounded rolling drum and onto the chips in an aligned morphology. Following electrospinning, the chips are exposed to ozone at a concentration of 10 g m^{-3} for 1 minute at 130ºC. The ozone generator is an OREC Ozone

Systems V Series instrument with compressed air as the oxygen source. An IN USA Ozone Analyzer Model H1 is used to measure the concentration of ozone. After ozone, the chips and fibers are annealed at 130ºC for 1 hour in air.

Fabrication of Network Array Devices on Nanofiber Scaffolds

Once the fibers are annealed, the chips are rinsed with deionized water and immersed in a 60 nm diameter Au colloid solution of concentration 2.6 x 10^{10} particles mL^{-1} and pH 8 (BBI International) for ~24 hours. Following 60 nm Au particle deposition, the chips are rinsed with deionized water and placed vertically into a 1 x 1 cm quartz cuvette filled with a 1.23 x 10^{-4} M solution of gold(III) trihydrate ($HAuCl_4 \cdot 3H_20$) in DNAse free water. The chips are exposed to UV light from a xenon lamp source at a wavelength of 260 - 270 nm for 20 min from a Thermo Oriel Instruments Model 66905 model light source with a Thermo Oriel 69911 power supply. The UV light causes the amine groups of the PAH to reduce the Au^{3+} in the $HAuCl_4$ solution to form ~10 nm sized Au particles onto the PAH nanofibers between the deposited 60 nm particles. The growth of Au through UV is also performed horizontally in a mounted electrochemistry cell with a silicon wafer mirror to reflect the UV light.

The robustness of the contact between the nanoparticles on the PAH fibers and the Au electrodes is improved by Au electroplation. For Au electroplation, chips are placed in a 3-terminal electrochemistry cell (working, counter, and reference electrode) with 0.01 M $HAuCl_4$. A Princeton Applied Research Potentiostat/Galvanostat Model 273A is used to apply a bias of 500 mV to the targeted Au electrode (working electrode) for ~1 minute.

During bias application, Au^{3+} from $HAuCl_4$ reduces onto the PAH/nanoparticle contact at the Au electrode interconnection.

Characterization Equipment

A Hitachi S-4700 Field-Emission Scanning Electron Microscope (FESEM) is used to characterize the morphology of the network array devices. Electrical characterization is performed using a home-built system with the high sensitivity multimeter Agilent 3458A and Agilent 6613C power supply.

6.2 ELECTROSPINNING OF POLYALLYLAMINE HYDROCHLORIDE NANOFIBERS

Nanofibers of the polymer polyallylamine hydrochloride (PAH) are electrospun directly onto a microelectrode chip to serve as a scaffold for the fabrication of a nanoparticle array device. The electrospinning setup (Fig. 6.1) consists of a horizontally mounted automated syringe pump, a rolling drum collector, and a power supply. A 10 mL plastic syringe with a needle is filled with a solution of ~38 wt% PAH in water and ethanol. Prior to electrospinning, the microelectrode chips are cleaned with piranha and immersed in a silane solution to make the silica hydrophobic. A hydrophobic surface results in devices that are cleaner and more uniform, as the negatively charged Au nanoparticles will deposit predominantly onto the positively charged PAH. The silanized chips are

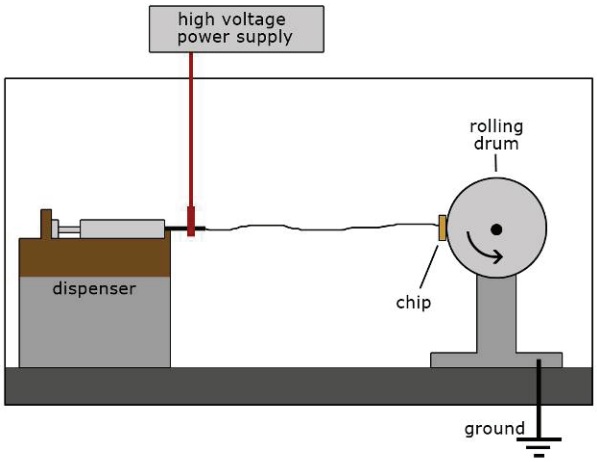

Figure 6.1. Schematic of the electrospinning setup. In the electrospinning setup, a syringe containing the PAH solution is mounted horizontally in an automated pump dispenser. The collector is a grounded rolling drum that is positioned ~19 cm from the syringe needle. An external electric field is generated by applying a high voltage to the needle of the syringe. Electrospinning is conducted in a sealed box.

affixed to a grounded rolling drum with double-sided tape so as to align the electrode gaps perpendicular to the rotation of the drum. The distance between the tip of the needle and the drum is ~19 cm. During electrospinning, the syringe pump dispenses solution at a flow rate of 0.01 mL hr^{-1} as a 5.2 kV bias is applied to the needle. During bias application, the polymer solution surface at the tip of the needle is pulled into a semi-sphere by electric forces and surface tension.[168] Charges move through the solution and concentrate at the tip of the semi-sphere. As more charges accumulate, the surface is pulled into a conical shape known as a Taylor cone. The charge per unit area continues to increase at the tip of the cone until ultimately a jet of solution pulls away from the tip towards the rolling drum collector. During the flight to the rolling drum collector, the external electric field accelerates and stretches the jet, causing a reduction in jet diameter. The jet is collected on the drum as PAH nanofibers. Rotation of the drum aligns and stretches the nanofibers into long 1D scaffolds perpendicular to the electrode gaps. Subsequent traveling fibers are repelled by the charged fibers that are deposited on the drum surface, resulting in a monolayer of PAH nanofibers on the chip surface.[168]

The diameters of the nanofibers are reduced by exposing the chip to ozone at a concentration of 10 g m^{-3} at 130ºC for 1 minute. In addition to reducing fiber diameter, the ozone treatment increases the surface roughness of the fibers, allowing for improved Au nanoparticle deposition later in the fabrication process. Following ozone treatment, the fibers are annealed for 1 hr at 130ºC in air. The resulting PAH nanofibers are aligned across the electrode gaps with diameters of ~60 – 200 nm.

6.3 FABRICATION OF NANOPARTICLE ARRAY DEVICES ON POLYALLYLAMINE HYDROCHLORIDE NANOFIBER SCAFFOLDS

A nanoparticle array device is fabricated by depositing 60 nm Au particles on the PAH nanofibers spanning across the electrode gaps. The negative citrate ions covering the Au particles bind to the positively charged amine groups of the PAH. After a ~18 hr deposition time, the 60 nm Au particles have deposited onto the nanofibers with large (i.e., non-percolating) interparticle distances (~120 nm) (Fig. 6.2). If electrospinning is performed using a PAH solution that is not fresh, i.e., at least 3 months old, the 60 nm Au particles deposit with an "edge-effect" (Fig. 6.3). Although interesting, devices exhibiting edge-effect deposition were not implemented in nanoparticle array device

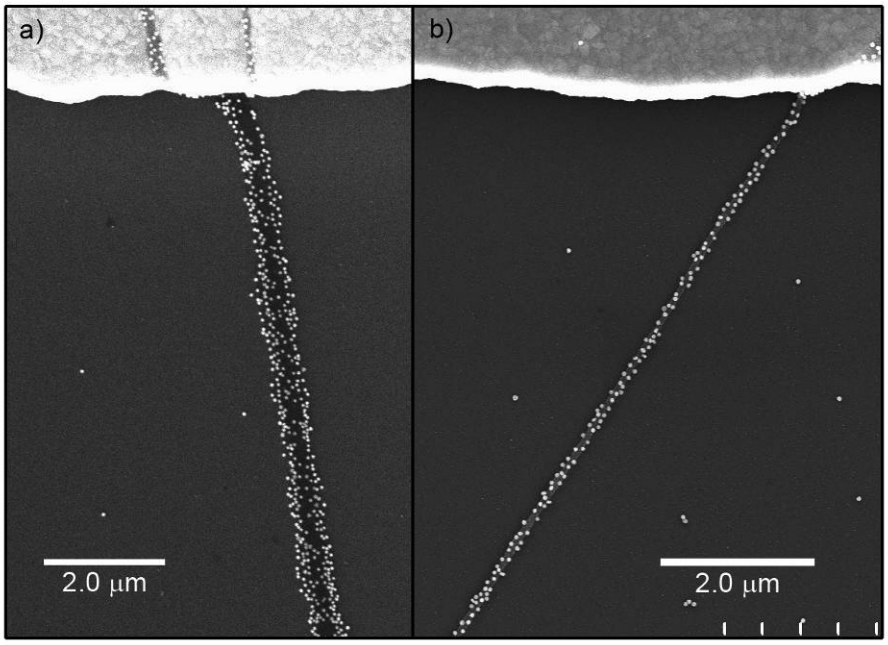

Figure 6.2. Deposition of 60 nm diameter Au particles. FESEM images of the self-assembly of 60 nm Au particles onto the electrospun PAH nanofibers. Interparticle distances between particles is ~120 nm.

characterization due to their 1D nature. The reason for this will become apparent later in the electrical behavior discussion.

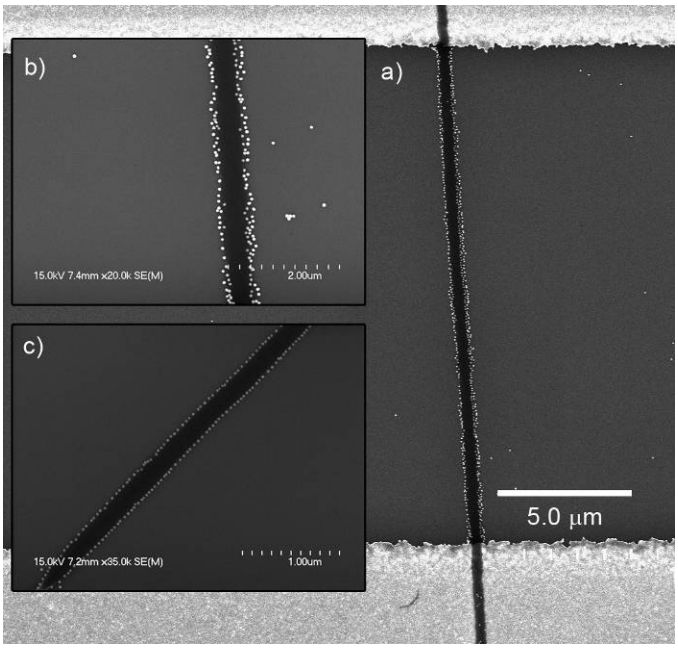

Figure 6.3. Edge-effect 60 nm Au particle deposition. (a) – (c) If a PAH solution that is greater than 3 months old is electrospun, the 60 nm Au self-assemble onto the edges of nanofiber.

In order to develop an electrically conducting nanoparticle array device, ~10 nm Au particles are nucleated onto the PAH fiber between the 60 nm Au particles (Fig. 6.4). Essentially, the ~10 nm particles serve to "stitch" the nanoparticle array together, as the 60 nm particles have an interparticle distance too large for the percolation of current. The ~10 nm particles are formed by immersing the sample into a quartz cuvette or an electrochemistry cell with a 1.23 x 10^{-4} M gold(III) trihydrate ($HAuCl_4 \cdot 3H_20$) solution. The cuvette is exposed to UV light with a wavelength of 260 – 270 nm (Fig. 6.5(a)). UV

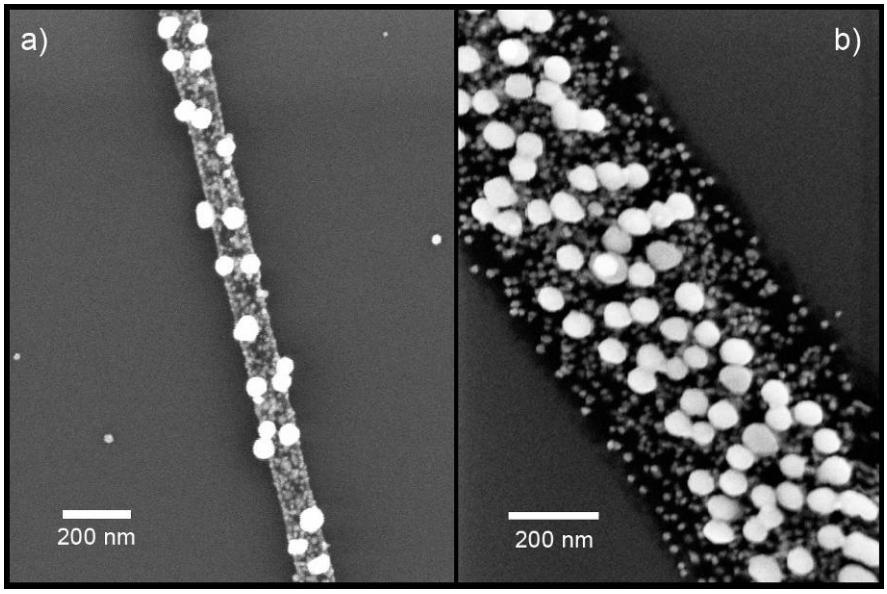

Figure 6.4. FESEM images of UV light reduced Au nanoparticles. (a) An FESEM image of the ~10 nm Au particles formed on an ~60 diameter PAH fiber due to the reduction of Au^{3+} by the UV light and amine groups of PAH. Particles have a close-packed morphology on the fiber. (b) The nucleation of ~10 nm Au particles on an ~200 nm diameter PAH fiber is filled with voids.

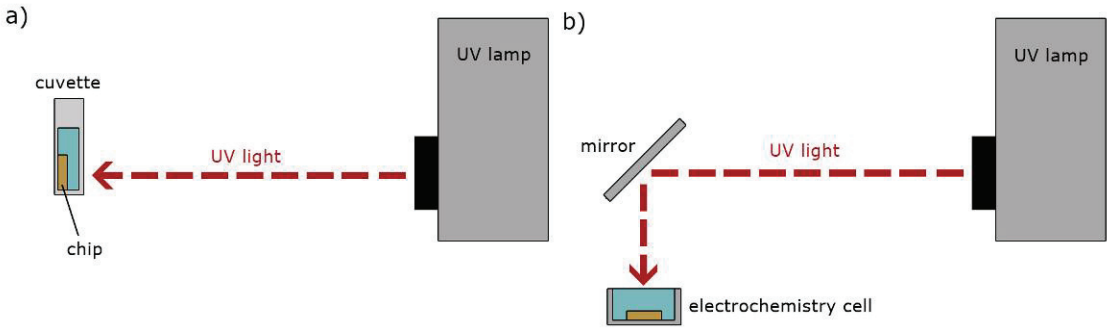

Figure 6.5. Au reduction using UV light and amine groups. (a) The chip with PAH nanofiber scaffolds and deposited 60 nm Au particles is vertically immersed in a solution of $HAuCl_4$ inside a quartz cuvette. UV light with wavelength 260 – 270 nm is applied to the device for 20 min to reduce Au^{3+} to Au^0 onto the PAH fibers. (b) Chips can also be mounted horizontally using an electrochemistry cell and reflecting mirror. The UV exposure time increases to 30 min, due to lose of beam strength from the mirror to the sample.

light combined with the amine groups of the PAH fiber reduces the Au^{3+} from $HAuCl_4$ to Au^0 directly onto the fiber.[167] The amino ($-NH_2$) group of the PAH fiber acts as a reducing agent and stabilizing agent for the nucleation of Au particles.[167] After ~20 min of UV light exposure, ~10 nm Au particles have formed on the PAH fiber between the 60 nm Au particles (Fig. 6.4). Spherical ~10 nm particles were deposited due to the PAH polymer adsorbing onto the surface of the particles, preventing agglomeration and controlling particle growth.[167] For Au nanoparticle growth in an electrochemistry cell, the chip is mounted horizontally with a quartz window to prevent the evaporation of the 1.23×10^{-4} M $HAuCl_4$ solution (Fig. 6.5(b)). A silicon wafer mirror is used to deflect the UV light beam downward into the electrochemistry cell. A longer exposure time of UV light, ~30 min, is required to grow the ~10 nm Au particles due to a lessening of the UV beam strength from the reflecting mirror.

Conductivity through the nanoparticle array devices is improved by electroplating with Au at the interconnection between the device and the Au electrodes (Fig. 6.6). By electroplating, a more robust contact is formed for the device. Electroplation is performed by placing the device into a 3-terminal electrochemistry cell (working, counter, and reference electrode) with a solution of 0.01 M $HAuCl_4$. A bias of 500 mV is applied to the working electrode (i.e., the electrode targeted for improved device contact) with a potentiostat for ~1 min. During bias application, Au^0 metal is reduced from the Au^{3+} of the $HAuCl_4$ solution onto the PAH fibers at the edge of the Au electrode (Fig. 6.6(a)). By applying bias for >1 minute, electroplation can be significantly extended onto the device across the electrode gap (Fig. 6.6(b)). Electroplation can only be performed

on PAH fibers with deposited Au particles. No electroplation will occur on the PAH fibers alone.

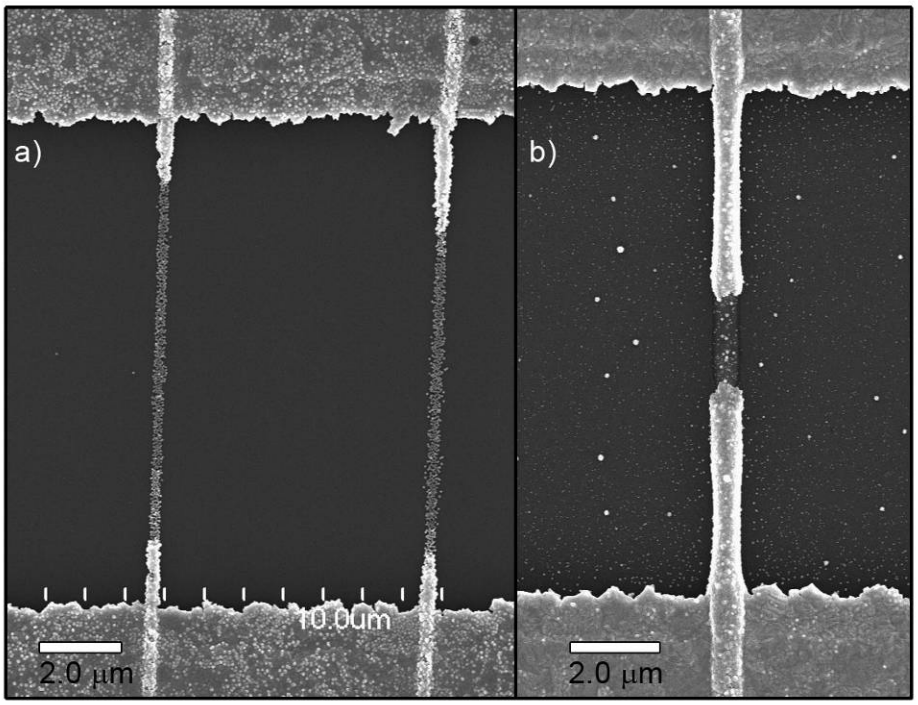

Figure 6.6. Au electroplated devices. (a) FESEM image of the electroplated contact region of the devices for a 1 min exposure time. Au metal reduces onto the edges of the PAH scaffold in contact with the Au pad. (b) The electroplated Au can be extended from the electrode into the gap by applying a bias for > 1 min.

6.4 ELECTRICAL CHARACTERIZATION OF NANOPARTICLE ARRAY DEVICES

The nanoparticle arrays assembled on the PAH nanofibers spanning across the electrode gaps are electrically conductive. As bias, V, is applied across the device, current, I, flows through the nanoparticle array according to the second-order phase transition, $I \sim [(V-V_T)/ V_T]^{\zeta}$, where ζ is the critical exponent, once the threshold voltage, V_T, is surpassed.[7] The critical exponent for 1D and 2D arrays is analytically determined to be 1 and 5/3, respectively.[7] Larger ζ values correspond to devices with sharper switching speeds and improved sensor sensitivities. This is due to the fact that smaller changes in voltage correspond to higher increases in current for large ζ.

For a device constructed on a 60 nm diameter fiber, the contacts are electroplated and a close-packed layer of ~10 nm Au particles has deposited between the 60 nm Au particles (Fig. 6.7). The nanoparticles making up the array have a quasi-1D morphology where the array is ~4 – 6 particles wide, particle diameters are ~10 nm. There are minimal voids within the array. The room temperature I-V behavior of a device spanning across a 100 μm electrode gap exhibits nominally Ohmic behavior (Fig. 6.8). Analysis of the I-V curve by a non-linear fitting function determines that the V_T = -0.1 V and ζ = 1.27. Analytical[7] and experimental[47] studies have shown that 1D arrays of nanoparticles have ζ = 1 and ~1, respectively, ie., the 1D arrays have Ohmic I-V behavior at $V > V_T$. In an experiment involving a 1D chain of 30 nm diameter carbon nanoparticles, exponent values ranged from $\zeta = 1.03 – 2.32$ at 4.2 K.[47] For quasi-1D arrays, experimental[25,27,48-50] and analytical[52] studies report ζ values ranging from 1.2 ± 0.2 to 1.95. For a quasi-1D

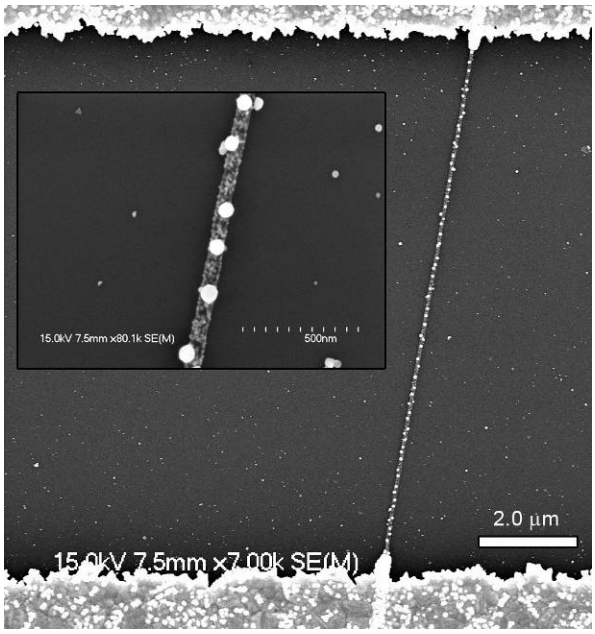

Figure 6.7. A 60 nm diameter fiber device. (a) FESEM image of a 60 nm wide PAH fiber device with electroplated contacts across a 10 μm gap. (b) The deposition of ~10 nm Au particles has a close-packed quasi-1D array morphology.

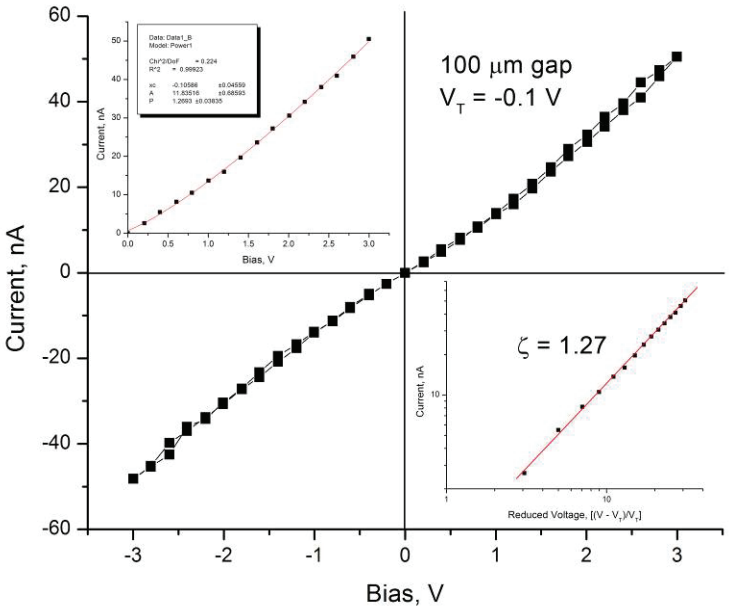

Figure 6.8. Electrical behavior of a nominally Ohmic device. For a 100 μm gap device, the I-V curve is nominally Ohmic, where a fitting function (upper inset) determines that ζ = 1.27 (lower inset) at room temperature. The V_T = -0.1 V for the device. The low ζ value is attributed to an array with a close-packed quasi-1D architecture.

array made up of 1.4 nm Au particles assembled on a poly-L-lysine biopolymer scaffold, the devices demonstrated $\zeta = 1.2 \pm 0.2$ and a $V_T = 12 \pm 1$ V at room temperature.[25,27] While for 2D arrays the ζ value is analytically predicted to be 5/3,[7] experimental studies predominantly report ζ values >2.[8,37,41,42,53,54] The nearly Ohmic (i.e., $\zeta = 1$) value of $\zeta = 1.26$ for the PAH fiber nanoparticle array device is indicative of a quasi-1D array with a prevalent 1D percolation path.

One means of increasing ζ, and thereby improving switching gain, is by increasing the tortuosity of the percolation path of the array. By introducing large voids within the array topology, the ζ increases as the tortuosity of the array increases.[42] In order to increase the tortuosity of the PAH nanoparticle array devices, a larger diameter PAH fiber (~200 nm) was utilized (Fig. 6.9). With an increase in fiber diameter, the deposition of the ~10 nm Au particles has a high void density. The nanoparticle array still has a quasi-1D morphology, but with large voids amidst the percolating chains of particles, or necklaces. Essentially, the arrays are a quasi-1D network of nanoparticle necklaces arranged as a 2D (i.e., monolayer) array with a high void density. Arrays with comparable architecture, i.e., nanoparticle necklaces, have been experimentally shown to exhibit single-electron switching, or V_T, at room temperature with $\zeta \sim 5/3$.[48] A PAH fiber nanoparticle array device, also spanning across a 100 μm gap, exhibits highly non-linear I-V behavior at room temperature with a significant $V_T = 0.5$ V and a large $\zeta = 2.76$ (Fig. 6.10). The impressive electrical properties are associated with a device constructed out of a larger diameter PAH fiber with a high array percolation path tortuosity. Given the large $\zeta =$

2.76 value and room temperature V_T, the device is suitable for applications in sensors requiring high sensitivity.

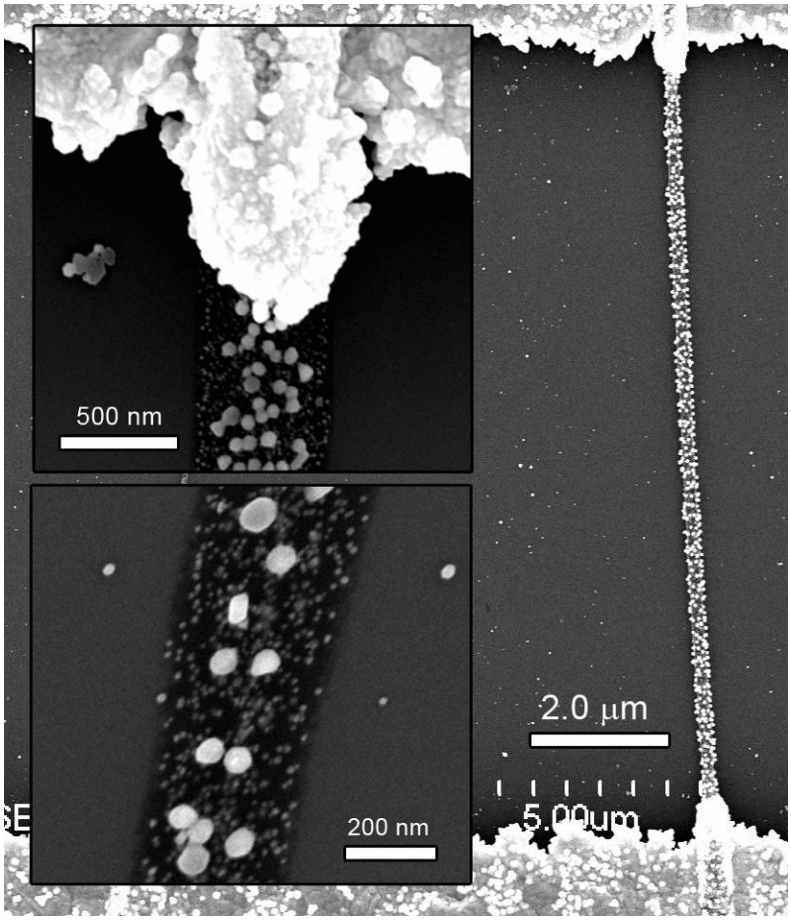

Figure 6.9. A 200 nm diameter fiber device. (a) FESEM of a fabricated ~200 nm diameter PAH fiber device across a 10 μm gap. The contacts have been electroplated with Au. (b) A high magnification image of the electroplated contact. (c) The ~10 nm Au array has a quasi-1D morphology with a high void density.

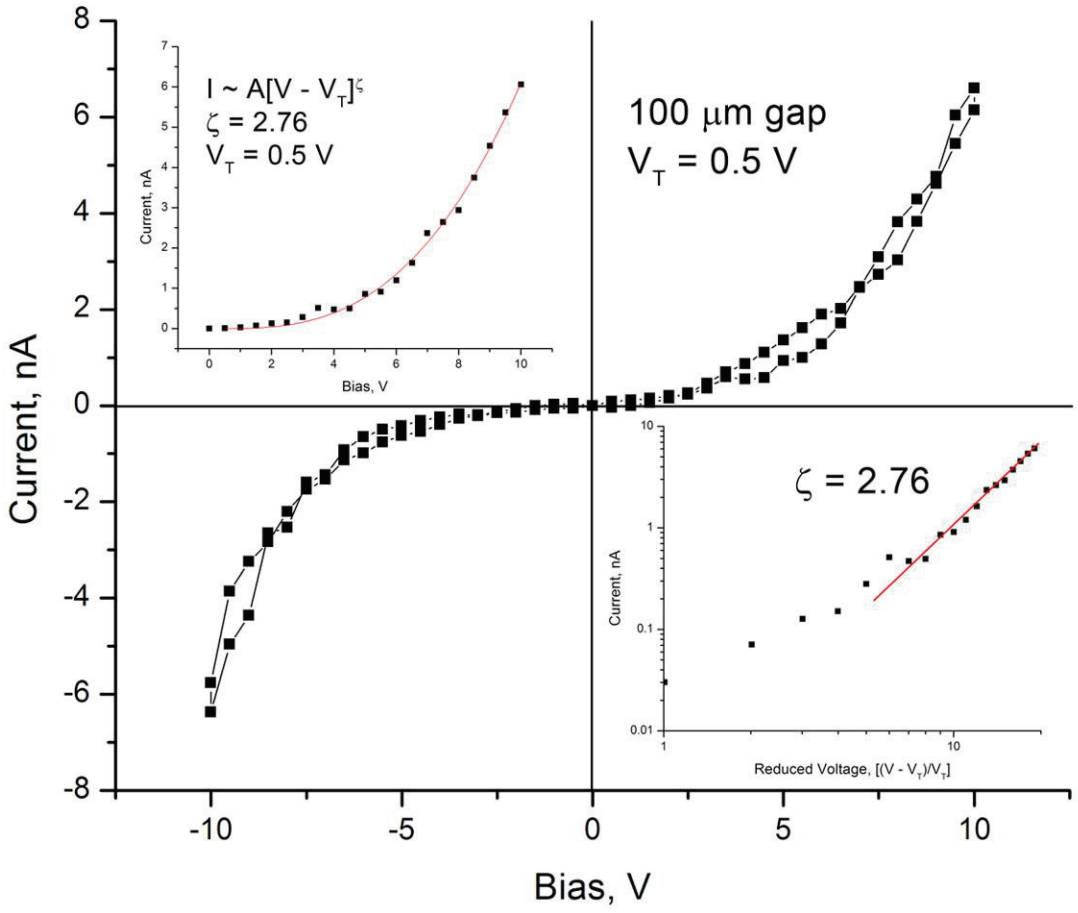

Figure 6.10. Single-electron switching behavior. The non-linear I-V plot for a 100 μm gap device has a V_T = 0.5 V and ζ = 2.76 (lower inset) at room temperature. A non-linear fitting function (upper inset) was used to determine the V_T and ζ values for the void-filled, quasi-1D array.

6.5 SUMMARY AND CONCLUSIONS

A technique to fabricate aligned quasi-1D nanoparticle array devices onto PAH nanofibers was presented. The electrospun nanofibers of diameter 60 – 200 nm were deposited and aligned across electrodes by use of a rolling drum collector. The amine groups making up the PAH nanofiber were used to self-assemble 60 nm Au particles onto the fibers. As the interparticle distances of the 60 nm Au particles were too large for conductivity, a combination of UV light and PAH amino groups allowed Au metal to be directly reduced onto the fibers as ~10 nm diameter spherical particles. Device conductivity was improved by electroplating the array interconnection point to the electrodes with Au metal reduction. By electroplating, robust device contacts were formed.

The electrical behavior of the array devices was influenced by the morphology of the nanoparticle arrays. Current flowed according to the second-order phase transition after a threshold voltage, V_T, was met as $I \sim [(V - V_T)/ V_T]^{\zeta}$, where ζ is the critical exponent. For a device fabricated on a ~60 nm diameter fiber, the combination of UV and amino groups reduced ~10 nm Au particles as a close-packed quasi-1D array onto the fiber. The resulting nominally Ohmic current-voltage (I-V) curve, with $\zeta = 1.27$, was attributed to the close-packed structure of the array. By utilizing a larger PAH fiber of diameter ~200 nm, a quasi-1D nanoparticle array with large voids was developed. The high void density increased the tortuosity of the percolation path of the array, thus increasing ζ. Room temperature non-linear I-V curves with a $V_T = 0.5$ V and $\zeta = 2.76$ were exhibited. Large ζ values correspond to devices with sharper switching speeds and higher switching gains.

The remarkable electrical properties of the void filled quasi-1D devices at room temperature could lead to applications in high sensitivity sensors and nanoelectronics.

CHAPTER 7

SUMMARY AND CONCLUSIONS

The fabrication and electrical properties of quasi-1D nanoparticle necklace network arrays are discussed. In necklace network array devices, a threshold bias, V_T, must be met in order for current, I, to flow through the array. Once at bias $V > V_T$, $I \sim [(V - V_T)/V_T]^{\zeta}$, where ζ is a critical exponent. Experimental studies have shown that the current through a single nanoparticle (0D) device can be gated by a single electron, thus operating as a single electron transistor. Devices with such single electron switching are known as single electron devices (SEDs). In order to observe the single electron effect of 0D devices, cryogenic temperatures are required. Single particle devices with higher operating temperature are feasible by using a particle of diameter <2 nm, but the degeneracy of the kinetic energy of the electron causes significant noise.

A SED made up of "large" nanoparticles, i.e., >5 nm, with robust room temperature operation is formed by using an array of particles. In arrays, V_T is enhanced compared to a single particle device and is temperature dependent, increasing as temperature, T, decreases. For 0D devices, V_T is temperature independent and $\zeta = 1$ (i.e., Ohm's law). In arrays $\zeta > 1$, thus leading to larger switching gain. One-dimensional (1D) arrays have a temperature independent ζ with a non-linear $V_T(T)$ relationship. In two-dimensional (2D) arrays, $\zeta \sim 2$ and there is a linear $V_T(T)$ dependence. The quasi-1D nanoparticle necklace network array is an amalgamation of 1D and 2D arrays, where 1D nanoparticle necklaces with large voids are arranged in a 2D monolayer. In this study, necklaces were self-

assembled in solution through ion mediation and then deposited by electrostatic attraction onto SiO_2 substrates, PMMA film scaffolds patterned by PEO fiber shadow masking, and patterned inkless microcontact printed PDMS scaffolds. Electrospun positively charged poly(allylamine hydrochloride) (PAH) nanofibers were used to self-assemble negatively charged nanoparticles directly onto the nanofiber scaffold to form quasi-1D close-packed and void-filled necklace network arrays.

The nanoparticle necklace network array devices are characterized by: a) the presence of large voids within the array that increase the tortuosity of the percolation path of the electrons traversing the array. By increasing path tortuosity, disorder is increased and the exponent, ζ, which is a measure of how current rises at $V > V_T$, is significantly enhanced to as high as ~7 for a CdS cemented network. As array length (i.e., electrode gap distance) is reduced, ζ increases, as a reduction in array length increases path tortuosity. b) Comparable to 1D arrays, the $V_T(T)$ relationship is non-linear with a sharp change in slope at large T, allowing robust room temperature single-electron switching with large 10 nm diameter particles to be achieved. Increasing array length enhanced V_T, due to the inclusion of more quenched charges within the percolation path. c) The ζ is constant over a large range of biases, i.e. $(V/ V_T - 1)$ from 0 to 50, greatly increasing the operating range of the devices. To note, previously reported nanoparticle-based devices have not reported such large biases.

Current through the network arrays were biogated using the metabolic activity of live yeast cells. When methanotropic *Pichia pastoris* yeast cells coupled to the network array were exposed to methanol vapor, a nutrient, REDOX activity was measured and current

through the array was gated. In the absence of yeast, REDOX behavior was not exhibited by the network array during methanol exposure. Additionally, V_T was enhanced when the current through the network array fabricated on inkless microcontact printed PDMS scaffolds was chemically gated with methanol vapor.

The four advantages of nanoparticle necklace network arrays over other dimensional nanoparticle array devices (i.e. 0D, 1D, and 2D arrays) are: (i) room temperature operation is achieved by enhancing the switching voltage, V_T, orders of magnitude. The non-linear $V_T(T)$ relationship led to robust room temperature V_T values. (ii) The critical exponent can be significantly increased from $\zeta = 1$ (for a single particle device) and $\zeta \sim 2$ (for a 2D device) to as high as 7 (for a CdS cemented necklace device). (iii) Single-electron sensitivity combined with room temperature operation allow live microorganisms to be coupled to the network array for biogating, which could lead to the real-time study of cell kinetics, and (iv) Compared to single particle and 1D devices, the nanoparticle necklace network array devices are easily integrated with microelectronic circuitry. Given the robust room temperature V_T, high ζ, live cell coupling capability, and facile interconnectivity with electronics, nanoparticle necklace network arrays are an ideal medium for the development of SEDs that can function as highly sensitive chemical or biochemical nanodevices and sensors.

CHAPTER 8

FUTURE WORK

An electrical characterization and several fabrication techniques for nanoparticle necklace network array devices were presented. As the potential of nanoparticle necklace network arrays is just being realized, there are many exciting future avenues of study available.

1) The necklaces were cemented with the dielectric material CdS and studied at 295, 50, and 5 K. An interesting feature of cemented nanoparticle network arrays is that the critical exponent, ζ, increased with decreasing temperature, a behavior not exhibited by uncemented necklaces. The cement material led to complex ζ behavior that should be studied in more depth as the high $\zeta \sim 7$ values are highly promising switching gains. Additionally, more cement materials should be incorporated into the necklaces, such as ZnS, ZnO, and Eu_4O_3, and studied for their unique properties.

2) Once a variety of cement materials are included in the necklaces, an interesting application would be the development of an electronic nose. The different cement materials would chemically react to airborne molecules with a unique signature that could be catalogued. A collection of different cemented arrays would be exposed to known chemicals, the chemicals would gate the devices (a shift in V_T), and a response would be recorded and fed to a pattern recognition software. The

software would be trained to identify the chemical based on the global gating response of the array collection. The cemented array collection could be self-assembled in solution and deposited onto a patterned scaffold, such as PMMA films or inkless microcontact printed PDMS. The arrays could also be fabricated onto the aligned electrospun PAH nanofibers.

3) Biogating by live yeast cells coupled to the network array was performed in a humid environment. A better design for a biosensor would be in an aqueous environment that would allow the microorganism to be coupled to the network array for longer than ~14 hrs under more optimal cell conditions. In order to achieve aqueous biogating, the nanoparticle necklace network array device should be designed so as to isolate the Au electrodes from the testing solution. Only the network array should be in contact with the solution and cells. Once the network array is isolated, biogating and electrochemical gating could be performed.

4) A more in depth study of the relationship of array length, i.e. gap distance, to V_T and ζ should be pursued at a range of operating temperatures. By using devices with a larger range of lengths, such as 5 to 100 μm, a better relationship would be attained that would allow devices to be tailored to achieve targeted V_T and ζ values.

In conclusion, nanoparticle necklace network arrays are a versatile and promising platform for nanodevice development.

Reference List

1. Gorter, C. J. A possible explanation of the increase of the electrical resistance of thin metal films at low temperatures and small field strengths. *Physica* **1951,** *17*, 777-780.

2. Neugebauer, C. A.; Webb, M. B. Electrical Conduction Mechanism in Ultrathin, Evaporated Metal Films. *Journal of Applied Physics* **1962,** *33* (1), 74-82.

3. Kulik, I. O.; Shekhter, R. I. Kinetic Phenomena and Charge Discreteness Effects in Granulated Media. *Soviet Journal of Experimental and Theoretical Physics* **1975,** *41*, 308-316.

4. Likharev, K. K. Single-Electron Transistors - Electrostatic Analogs of the Dc Squids. *Ieee Transactions on Magnetics* **1987,** *23* (2), 1142-1145.

5. Fulton, T. A.; Dolan, G. J. Observation of Single-Electron Charging Effects in Small Tunnel-Junctions. *Physical Review Letters* **1987,** *59* (1), 109-112.

6. Wilkins, R.; Benjacob, E.; Jaklevic, R. C. Scanning-Tunneling-Microscope Observations of Coulomb Blockade and Oxide Polarization in Small Metal Droplets. *Physical Review Letters* **1989,** *63* (7), 801-804.

7. Middleton, A. A.; Wingreen, N. S. Collective Transport in Arrays of Small Metallic Dots. *Physical Review Letters* **1993,** *71* (19), 3198-3201.

8. Parthasarathy, R.; Lin, X. M.; Elteto, K.; Rosenbaum, T. F.; Jaeger, H. M. Percolating through networks of random thresholds: Finite temperature electron tunneling in metal nanocrystal arrays. *Physical Review Letters* **2004,** *92*, 076801.

9. Kastner, M. A. The Single-Electron Transistor. *Reviews of Modern Physics* **1992,** *64* (3), 849-858.

10. Vankempen, H.; Dubois, J. G. A.; Gerritsen, J. W.; Schmid, G. Small Metallic Particles Studied by Scanning-Tunneling-Microscopy. *Physica B-Condensed Matter* **1995,** *204* (1-4), 51-56.

11. Klein, D. L.; Roth, R.; Lim, A. K. L.; Alivisatos, A. P.; Mceuen, P. L. A single-electron transistor made from a cadmium selenide nanocrystal. *Nature* **1997,** *389* (6652), 699-701.

12. Persson, S. H. M.; Olofsson, L.; Gunnarsson, L. A self-assembled single-electron tunneling transistor. *Applied Physics Letters* **1999,** *74* (17), 2546-2548.

13. Bolotin, K. I.; Kuemmeth, F.; Pasupathy, A. N.; Ralph, D. C. Metal-nanoparticle single-electron transistors fabricated using electromigration. *Applied Physics Letters* **2004,** *84* (16), 3154-3156.

14. Park, H.; Lim, A. K. L.; Alivisatos, A. P.; Park, J.; Mceuen, P. L. Fabrication of metallic electrodes with nanometer separation by electromigration. *Applied Physics Letters* **1999,** *75* (2), 301-303.

15. Wang, B.; Wang, H. Q.; Li, H. X.; Zeng, C. G.; Hou, J. G.; Xiao, X. D. Tunable single-electron tunneling behavior of ligand-stabilized gold particles on self-assembled monolayers. *Physical Review B* **2001,** *63*, 035403.

16. Andres, R. P.; Datta, S.; Dorogi, M.; Gomez, J.; Henderson, J. I.; Janes, D. B.; Kolagunta, V. R.; Kubiak, C. P.; Mahoney, W.; Osifchin, R. F.; Reifenberger, R.; Samanta, M. P.; Tian, W. Room temperature Coulomb blockade and Coulomb staircase from self-assembled nanostructures. *Journal of Vacuum Science & Technology A* **1996,** *14* (3), 1178-1183.

17. Roch, N.; Vincent, R.; Elste, F.; Harneit, W.; Wernsdorfer, W.; Timm, C.; Balestro, F. Cotunneling through a magnetic single-molecule transistor based on N@C-60. *Physical Review B* **2011,** *83*, 081407.

18. Giaever, I.; Zeller, H. R. Superconductivity of Small Tin Particles Measured by Tunneling. *Physical Review Letters* **1968,** *20* (26), 1504-1507.

19. Giaever, I.; Zeller, H. R. Tunneling Into and Through Evaporated Semiconducting Films. *Journal of Vacuum Science & Technology* **1969,** *6* (4), 502-508.

20. Lambe, J.; Jaklevic, R. C. Charge-Quantization Studies Using A Tunnel Capacitor. *Physical Review Letters* **1969,** *22* (25), 1371-1375.

21. Cavicchi, R. E.; Silsbee, R. H. Coulomb Suppression of Tunneling Rate from Small Metal Particles. *Physical Review Letters* **1984,** *52* (16), 1453-1456.

22. Averin, D. V.; Likharev, K. K. Coulomb Blockade of Single-Electron Tunneling, and Coherent Oscillations in Small Tunnel-Junctions. *Journal of Low Temperature Physics* **1986,** *62* (3-4), 345-373.

23. Likharev, K. K.; Zorin, A. B. Theory of the Bloch-Wave Oscillations in Small Josephson-Junctions. *Journal of Low Temperature Physics* **1985,** *59* (3-4), 347-382.

24. Likharev, K. K. Single-electron devices and their applications. *Proceedings of the Ieee* **1999,** *87* (4), 606-632.

25. Berven, C. A.; Clarke, L.; Mooster, J. L.; Wybourne, M. N.; Hutchison, J. E. Defect-tolerant single-electron charging at room temperature in metal nanoparticle decorated biopolymers. *Advanced Materials* **2001,** *13* (2), 109-113.

26. Averin, D. V.; Korotkov, A. N. Correlated Single-Electron Tunneling Via Mesoscopic Metal Particles - Effects of the Energy Quantization. *Journal of Low Temperature Physics* **1990,** *80* (3-4), 173-185.

27. Berven, C. A.; Wybourne, M. N.; Clarke, L.; Longstreth, L.; Hutchison, J. E.; Mooster, J. L. Background charge fluctuations and the transport properties of biopolymer-gold nanoparticle complexes. *Journal of Applied Physics* **2002,** *92* (8), 4513-4517.

28. Simon, U. Charge transport in nanoparticle arrangements. *Advanced Materials* **1998,** *10* (17), 1487-1492.

29. Meir, Y.; Wingreen, N. S.; Lee, P. A. Transport Through A Strongly Interacting Electron-System - Theory of Periodic Conductance Oscillations. *Physical Review Letters* **1991,** *66* (23), 3048-3051.

30. Beenakker, C. W. J. Theory of Coulomb-Blockade Oscillations in the Conductance of A Quantum Dot. *Physical Review B* **1991,** *44* (4), 1646-1656.

31. Shekhter, R. I. Zero Anomalies of the Resistance of Tunnel Junctions Containing Metallic Inclusions in the Oxide Layer. *Soviet Journal of Experimental and Theoretical Physics* **1973,** *36*, 747-750.

32. Mceuen, P. L.; Foxman, E. B.; Meirav, U.; Kastner, M. A.; Meir, Y.; Wingreen, N. S.; Wind, S. J. Transport Spectroscopy of A Coulomb Island in the Quantum Hall Regime. *Physical Review Letters* **1991,** *66* (14), 1926-1929.

33. Kastner, M. A. Artificial Atoms. *Physics Today* **1993,** *46* (1), 24-31.

34. Meirav, U.; Foxman, E. B. Single-electron phenomena in semiconductors. *Semiconductor Science and Technology* **1996,** *11* (3), 255-284.

35. Kouwenhoven, L. P.; Markus, C. M.; Mceuen, P. L.; Tarucha, S.; Westerfelt, R. M.; Wingreen, N. S. Electron transport in quantum dots. In *Mesoscopic Electron Transfer*, Sohn, L., et al., Eds.; Kluwer: Dordrecht, 1997; pp 105-215.

36. Ingold, G. L.; Nazarov, Y. V. Charge tunneling rates in ultrasmall junctions. In *Single Charge Tunneling*, Grabert, H., Devoret, M. H., Eds.; Plenum: New York, 1992; pp 21-108.

37. Parthasarathy, R.; Lin, X. M.; Jaeger, H. M. Electronic transport in metal nanocrystal arrays: The effect of structural disorder on scaling behavior. *Physical Review Letters* **2001,** *87*, 186807.

38. Elteto, K.; Antonyan, E. G.; Nguyen, T. T.; Jaeger, H. M. Model for the onset of transport in systems with distributed thresholds for conduction. *Physical Review B* **2005,** *71* (6), 064206.

39. Tremblay, F.; Pepper, M.; Newbury, R.; Ritchie, D.; Peacock, D. C.; Frost, J. E. F.; Jones, G. A. C.; Hill, G. Activationless Hopping of Correlated Electrons in N-Type Gas. *Physical Review B* **1989,** *40* (5), 3387-3389.

40. Shahar, D.; Ovadyahu, Z. Dimensional Crossover in the Hopping Regime Induced by An Electric-Field. *Physical Review Letters* **1990,** *64* (19), 2293-2296.

41. Ancona, M. G.; Kruppa, W.; Rendell, R. W.; Snow, A. W.; Park, D.; Boos, J. B. Coulomb blockade in single-layer Au nanocluster films. *Physical Review B* **2001,** *64* (3), 033408.

42. Blunt, M. O.; Suvakov, M.; Pulizzi, F.; Martin, C. P.; Pauliac-Vaujour, E.; Stannard, A.; Rushforth, A. W.; Tadic, B.; Moriarty, P. Charge transport in cellular nanoparticle networks: Meandering through nanoscale mazes. *Nano Letters* **2007,** *7* (4), 855-860.

43. Geigenmuller, U.; Schon, G. Single-Electron Effects in Arrays of Normal Tunnel-Junctions. *Europhysics Letters* **1989,** *10* (8), 765-770.

44. Andres, R. P.; Bielefeld, J. D.; Henderson, J. I.; Janes, D. B.; Kolagunta, V. R.; Kubiak, C. P.; Mahoney, W. J.; Osifchin, R. G. Self-assembly of a two-dimensional superlattice of molecularly linked metal clusters. *Science* **1996,** *273* (5282), 1690-1693.

45. Klein, D. L.; Mceuen, P. L.; Katari, J. E. B.; Roth, R.; Alivisatos, A. P. An approach to electrical studies of single nanocrystals. *Applied Physics Letters* **1996,** *68* (18), 2574-2576.

46. Reichhardt, C.; Reichhardt, C. J. O. Temperature and ac effects on charge transport in arrays of metallic dots. *Physical Review B* **2003,** *68* (16), 165305.

47. Bezryadin, A.; Dekker, C.; Schmid, G. Electrostatic trapping of single conducting nanoparticles between nanoelectrodes. *Applied Physics Letters* **1997,** *71* (9), 1273-1275.

48. Kane, J.; Inan, M.; Saraf, R. F. Self-Assembled Nanoparticle Necklaces Network Showing Single-Electron Switching at Room Temperature and Biogating Current by Living Microorganisms. *Acs Nano* **2010,** *4* (1), 317-323.

49. Clarke, L.; Wybourne, M. N.; Yan, M. D.; Cai, S. X.; Keana, J. F. W. Transport in gold cluster structures defined by electron-beam lithography. *Applied Physics Letters* **1997,** *71* (5), 617-619.

50. Elteto, K.; Lin, X. M.; Jaeger, H. M. Electronic transport in quasi-one-dimensional arrays of gold nanocrystals. *Physical Review B* **2005,** *71* (20), 205412.

51. Maheshwari, V.; Kane, J.; Saraf, R. F. Self-assembly of a micrometers-long one-dimensional network of cemented Au nanoparticles. *Advanced Materials* **2008,** *20* (2), 284-287.

52. Reichhardt, C.; Reichhardt, C. J. O. Charge transport transitions and scaling in disordered arrays of metallic dots. *Physical Review Letters* **2003,** *90* (4), 046802.

53. Black, C. T.; Murray, C. B.; Sandstrom, R. L.; Sun, S. H. Spin-dependent tunneling in self-assembled cobalt-nanocrystal superlattices. *Science* **2000,** *290* (5494), 1131-1134.

54. Ancona, M. G.; Kooi, S. E.; Kruppa, W.; Snow, A. W.; Foos, E. E.; Whitman, L. J.; Park, D.; Shirey, L. Patterning of narrow Au nanocluster lines using V2O5 nanowire masks and ion-beam milling. *Nano Letters* **2003,** *3* (2), 135-138.

55. Wuelfing, W. P.; Green, S. J.; Pietron, J. J.; Cliffel, D. E.; Murray, R. W. Electronic conductivity of solid-state, mixed-valent, monolayer-protected Au clusters. *Journal of the American Chemical Society* **2000,** *122* (46), 11465-11472.

56. Heath, J. R.; Knobler, C. M.; Leff, D. V. Pressure/temperature phase diagrams and superlattices of organically functionalized metal nanocrystal monolayers: The influence of particle size, size distribution, and surface passivant. *Journal of Physical Chemistry B* **1997,** *101* (2), 189-197.

57. Bourgoin, J. P.; Kergueris, C.; Lefevre, E.; Palacin, S. Langmuir-Blodgett films of thiol-capped gold nanoclusters: fabrication and electrical properties. *Thin Solid Films* **1998,** *327*, 515-519.

58. Markovich, G.; Collier, C. P.; Heath, J. R. Reversible metal-insulator transition in ordered metal nanocrystal monolayers observed by impedance spectroscopy. *Physical Review Letters* **1998,** *80* (17), 3807-3810.

59. Santhanam, V.; Liu, J.; Agarwal, R.; Andres, R. P. Self-assembly of uniform monolayer arrays of nanoparticles. *Langmuir* **2003,** *19* (19), 7881-7887.

60. Bethell, D.; Brust, M.; Schiffrin, D. J.; Kiely, C. From monolayers to nanostructured materials: An organic chemist's view of self-assembly. *Journal of Electroanalytical Chemistry* **1996,** *409* (1-2), 137-143.

61. Zabet-Khosousi, A.; Dhirani, A. A. Charge transport in nanoparticle assemblies. *Chemical Reviews* **2008,** *108* (10), 4072-4124.

62. Fuller, S. B.; Wilhelm, E. J.; Jacobson, J. M. Ink-jet printed nanoparticle microelectromechanical systems. *Journal of Microelectromechanical Systems* **2002,** *11* (1), 54-60.

63. Rendell, R. W.; Ancona, M. G.; Kruppa, W.; Foos, E. E.; Snow, A. W.; Park, D.; Boos, J. B. Electron transport in nanocluster films with random voids. *Ieee Transactions on Nanotechnology* **2003,** *2* (2), 75-81.

64. Zeng, H.; Black, C. T.; Sandstrom, R. L.; Rice, P. M.; Murray, C. B.; Sun, S. H. Magnetotransport of magnetite nanoparticle arrays. *Physical Review B* **2006,** *73* (2), 020404.

65. Yakimov, A. I.; Dvurechenskii, A. V.; Kirienko, V. V.; Yakovlev, Y. I.; Nikiforov, A. I.; Adkins, C. J. Long-range Coulomb interaction in arrays of self-assembled quantum dots. *Physical Review B* **2000,** *61* (16), 10868-10876.

66. Beverly, K. C.; Sampaio, J. F.; Heath, J. R. Effects of size dispersion disorder on the charge transport in self-assembled 2-D Ag nanoparticle arrays. *Journal of Physical Chemistry B* **2002,** *106* (9), 2131-2135.

67. Yu, D.; Wang, C. J.; Wehrenberg, B. L.; Guyot-Sionnest, P. Variable range hopping conduction in semiconductor nanocrystal solids. *Physical Review Letters* **2004,** *92* (21), 216802.

68. Tran, T. B.; Beloborodov, I. S.; Lin, X. M.; Bigioni, T. P.; Vinokur, V. M.; Jaeger, H. M. Multiple cotunneling in large quantum dot arrays. *Physical Review Letters* **2005,** *95* (7), 076806.

69. Tran, T. B.; Beloborodov, I. S.; Hu, J. S.; Lin, X. M.; Rosenbaum, T. F.; Jaeger, H. M. Sequential tunneling and inelastic cotunneling in nanoparticle arrays. *Physical Review B* **2008,** *78* (7), 075437.

70. Xu, K.; Qin, L. D.; Heath, J. R. The crossover from two dimensions to one dimension in granular electronic materials. *Nature Nanotechnology* **2009,** *4* (6), 368-372.

71. Cordan, A. S.; Leroy, Y.; Goltzene, A.; Pepin, A.; Vieu, C.; Mejias, M.; Launois, H. Temperature behavior of multiple tunnel junction devices based on disordered dot arrays. *Journal of Applied Physics* **2000,** *87* (1), 345-352.

72. Sato, T.; Ahmed, H.; Brown, D.; Johnson, B. F. G. Single electron transistor using a molecularly linked gold colloidal particle chain. *Journal of Applied Physics* **1997,** *82* (2), 696-701.

73. Lee, C. S.; Lee, H.; Westervelt, R. M. Microelectromagnets for the control of magnetic nanoparticles. *Applied Physics Letters* **2001,** *79* (20), 3308-3310.

74. Xia, Y. N.; Yin, Y. D.; Lu, Y.; McLellan, J. Template-assisted self-assembly of spherical colloids into complex and controllable structures. *Advanced Functional Materials* **2003,** *13* (12), 907-918.

75. Tang, Z. Y.; Kotov, N. A. One-dimensional assemblies of nanoparticles: Preparation, properties, and promise. *Advanced Materials* **2005,** *17* (8), 951-962.

76. Kraus, T.; Malaquin, L.; Schmid, H.; Riess, W.; Spencer, N. D.; Wolf, H. Nanoparticle printing with single-particle resolution. *Nature Nanotechnology* **2007,** *2* (9), 570-576.

77. Huang, J. X.; Tao, A. R.; Connor, S.; He, R. R.; Yang, P. D. A general method for assembling single colloidal particle lines. *Nano Letters* **2006,** *6* (3), 524-529.

78. Braun, E.; Eichen, Y.; Sivan, U.; Ben-Yoseph, G. DNA-templated assembly and electrode attachment of a conducting silver wire. *Nature* **1998,** *391* (6669), 775-778.

79. Ugarte, D.; Chatelain, A.; deHeer, W. A. Nanocapillarity and chemistry in carbon nanotubes. *Science* **1996,** *274* (5294), 1897-1899.

80. Patolsky, F.; Weizmann, Y.; Lioubashevski, O.; Willner, I. Au-nanoparticle nanowires based on DNA and polylysine templates. *Angewandte Chemie-International Edition* **2002,** *41* (13), 2323-2327.

81. Minko, S.; Kiriy, A.; Gorodyska, G.; Stamm, M. Mineralization of single flexible polyelectrolyte molecules. *Journal of the American Chemical Society* **2002,** *124* (34), 10192-10197.

82. Jiang, K. Y.; Eitan, A.; Schadler, L. S.; Ajayan, P. M.; Siegel, R. W.; Grobert, N.; Mayne, M.; Reyes-Reyes, M.; Terrones, H.; Terrones, M. Selective attachment of gold nanoparticies to nitrogen-doped carbon nanotubes. *Nano Letters* **2003,** *3* (3), 275-277.

83. Kumar, A.; Pattarkine, M.; Bhadbhade, M.; Mandale, A. B.; Ganesh, K. N.; Datar, S. S.; Dharmadhikari, C. V.; Sastry, M. Linear superclusters of colloidal gold particles by electrostatic assembly on DNA templates. *Advanced Materials* **2001,** *13* (5), 341-344.

84. Warner, M. G.; Hutchison, J. E. Linear assemblies of nanoparticles electrostatically organized on DNA scaffolds. *Nature Materials* **2003,** *2* (4), 272-277.

85. Bae, A. H.; Numata, M.; Hasegawa, T.; Li, C.; Kaneko, K.; Sakurai, K.; Shinkai, S. 1D arrangement of an nanoparticles by the helical structure of schizophyllan: A unique encounter of a natural product with inorganic

compounds. *Angewandte Chemie-International Edition* **2005,** *44* (13), 2030-2033.

86. Fu, X. Y.; Wang, Y.; Huang, L. X.; Sha, Y. L.; Gui, L. L.; Lai, L. H.; Tang, Y. Q. Assemblies of metal nanoparticles and self-assembled peptide fibrils - Formation of double helical and single-chain arrays of metal nanoparticles. *Advanced Materials* **2003,** *15* (11), 902-906.

87. Kane, J.; Saraf, R. F. Unpublished Work, 2011.

88. Tlusty, T.; Safran, S. A. Defect-induced phase separation in dipolar fluids. *Science* **2000,** *290* (5495), 1328-1331.

89. Tang, Z. Y.; Kotov, N. A.; Giersig, M. Spontaneous organization of single CdTe nanoparticles into luminescent nanowires. *Science* **2002,** *297* (5579), 237-240.

90. Lin, S.; Li, M.; Dujardin, E.; Girard, C.; Mann, S. One-dimensional plasmon coupling by facile self-assembly of gold nanoparticles into branched chain networks. *Advanced Materials* **2005,** *17* (21), 2553-2559.

91. Hong, M.; Wu, L. L.; Tian, L. F.; Zhu, J. Controlled Assembly of An, Ag, and Pt Nanoparticles with Chitosan. *Chemistry-A European Journal* **2009,** *15* (24), 5935-5941.

92. Na, H. B.; Song, I. C.; Hyeon, T. Inorganic Nanoparticles for MRI Contrast Agents. *Advanced Materials* **2009,** *21* (21), 2133-2148.

93. Couvreur, P.; Vauthier, C. Nanotechnology: Intelligent design to treat complex disease. *Pharmaceutical Research* **2006,** *23* (7), 1417-1450.

94. Berry, V.; Saraf, R. F. Self-assembly of nanoparticles on live bacterium: An avenue to fabricate electronic devices. *Angewandte Chemie-International Edition* **2005,** *44* (41), 6668-6673.

95. Maheshwari, V.; Saraf, R. F. High-resolution thin-film device to sense texture by touch. *Science* **2006,** *312* (5779), 1501-1504.

96. Maheshwari, V.; Saraf, R. Tactile devices to sense touch on a par with a human finger. *Angewandte Chemie-International Edition* **2008,** *47* (41), 7808-7826.

97. Peng, G.; Tisch, U.; Adams, O.; Hakim, M.; Shehada, N.; Broza, Y. Y.; Billan, S.; bdah-Bortnyak, R.; Kuten, A.; Haick, H. Diagnosing lung cancer in exhaled breath using gold nanoparticles. *Nature Nanotechnology* **2009,** *4* (10), 669-673.

98. Suganuma, Y.; Trudeau, P. E.; Dhirani, A. A. Multi-valued analogue information storage using self-assembled nanoparticle films. *Nanotechnology* **2005,** *16* (8), 1196-1203.

99. Nguyen, C.; O'Connor, D.; Saraf, R. F. Unpublished Work, 2011.

100. Bachtold, A.; Hadley, P.; Nakanishi, T.; Dekker, C. Logic circuits with carbon nanotube transistors. *Science* **2001,** *294* (5545), 1317-1320.

101. Huang, Y.; Duan, X. F.; Cui, Y.; Lauhon, L. J.; Kim, K. H.; Lieber, C. M. Logic gates and computation from assembled nanowire building blocks. *Science* **2001,** *294* (5545), 1313-1317.

102. Kong, J.; Franklin, N. R.; Zhou, C. W.; Chapline, M. G.; Peng, S.; Cho, K. J.; Dai, H. J. Nanotube molecular wires as chemical sensors. *Science* **2000,** *287* (5453), 622-625.

103. Tok, J. B. H.; Chuang, F. Y. S.; Kao, M. C.; Rose, K. A.; Pannu, S. S.; Sha, M. Y.; Chakarova, G.; Penn, S. G.; Dougherty, G. M. Metallic striped nanowires as multiplexed immunoassay platforms for pathogen detection. *Angewandte Chemie-International Edition* **2006,** *45* (41), 6900-6904.

104. Patolsky, F.; Timko, B. P.; Yu, G. H.; Fang, Y.; Greytak, A. B.; Zheng, G. F.; Lieber, C. M. Detection, stimulation, and inhibition of neuronal signals with high-density nanowire transistor arrays. *Science* **2006,** *313* (5790), 1100-1104.

105. Law, M.; Greene, L. E.; Johnson, J. C.; Saykally, R.; Yang, P. D. Nanowire dye-sensitized solar cells. *Nature Materials* **2005,** *4* (6), 455-459.

106. Harnack, O.; Ford, W. E.; Yasuda, A.; Wessels, J. M. Tris(hydroxymethyl)phosphine-capped gold particles templated by DNA as nanowire precursors. *Nano Letters* **2002,** *2* (9), 919-923.

107. Djalali, R.; Li, S. Y.; Schmidt, M. Amphipolar core-shell cylindrical brushes as templates for the formation of gold clusters and nanowires. *Macromolecules* **2002,** *35* (11), 4282-4288.

108. Kang, Y. J.; Erickson, K. J.; Taton, T. A. Plasmonic nanoparticle chains via a morphological, sphere-to-string transition. *Journal of the American Chemical Society* **2005,** *127* (40), 13800-13801.

109. Shipway, A. N.; Lahav, M.; Gabai, R.; Willner, I. Investigations into the electrostatically induced aggregation of Au nanoparticles. *Langmuir* **2000,** *16* (23), 8789-8795.

110. Maheshwari, V.; Saraf, R. F. Mineralization of monodispersed CdS nanoparticles on polyelectrolyte superstructure forming an electroluminescent "necklace-of-beads". *Langmuir* **2006,** *22* (21), 8623-8626.

111. Link, S.; El-Sayed, M. A. Spectral properties and relaxation dynamics of surface plasmon electronic oscillations in gold and silver nanodots and nanorods. *Journal of Physical Chemistry B* **1999,** *103* (40), 8410-8426.

112. Pantina, J. P.; Furst, E. M. Colloidal aggregate micromechanics in the presence of divalent ions. *Langmuir* **2006,** *22* (12), 5282-5288.

113. Maheshwari, V.; Saraf, R. F. Mineralization of monodispersed CdS nanoparticles on polyelectrolyte superstructure forming an electroluminescent "necklace-of-beads". *Langmuir* **2006,** *22* (21), 8623-8626.

114. Lopes, W. A.; Jaeger, H. M. Hierarchical self-assembly of metal nanostructures on diblock copolymer scaffolds. *Nature* **2001,** *414* (6865), 735-738.

115. DeVries, G. A.; Brunnbauer, M.; Hu, Y.; Jackson, A. M.; Long, B.; Neltner, B. T.; Uzun, O.; Wunsch, B. H.; Stellacci, F. Divalent metal nanoparticles. *Science* **2007,** *315* (5810), 358-361.

116. Huang, J. X.; Kim, F.; Tao, A. R.; Connor, S.; Yang, P. D. Spontaneous formation of nanoparticle stripe patterns through dewetting. *Nature Materials* **2005,** *4* (12), 896-900.

117. Rabani, E.; Reichman, D. R.; Geissler, P. L.; Brus, L. E. Drying-mediated self-assembly of nanoparticles. *Nature* **2003,** *426* (6964), 271-274.

118. Markovich, G.; Collier, C. P.; Henrichs, S. E.; Remacle, F.; Levine, R. D.; Heath, J. R. Architectonic quantum dot solids. *Accounts of Chemical Research* **1999,** *32* (5), 415-423.

119. Narayanan, S.; Wang, J.; Lin, X. M. Dynamical self-assembly of nanocrystal superlattices during colloidal droplet evaporation by in situ small angle x-ray scattering. *Physical Review Letters* **2004,** *93* (13).

120. Maier, S. A.; Kik, P. G.; Atwater, H. A.; Meltzer, S.; Harel, E.; Koel, B. E.; Requicha, A. A. G. Local detection of electromagnetic energy transport below the diffraction limit in metal nanoparticle plasmon waveguides. *Nature Materials* **2003,** *2* (4), 229-232.

121. McCarthy, A. J.; Coleman, R. G.; Nicol, M. J. The mechanism of the oxidative dissolution of colloidal gold in cyanide media. *Journal of the Electrochemical Society* **1998,** *145* (2), 408-414.

122. Lou, X.; Zhang, Y.; Qin, J.; Li, Z. A highly sensitive and selective fluorescent probe for cyanide based on the dissolution of gold nanoparticles and its

application in real samples. *Chemistry (Weinheim an der Bergstrasse, Germany)* **2011,** *17* (35), 9691-9696.

123. Sibirny, A. A.; Titorenko, V. I.; Gonchar, M. V.; Ubiyvovk, V. M.; Ksheminskaya, G. P.; Vitvitskaya, O. P. Genetic-Control of Methanol Utilization in Yeasts. *Journal of Basic Microbiology* **1988,** *28* (5), 293-319.

124. Korpan, Y. I.; Gonchar, M. V.; Sibirny, A. A.; Martelet, C.; El'skaya, A. V.; Gibson, T. D.; Soldatkin, A. P. Development of highly selective and stable potentiometric sensors for formaldehyde determination. *Biosensors & Bioelectronics* **2000,** *15* (1-2), 77-83.

125. ten Kortenaar, M. V.; Kolar, Z. I.; de Gopeij, J. J. M.; Frens, G. Electrocatalytic oxidation of formaldehyde on gold studied by differential electrochemical mass spectrometry and voltammetry. *Journal of the Electrochemical Society* **2001,** *148* (8), E327-E335.

126. Bard, A. J.; Faulkner, L. R. Electrochemical Methods: Fundamentals and Applications. 2001. New York, J. Wiley & Sons.
Ref Type: Generic

127. Montenegro, M. I.; Pletcher, D.; Liolios, E. A.; Mazur, D. J.; Zawodzinski, C. A Microelectrode Study of the Reduction of Formaldehyde in Neutral Concentrated Aqueous-Solutions. *Journal of Applied Electrochemistry* **1990,** *20* (1), 54-59.

128. Schedin, F.; Geim, A. K.; Morozov, S. V.; Hill, E. W.; Blake, P.; Katsnelson, M. I.; Novoselov, K. S. Detection of individual gas molecules adsorbed on graphene. *Nature Materials* **2007,** *6* (9), 652-655.

129. Gunawidjaja, R.; Kharlampieva, E.; Choi, I.; Tsukruk, V. V. Bimetallic Nanostructures as Active Raman Markers: Gold-Nanoparticle Assembly on 1D and 2D Silver Nanostructure Surfaces. *Small* **2009,** *5* (21), 2460-2466.

130. Berry, V.; Saraf, R. F. Modulation of Electron-Tunneling in Nanoparticle Array by Sound Wave: An Avenue to High Speed, High Sensitivity Sensors. *Small* **2011**.

131. Zhou, Y. X.; Johnson, A. T. Simple fabrication of molecular circuits by shadow mask evaporation. *Nano Letters* **2003,** *3* (10), 1371-1374.

132. Wang, D. S.; Chao, J. J.; Hung, S. C.; Lin, C. F. Fabrication of large-area gallium arsenide nanowires using silicon dioxide nanoparticle mask. *Journal of Vacuum Science & Technology B* **2009,** *27* (6), 2449-2452.

133. Ishii, Y.; Sakai, H.; Murata, H. Fabrication of a submicron-channel organic field-effect transistor using a controllable electrospun single fibre as a shadow mask. *Nanotechnology* **2011,** *22* (20).

134. Kumar, A.; Whitesides, G. M. Features of Gold Having Micrometer to Centimeter Dimensions Can be Formed Through A Combination of Stamping with An Elastomeric Stamp and An Alkanethiol Ink Followed by Chemical Etching. *Applied Physics Letters* **1993,** *63* (14), 2002-2004.

135. Kumar, A.; Biebuyck, H. A.; Whitesides, G. M. Patterning Self-Assembled Monolayers - Applications in Materials Science. *Langmuir* **1994,** *10* (5), 1498-1511.

136. Tan, J. L.; Tien, J.; Chen, C. S. Microcontact printing of proteins on mixed self-assembled monolayers. *Langmuir* **2002,** *18* (2), 519-523.

137. Kane, R. S.; Takayama, S.; Ostuni, E.; Ingber, D. E.; Whitesides, G. M. Patterning proteins and cells using soft lithography. *Biomaterials* **1999,** *20* (23-24), 2363-2376.

138. Rogers, J. A.; Bao, Z.; Baldwin, K.; Dodabalapur, A.; Crone, B.; Raju, V. R.; Kuck, V.; Katz, H.; Amundson, K.; Ewing, J.; Drzaic, P. Paper-like electronic displays: Large-area rubber-stamped plastic sheets of electronics and microencapsulated electrophoretic inks. *Proceedings of the National Academy of Sciences of the United States of America* **2001,** *98* (9), 4835-4840.

139. Roman, L. S.; Inganas, O.; Granlund, T.; Nyberg, T.; Svensson, M.; Andersson, M. R.; Hummelen, J. C. Trapping light in polymer photodiodes with soft embossed gratings. *Advanced Materials* **2000,** *12* (3), 189-+.

140. Graham, D. J.; Price, D. D.; Ratner, B. D. Solution assembled and microcontact printed monolayers of dodecanethiol on gold: A multivariate exploration of chemistry and contamination. *Langmuir* **2002,** *18* (5), 1518-1527.

141. Glasmastar, K.; Gold, J.; Andersson, A. S.; Sutherland, D. S.; Kasemo, B. Silicone transfer during microcontact printing. *Langmuir* **2003,** *19* (13), 5475-5483.

142. Wang, X. J.; Ostblom, M.; Johansson, T.; Inganas, O. PEDOT surface energy pattern controls fluorescent polymer deposition by dewetting. *Thin Solid Films* **2004,** *449* (1-2), 125-132.

143. Asberg, P.; Nilsson, K. P. R.; Inganas, O. Surface energy modified chips for detection of conformational states and enzymatic activity in biomolecules. *Langmuir* **2006,** *22* (5), 2205-2211.

144. Cortese, B.; Piliego, C.; Viola, I.; D'Amone, S.; Cingolani, R.; Gigli, G. Engineering Transfer of Micro- and Nanometer-Scale Features by Surface Energy Modification. *Langmuir* **2009,** *25* (12), 7025-7031.

145. Kim, J. H.; Hwang, H. S.; Hahm, S. W.; Khang, D. Y. Hydrophobically Recovered and Contact Printed Siloxane Oligomers for General-Purpose Surface Patterning. *Langmuir* **2010,** *26* (15), 13015-13019.

146. Briseno, A. L.; Roberts, M.; Ling, M. M.; Moon, H.; Nemanick, E. J.; Bao, Z. N. Patterning organic semiconductors using "dry" poly(dimethylsiloxane) elastomeric stamps for thin film transistors. *Journal of the American Chemical Society* **2006,** *128* (12), 3880-3881.

147. McDonald, J. C.; Duffy, D. C.; Anderson, J. R.; Chiu, D. T.; Wu, H. K.; Schueller, O. J. A.; Whitesides, G. M. Fabrication of microfluidic systems in poly(dimethylsiloxane). *Electrophoresis* **2000,** *21* (1), 27-40.

148. Pickering, J. P.; van der Meer, D. W.; Vancso, G. J. Effects of contact time, humidity, and surface roughness on the adhesion hysteresis of polydimethylsiloxane. *Journal of Adhesion Science and Technology* **2001,** *15* (12), 1429-1441.

149. Evans, D. F.; Wennerstrom, H. *The Colloidal Domain Where Physics, Chemistry, Biology, and Technology Meet;* 2nd ed ed.; Wiley VCH: New York, 1999.

150. Singh, G.; Saraf, R. F. Direct measurement of ion accumulation at the electrode electrolyte interface under an oscillatory electric field. *Journal of Physical Chemistry B* **2006,** *110* (25), 12581-12587.

151. Luna, M.; Colchero, J.; Gil, A.; Gomez-Herrero, J.; Baro, A. M. Application of non-contact scanning force microscopy to the study of water adsorption on graphite, gold and mica. *Applied Surface Science* **2000,** *157* (4), 393-397.

152. Bassindale, A.; Taylor, P. In *The Chemistry of Organic Silicon Compounds*, Patai, S., Rappoport, Z., Eds.; John Wiley: Chichester, 1989; pp 810-839.

153. Kendrick, T.; Parbhoo, B.; White, J. In *The Chemistry of Organic Silicon Compounds: Part 2*, Patai, S., Rappoport, Z., Eds.; John Wiley: Chichester, 1989; pp 1290-1361.

154. Fowkes, F. M. In *Treatise on Adhesion and Adhesives*, Patrick, R. L., Ed.; Marcel Dekker: New York, 1967; pp 325-447.

155. Cohen-Karni, T.; Timko, B. P.; Weiss, L. E.; Lieber, C. M. Flexible electrical recording from cells using nanowire transistor arrays. *Proceedings of the National Academy of Sciences of the United States of America* **2009,** *106* (18), 7309-7313.

156. Katta, P.; Alessandro, M.; Ramsier, R. D.; Chase, G. G. Continuous electrospinning of aligned polymer nanofibers onto a wire drum collector. *Nano Letters* **2004,** *4* (11), 2215-2218.

157. Li, D.; Wang, Y. L.; Xia, Y. N. Electrospinning of polymeric and ceramic nanofibers as uniaxially aligned arrays. *Nano Letters* **2003,** *3* (8), 1167-1171.

158. Tseng, R. J.; Huang, J. X.; Ouyang, J.; Kaner, R. B.; Yang, Y. Polyaniline nanofiber/gold nanoparticle nonvolatile memory. *Nano Letters* **2005,** *5* (6), 1077-1080.

159. Wang, Y. Z.; Yang, Q. B.; Shan, G. Y.; Wang, C.; Du, J. S.; Wang, S. G.; Li, Y. X.; Chen, X. S.; Jing, X. B.; Wei, Y. Preparation of silver nanoparticles dispersed in polyacrylonitrile nanofiber film spun by electrospinning. *Materials Letters* **2005,** *59* (24-25), 3046-3049.

160. Han, G. Y.; Guo, B.; Zhang, L. W.; Yang, B. S. Conductive gold films assembled on electrospun poly(methyl methacrylate) fibrous mats. *Advanced Materials* **2006,** *18* (13), 1709-+.

161. Li, D.; Mccann, J. T.; Gratt, M.; Xia, Y. N. Photocatalytic deposition of gold nanoparticles on electrospun nanofibers of titania. *Chemical Physics Letters* **2004,** *394* (4-6), 387-391.

162. Son, W. K.; Youk, J. H.; Lee, T. S.; Park, W. H. Preparation of antimicrobial ultrafine cellulose acetate fibers with silver nanoparticles. *Macromolecular Rapid Communications* **2004,** *25* (18), 1632-1637.

163. Dong, F. X.; Li, Z. Y.; Huang, H. M.; Yang, F.; Zheng, W.; Wang, C. Fabrication of semiconductor nanostructures on the outer surfaces of polyacrylonitrile nanofibers by in-situ electrospinning. *Materials Letters* **2007,** *61* (11-12), 2556-2559.

164. Wang, Y. Z.; Li, Y. X.; Sun, G.; Zhang, G. L.; Liu, H.; Du, J. S.; Yang, S. A.; Bai, J.; Yang, Q. B. Fabrication of Au/PVP by electrospinning nanofiber composites by electrospinning. *Journal of Applied Polymer Science* **2007,** *105* (6), 3618-3622.

165. Kim, G. M.; Wutzler, A.; Radusch, H. J.; Michler, G. H.; Simon, P.; Sperling, R. A.; Parak, W. J. One-dimensional arrangement of gold nanoparticles by electrospinning. *Chemistry of Materials* **2005,** *17* (20), 4949-4957.

166. Dong, H.; Fey, E.; Gandelman, A.; Jones, W. E. Synthesis and assembly of metal nanoparticles on electrospun poly(4-vinylpyridine) fibers and poly(4-vinylpyridine) composite fibers. *Chemistry of Materials* **2006,** *18* (8), 2008-2011.

167. Kundu, S.; Gill, R.; Saraf, R. F. Electrospinning of PAH Nanofiber and Deposition of Au NPs for Nanodevice Fabrication. *The Journal of Physical Chemistry C* **2011**.

168. Reneker, D. H.; Chun, I. Nanometre diameter fibres of polymer, produced by electrospinning. *Nanotechnology* **1996,** *7* (3), 216-223.

APPENDIX A

DETERMINATION OF V_T AND ζ FROM I-V DATA

The method to determine V_T and ζ is demonstrated on the 10 μm device from Chapter 3 at room temperature. Raw I-V data is plotted in Origin on a log-log scale (Fig. A1.1). Data is fit according to a non-linear curve fitting function using the built-in power law function: $y = A|x - x_c|^P$. The fitting function corresponds to the second order phase transition for the current in an array, $I = A(V - V_T/V_T)^{\zeta}$. There is a large deviation close to V_T due to the discontinuity in the non-linear regression curve at the critical point. However, far from V_T, the curve fit is excellent, where at large bias the slope of the fit corresponds to the critical exponent, ζ. The minimum in the curve fit aligns well with the

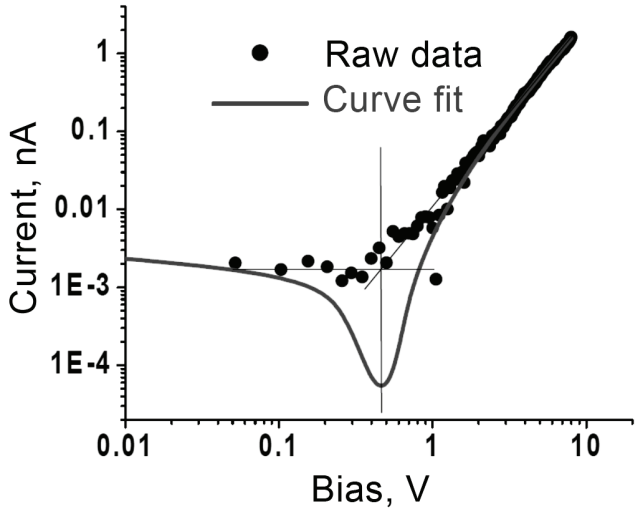

Figure A1.1 Determination of V_T and ζ from raw I-V data. The I-V data for the 10 μm device at 295 K is plotted on a log-log scale. A sharp change in the slope of the non-linear curve fit indicates that $V_T = 0.45$ V.

apparent V_T of the raw data, indicating the consistency of the evaluated V_T to the raw data. For the 10 μm device, a $V_T \sim 0.45$ V is determined, explicitly illustrating the Coulomb blockade effect at room temperature.

APPENDIX B

Cell Culturing *Pichia pastoris*

The wildtype X-33 strain of *Pichia pastoris* used in this study is fermented in a batch reactor according to the following procedure:

1. Using a sterile loop, place one colony into a flask containing 5 mL of YPD media.
2. Place the flask into a water bath shaker at 28 – 30°C at an rpm of 200 for 18 hours.
3. Pipette 100 μL of the yeast solution from the flask into a test tube containing 5 mL of BMGY media.
4. Place the test tube into a water bath shaker at 28 – 30°C at an rpm of 200 for 18 hours.
5. Fill 5 microcentrifuge tubes with 1 mL of BMGY-yeast solution, respectively.
6. Centrifuge the test tubes at 7,000 rpm for 10 minutes.
7. Discard the supernatant and add 1 mL of BMMY media to each of the 5 microcentrifuge tubes.
8. Vortex the tubes.
9. Transfer the contents of the 5 microcentrifuge tubes of BMMY-yeast solution into a flask.
10. Place the flask into a water bath shaker at 28 – 30°C at an rpm of 200 for 12 hours.
11. Fill 5 microcentrifuge tubes with 1 mL of the BMMY-yeast solution.
12. Centrifuge the tubes at 10,000 rpm for 2 minutes.
13. Discard the supernatant and add 1 mL of sterile deionized water to each microcentrifuge tube.
14. Repeat water washing two times.

The yeast should be deposited as soon as possible onto a device and kept at a humidity of ~70% and temperature of 26°C.

MEDIA RECIPES:

BMGY with Soytone

Yeast extract (Difco)	20 g
Soytone (Difco)	40 g
1M Potassium phosphate buffer	200 mL
13.4% YNB (yeast nitrogen base without amino acids, Difco)	200 mL
Glycerol (Sigma-Aldrich)	25.22 g
0.02% Biotin (Fisher BioReagents)	4 mL

In MilliQ water, at a total volume of 2.0 L and pH 6. Autoclave for 20 minutes on liquid cycle.

BMMY with Soytone

Yeast extract (Difco)	20 g
Soytone (Difco)	40 g
1M Potassium phosphate buffer	200 mL
13.4% YNB (yeast nitrogen base without amino acids, Difco)	200 mL
Methanol (Sigma-Aldrich)	10 mL
0.02% Biotin (Fisher BioReagents)	4 mL

In MilliQ water, at a total volume of 2.0 L and pH 6. Autoclave for 20 minutes on liquid cycle. Cool to room temperature before adding methanol.